Formulation Design of Spray-Dried Microparticles for Respiratory Drug Delivery

by

Mani Ordoubadi

A thesis submitted in partial fulfillment of the requirements for the degree of

Doctor of Philosophy

Department of Mechanical Engineering

University of Alberta

Abstract

In this thesis, several fundamental studies were conducted to tackle some of the unanswered questions in the design and engineering of inhalable microparticles produced via spray drying. Different experimental and theoretical methods were applied to understand the mechanisms that control particle formation of formulations containing solvents and excipients of the most interest.

Chapter 1 contains a brief introduction to drug delivery to the lungs in general and the appropriate tools and devices used. Next, the spray drying process is introduced and explained as one of the industrial processes employed in the production of pulmonary microparticles. The most pressing problems and questions faced by a formulator are discussed next, both with respect to overcoming the issue of emerging low-water-soluble drugs and with respect to choosing the necessary excipients to meet the physicochemical targets in the final product.

Chapter 2 focuses on the evaporation of multi-solvent microdroplets and the ensuing particle formation pertaining to the spray drying of inhalable powders containing hydrophobic active ingredients. The evaporation of such multi-solvent droplets and their internal solute transfers are theoretically modeled and compared to the measurements performed using a single-particle electrodynamic balance and a droplet chain instrument. The results show that the two parameters controlling the general morphology of the dried particles the most - namely the level of saturation and the Péclet number - change with time in a multi-solvent droplet during evaporation. This temporal variation

of the parameters introduces complexities during the formulation design but vanishes at an iso-compositional state similar to the azeotrope of non-ideal mixtures.

In Chapter 3, the particle formation of L-leucine, a dispersibility-enhancing amino acid is studied extensively. Three complementary experimental methods are used: an electrodynamic balance, a monodisperse droplet chain, and a conventional lab-scale spray dryer. The shell formation kinetics of leucine in the presence of trehalose is measured using the electrodynamic balance, the particle morphologies and densities are studied using the droplet chain instrument, and spray drying is used to produce powders representative of actual industrial applications and to allow for further characterization and analytical measurements. A modified particle formation method appropriate for crystallizing components is developed to interpret the experimental measurements and observations. It is confirmed that other components can interfere with the free crystallization of the shell former. Moreover, it is observed that the surface coverage of a crystallizing shell former such as leucine shows a rather large variation for different particle sizes in the same batch of powder, which points to the mechanisms of nucleation and crystal growth in such systems. The modified particle formation theory is hence shown to be a valuable tool in the formulation design of systems containing a number of excipients and active ingredients.

In Chapter 4, the formation of trileucine-containing microdroplets is studied experimentally, and the results are explained theoretically. The kinetics of shell formation is measured using an electrodynamic balance and a droplet chain is used to measure the particle densities and examine the morphologies. Spray drying is used to produce enough powder for spectroscopy analysis. A comparison of the results to theoretical models reveals that the dispersibility enhancement of trileucine is due to two consecutive stages: the adsorption of a

mono-molecular layer on the droplet surface owing to its surface activity and the early amorphous phase separation as a result of its low aqueous solubility. Based on this information, a process is proposed so that a formulator can design an excipient system to make low- or high-density particles to meet the design targets while maintaining good aerosol performance.

Chapter 5 summarizes the main conclusions of the thesis and presents some suggestions for future work.

Preface

Some of the research conducted for this work are parts of an international scientific and industrial collaboration between the Particle Engineering group at the University of Alberta, the Bristol Aerosol Research Centre at the University of Bristol, and the Pharmaceutical Technology & Development at AstraZeneca.

Chapter 2 of this thesis has been published as

> M. Ordoubadi, F.K.A. Gregson, O. Melhem, D. Barona, R.E.H. Miles, D. D'Sa, S. Gracin, D. Lechuga-Ballesteros, J.P. Reid, W.H. Finlay, R. Vehring, Multi-Solvent Microdroplet Evaporation: Modeling and Measurement of Spray-Drying Kinetics with Inhalable Pharmaceutics, Pharm. Res. 36 (2019) 100.

I developed the multi-solvent model and wrote its computer source code in the C++ language. I wrote the majority of the manuscript with the help of Florence Gregson on Section 2.2.2 and Omar Melhem on Section 2.2.3. I was responsible for the experiment design and conceptualization, while the EDB measurements were conducted by Florence Gregson at the University of Bristol, and the droplet chain experiments, training and SEM were conducted by Omar Melhem. The FIB/HIM was conducted by David Barona. Reinhard Vehring supervised the work and Warren Finlay provided insights on the multi-solvent model. All coauthors gave feedback on the manuscript.

Chapter 3 of this thesis has been published as

> M. Ordoubadi, F.K.A. Gregson, H. Wang, M. Nicholas, S. Gracin, D. Lechuga-Ballesteros, J.P. Reid, W.H. Finlay, R. Vehring, On

the particle formation of leucine in spray drying of inhalable microparticles, Int. J. Pharm. 592 (2021) 120102.

I wrote the majority of the manuscript and all coauthors gave feedback. I did the experimental design and conceptualization. Hui Wang trained me in the use of the B-191 spray dryer and helped me with some of the spray drying runs. He also conducted the Raman spectroscopy measurements and wrote the respective subsection of the manuscript. I performed the droplet chain experiments, the remainder of the spray drying runs, and the SEMs. Florence Gregson conducted the EDB measurements at the University of Bristol. The TOF-SIMS was performed by Mark Nicholas at AstraZeneca Sweden. I did the size-binning and quantification of TOF-SIMS data myself.

Chapter 4 of this thesis has been submitted as

M. Ordoubadi, F.K.A. Gregson, H. Wang, N.B. Carrigy, M. Nicholas, S. Gracin, D. Lechuga-Ballesteros, J.P. Reid, W.H. Finlay, R. Vehring, Trileucine as a Dispersibility Enhancer of Spray-Dried Inhalable Microparticles, J Control Release. submitted Jan 25, 2021.

I wrote the majority of the manuscript and all coauthors gave feedback. I did the experimental design and conceptualization. Hui Wang conducted the Raman spectroscopy measurements. I performed the droplet chain experiments, the spray drying runs, and the SEMs. Florence Gregson conducted the EDB measurements at the University of Bristol. The TOF-SIMS was perfromed by Mark Nicholas at AstraZeneca Sweden. I did the size-binning and quantification of TOF-SIMS data myself.

The studies conducted in this thesis contributed to the following conference publications:

M. Ordoubadi, F. Gregson, W.H. Finlay, R. Vehring, J.P. Reid, Interaction of Evaporating Multicomponent Microdroplets with Humid Environments, in: Respir. Drug Deliv., 2018.

M. Ordoubadi, H. Wang, M. Nicholas, S. Gracin, D. Lechuga-Ballesteros, W.H. Finlay, R. Vehring, Understanding the Dispersibility Enhancement of L-Leucine in the Spray Drying of Inhalable Microparticles, in: Respir. Drug Deliv., 2021.

M. Ordoubadi, H. Wang, N.B. Carrigy, M. Nicholas, S. Gracin, D. Lechuga-Ballesteros, W.H. Finlay, R. Vehring, How Does Trileucine Act as a Dispersibility Enhancer in the Spray Drying of Microparticles?, in: Respir. Drug Deliv., 2021.

To my parents, Firooz and Vida;
to the loving memory of my brother, Maziar;
to my wife, Firoozeh.

Acknowledgements

My deepest gratitude goes to Prof. Reinhard Vehring for his patient guidance, support, and kindness over the past 4 years. I wish to pay my special regards to Prof. Warren Finlay for his invaluable guidance and suggestions on different parts of this thesis. I wish to thank Luba Slabyj for her meticulous help and assistance in reviewing the manuscripts and the thesis. I am also extremely grateful to Florence Gregson and Prof. Jonathan Reid at the University of Bristol, and Sandra Gracin, David Lechuga-Ballesteros, and Mark Nicholas at AstraZeneca plc for their support, suggestions, and scientific collaborations. I am indebted to my friends and colleagues at the Particle Engineering group for their friendship, assistance, and scientific suggestions throughout the course of this work. Last but not least, I would like to express my wholehearted appreciation for the loving care and support of my family and friends, without whom this work would not be possible.

Contents

List of Tables

List of Figures

Chapter 1

Introduction

1.1 Pulmonary Drug Delivery

Among the different drug administration paths, the inhalation route is interesting because of its non-invasive nature, convenience, and fast onset of action. This route is especially advantageous for local treatment of lung diseases with minimal side effects and required doses [1]. The main applications of inhaled aerosols are the treatment and maintenance therapy of asthma, chronic obstructive pulmonary disease (COPD), cystic fibrosis, and pulmonary arterial hypertension through the use of bronchodilators, corticosteroids, antibiotics, and vasodilators [2, 3]. The pulmonary route also holds some potential for systemic delivery due to the significantly large surface area available in the alveolar regions of the lung and is employed in some commercial products for pain relief and diabetes treatment [2, 4].

While pulmonary drug delivery carries many advantages, there are some inherent complexities to this practice mostly due to the physiological function and defense mechanisms of the respiratory tract. These defense mechanisms include mechanical, chemical, and immunological barriers [2]. Mechanical barriers include the filtration of large particles due to inertial impaction in the upper airways [1, 5], and mucociliary clearance, caused by the constant beating of hair-like extrusions called cilia, which move the material deposited on the mucus layer surrounding the conducting airways up the trachea to the oropharynx [6]. Based on the solubility of their components, deposited particles that are not cleared by the mucociliary mechanism can dissolve in the

lung fluid and either be adsorbed or go through enzymatic degradation [7]. Ultimately, phagocytosis by alveolar macrophages is the last line of defense against inhaled material [8]. These natural defense mechanisms of the respiratory system complicate the whole process of pulmonary drug delivery.

Drugs are delivered to the lungs through the inhalation of aerosols. The inhaled particles need to have specific aerodynamic properties for efficient delivery to the targeted sites [1]. If not designed properly, drug-containing aerosols will settle and deposit in unintended areas of the respiratory tract, such as the mouth and throat, decreasing the lung dose and potentially causing adverse reactions in these locations [9]. Particles need to have aerodynamic diameters between 1-5 µm to maximize delivery to the lungs [1, 10]. The aerodynamic diameter of a particle is defined as the diameter of a sphere having a density of 1 g/cm^3 (that of water) and the same settling velocity as the initial particle [11]. The aerodynamic diameter, d_a, of a nearly spherical particle with a geometric diameter of d_p can be calculated from [11]

$$d_\mathrm{a} = d_\mathrm{p} \left(\frac{C_\mathrm{c}\left(d_\mathrm{p}\right) \rho_\mathrm{p}}{C_\mathrm{c}\left(d_\mathrm{a}\right) \rho_0} \right)^{1/2}, \tag{1.1}$$

where $C_\mathrm{c}\left(d\right)$ is the slip correction factor, which corrects the settling velocity for the partial slip boundary condition in the Stokes' law, and ρ_p and ρ_0 are the densities of the particle and water, respectively.

Consequently, the physical dimension of the particles is one of the most important factors in the design and production of powders intended for lung delivery. The large-scale production of small solid particles with a narrow enough polydispersity to place them in the respirable range is one of the challenges facing the pharmaceutical industry. If the drug is to be delivered as a dry powder, different particle manufacturing and processing techniques are used commercially for the production of micron-sized particles, namely, milling [12, 13], spray drying [14–16], and supercritical solvent manufacturing [17, 18]. Among these methods, spray drying, which is the main focus of this work, is of interest in the large-scale production of microparticles because it is a fast continuous process by nature and can be easily scaled up [15]. Moreover, a formulator can control with ease some of the physical properties of the spray-

dried powders, such as the size distribution, density, and radial distribution of different components of the dried particles [14].

1.1.1 Devices

There are several devices and methods commercially used for pulmonary drug delivery, including pressurized metered-dose inhalers (pMDIs), dry powder inhalers (DPIs), Nebulizers, and soft mist inhalers.

pMDIs, which hold about 70% of the inhalation devices market share [19], deliver accurate doses of a drug via the release of a superheated liquid (the propellant) from a canister [1]. The drug, usually less than 10 mg/mL in concentration, is dissolved (solution MDIs) or suspended as microparticles (suspension MDIs) in the propellant liquid. Besides the drug, certain excipients, surfactants, or co-solvents might be added to the formulation to enhance the aerosol properties, suspension stability, or solution solubility [1, 19, 20]. Upon actuation, the superheated solution or suspension undergoes flash evaporation and atomization into microdroplets that are delivered to the patient at high speeds through the mouthpiece [1, 21]. Due to the high vapor pressures of the propellants, the atomized droplets are then evaporated rapidly, leaving behind aerosolized drug-containing microparticles ready for inhalation.

DPIs are devices through which a specific quantity of solid powder composed of the drug and typically some excipients are fluidized through a high-velocity air flow. This air flow is provided by a sharp breath administered by the patient (passive DPIs), or via the help of an external source of energy (active DPIs) [1]. The flow should induce enough force on the powders to entrain the particles and break any agglomerates into their primary particles; otherwise, the majority of the powder will not leave the device or will deposit in the upper airways, which can reduce the delivered dose to the lungs significantly [22].

Nebulizers aerosolize a solution or suspension (usually aqueous) into a gas for inhalation through a mouthpiece or mask [1]. The main advantage over pocket-sized devices such as pMDIs and DPIs is that nebulizers can be used with ordinary tidal breathing in patients who cannot perform arduous inhala-

tion efforts because they are very young, very old, or otherwise incapacitated [23].

Soft mist inhalers, the newest kind of portable devices, produce a cloud of droplets containing the drug [24]. The energy required for aerosolization is usually provided from a battery or a spring, and the produced mist exits the mouthpiece at much slower velocities than in pMDIs and DPIs, resulting in more efficient lung delivery [24].

It can be seen that solid particles are present in a majority of the dosage forms used in all devices, such as DPIs and suspensions in pMDIs, nebulizers, and soft mist inhalers. Consequently, the production of solid microparticles comprises a significant part of the pharmaceutical industry related to pulmonary drug delivery.

1.2 Spray Drying

As shown in Figure 1.1, the spray drying process is composed of three main stages: 1) atomization of the liquid feed into microdroplets, 2) rapid evaporation of these droplets by the passage of a high-temperature drying gas over them, and 3) collection of the residual microparticles through different mechanisms such as cyclone separation and electrostatic precipitation [15]. The spray drying cycle can be open, for aqueous solvents, or closed, with solvent capture for organic solvents or hazardous components [25]. The production of pharmaceutical aerosols via spray drying has been well-understood and documented in recent years, as seen in some of the published review articles [14, 16, 26]. What warrants further study is the mechanistic understanding of the underlying phenomena that control droplet evaporation and particle formation.

Besides having a specific size, spray-dried particles intended for pulmonary drug delivery need to meet other physical, chemical, and solid-state specifications [10]. These properties affect conditions such as long-term physicochemical stability, compressed bulk density, dispersibility, and dissolution rate [10, 14], all of which determine the efficacy of the pharmaceutical actives. These facts emphasize the need for a fundamental understanding of the processes

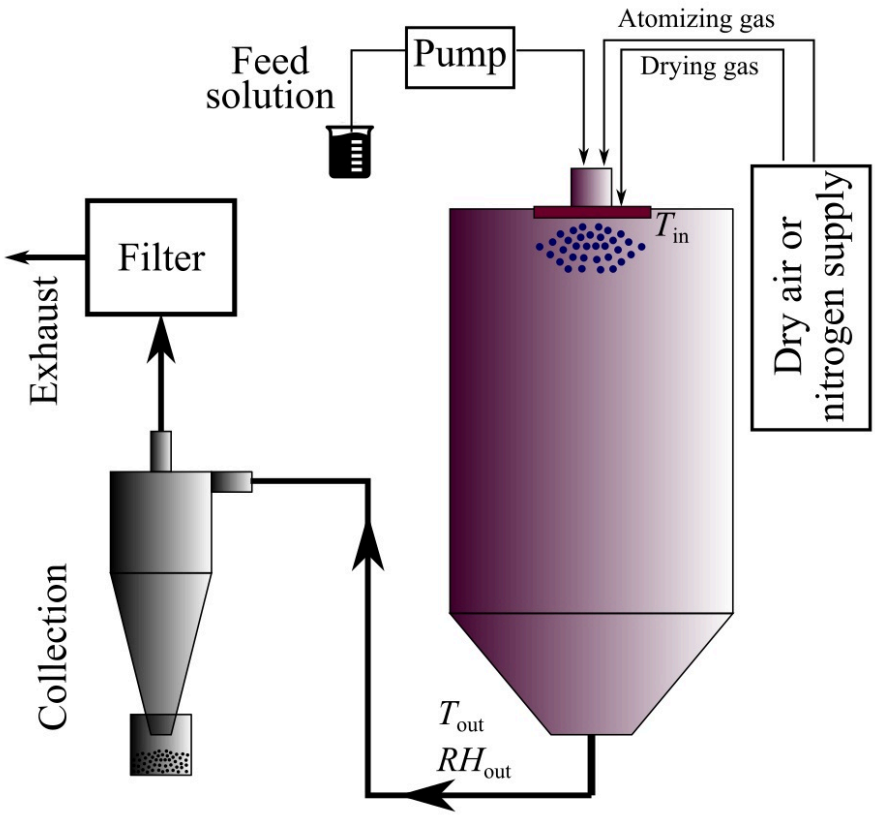

Figure 1.1: Schematic of a typical open loop spray dryer.

that occur during spray drying, from the atomization of the feed solution, to the water uptake of the resulting powder during handling and storage. The most significant part is the drying of these microdroplets into smaller solid particles. The important characteristics of the resulting powder are direct consequences of the different phenomena of heat and mass transfer that occur during this drying stage [14]. By understanding these phenomena, a particle engineer will be able to answer such questions as the following:

- Will the final particle have a smooth or rugose surface (affects dispersibility, water uptake, and bulk density)?
- Will the final particle exhibit a shell with a hollow void inside or will it be solid throughout (affects bulk density and aerodynamic size)?
- Which component will dominate the surface composition (affects dissolution rate, dispersibility, water uptake, and physicochemical stability)?

- What solid phase will the particle have (affects physical stability, dissolution rate, and water uptake)?

Particle formation models are used to tackle such questions in a predictive manner and limit the number of experimental iterations in order to significantly reduce costs and risks at the early stages of the formulation design process [27].

The theoretical models have better predictive capabilities for components that do not crystallize, have high solubility, and are not surface active [14]. Incidentally, two of the most effective dispersibility enhancers, namely leucine and trileucine, which are currently in clinical development [28], are both surface-active [29] with relatively low aqueous solubility [29, 30], and the former can crystallize during spray drying [31].

Moreover, the developed models work best for single-solvent systems with constant evaporation rates [32, 33]. This is while, low water solubility is a growing concern in the pharmaceutical industry, as about 70% of the newly investigated chemical ingredients are hydrophobic [34]. This fact explains the interest in spray drying out of co-solvent systems, both in the production of amorphous solid dispersions to improve the dissolution rates [35, 36], and in solubilizing the hydrophobic actives in the presence of hydrophilic excipients [37, 38].

The main objectives of this thesis are to address the shortcomings in the available particle formation models for co-solvent systems and for the materials that act best as dispersibility enhancers due to their surface activity and low solubilities, such as leucine and trileucine.

Chapter 2

Multi-Solvent Microdroplet Evaporation: Modeling and Measurement of Spray Drying Kinetics with Inhalable Pharmaceuticals

Evaporation and particle formation from multi-solvent microdroplets containing solid excipients pertaining to spray drying of therapeutic agents intended for lung delivery were studied. Various water and ethanol co-solvent systems containing a variety of actives and excipients (beclomethasone, budesonide, leucine, and trehalose) were considered.

Numerical methods were used to predict the droplet evaporation rates and internal solute transfers, and their results verified and compared with results from two separate experimental setups. In particular, an electrodynamic balance was used to measure the evaporation rates of multicomponent droplets and a monodisperse droplet chain setup collected dried microparticles for further analytical investigations and ultramicroscopy.

The numerical results are used to explain the different particle morphologies dried from solutions at different co-solvent compositions. The obtained numerical data clearly show that the two parameters controlling the general morphology of a dried particle, namely the Péclet number and the degree of saturation, can change with time in a multi-solvent droplet. This fact

complicates product development for such systems. However, this additional complexity vanishes at what we define as the iso-compositional point, which occurs when the solvent ratios and other composition-dependent properties of the droplet remain constant during evaporation, similar to the azeotrope of such systems during distillation.

Numerical and experimental analysis of multi-solvent systems indicate that spray drying near the iso-compositional ratio simplifies the design and process development of such systems.

2.1 Introduction

The study of evaporation and condensation of volatile components from micro-droplets is important in many areas of engineering, pharmaceutics, medicine and environmental sciences [39–43]. The studies pertaining specifically to inhalable therapeutics are of great significance, as these hygroscopic aerosols can undergo severe morphological transformations due to mass and heat transfer in different environmental conditions ranging from the hot and relatively dry settings in spray dryers [26] to the highly humid passages of the respiratory tract [44]. In many of these circumstances, such as spray drying from a co-solvent system [37, 45] or the condensation of water on a propellant droplet [46], there is more than one volatile component inside the droplet. Models and analytical techniques can reduce the time, cost and risks associated with experimentation during the design and study of spray-dried particles [33, 47]. In spray drying from single volatile components, the initial solute saturation and a dimensionless number called the Péclet number, which typically has a constant value for a single solvent droplet, determine the general morphology of the dried particles at different drying conditions [33]. In an evaporating multi-solvent droplet, complications arise in the prediction and design stage as the composition of the droplet, its temperature, evaporation rate and the solubilities of the excipients change over the drying time, further highlighting the need for a numerical model in order to understand the underlying physics.

The study of evaporation of multicomponent droplets is specifically preva-

lent in fuel spray and combustion applications [43, 48–51] and environmental aerosol and cloud formation [52]. Assuming one-dimensional heat and mass transfers around and inside the droplet, the two models that have been used most frequently to model evaporation or condensation of a single aerosol droplet are the Maxwell model, which neglects the radial convective fluxes around the droplet, and the Stefan-Fuchs model, which accounts for these radial mass fluxes commonly known as Stefan flow [43, 53]. In this study, modified versions of these models appropriate for multi-solvent microdroplets are compared to assess their applicability in microparticle formation studies based on accuracy and levels of complexity.

There is a growing interest in using multi-solvent formulations in spray drying hydrophobic active pharmaceutical ingredients such as budesonide [37], beclometasone dipropionate [54], triamcinolone acetonide [55] and fluticasone propionate [56] in order to achieve reasonable feed solute concentrations, production yield, dispersibility, and particle aerodynamic properties. Therefore, predictions of the evaporation and solvent compositions of co-solvent droplets containing such actives are useful during their design and development stages. However, the different mechanisms of particle formation in such systems have yet to be studied comprehensively.

The evaporation rates and drying kinetics of microdroplets are usually studied experimentally via the use of single particle methods such as optical traps [57], electrodynamic balances (EDBs) [40, 58] and droplet chain instruments [32, 59, 60].

In this study, validation of a numerical model is provided from measurements made with a Comparative-Kinetics Electrodynamic Balance (CK-EDB), which can levitate a single micron-sized aerosol droplet indefinitely. Light scattering can be used to infer the time-dependence of the droplet size with high accuracy in a controlled environment. Dry particle collection for comparison with the model predictions is performed using an in-house monodisperse droplet chain setup, which generates monodisperse particles. Even though imaging of the droplet chain facilitates the determination of droplet evaporation rates, this instrument is used here for the sole purpose of particle

collection, as the CK-EDB outperforms it in sizing accuracy.

To assess the applicability of the numerical model in predicting the drying behavior and morphology of spray-dried microdroplets, the evaporation dynamics of various microdroplets containing different mixtures of water and ethanol are compared to our experimental data.

2.2 Materials and Methods

2.2.1 Materials

Trehalose dihydrate and L-leucine were purchased from Fisher Scientific (Ottawa, ON, Canada). The solvents used were absolute grade ethanol with purity of greater than 99.8% purchased from Sigma Aldrich (Oakville, ON, Canada) and HPLC grade water from Fisher Scientific (Ottawa, ON, Canada).

2.2.2 Comparative-Kinetics Electrodynamic Balance (CK-EDB)

The evaporation rates of multicomponent droplets were measured over a range of environmental conditions using a Comparative-Kinetics Electrodynamic Balance (CK-EDB) in which single aerosol droplets consisting of a mixture of water and ethanol were levitated. This technique has been described in detail in a previous publication [58] and is only briefly outlined here: A charged droplet with an initial diameter of approximately 44 µm of known composition was generated by a droplet-on-demand dispenser (MJ-ABP-01, MicroFab Technologies, Plano, Texas, USA) and injected into the center of the chamber of the instrument. The droplet was trapped within an electric field produced by two sets of concentric cylindrical electrodes, mounted vertically above one another. An AC voltage was applied to the electrodes, with an additional DC voltage superimposed across the bottom set of electrodes to counteract the gravitational force of the droplet. This technique allowed for stable trapping of charged droplets throughout the evaporation process. A gas flow formed from mixing wet and dry nitrogen gas streams passed over the droplet, permitting accurate control of relative humidity (RH) in the chamber ranging from

0 to about 95%. This stream flowed with a velocity of about 3 cm/s inside the drying chamber during the measurements. Based on the available corrections [43], this flow with a Reynolds number of about 0.1 around a droplet with a diameter of 50 µm increases the Nusselt and Sherwood numbers of the evaporating droplet by less than 1% compared to a stationary droplet. Hence this gas velocity can be neglected in the calculations of the evaporation rates discussed in the theoretical section of this study. The RH is determined by comparing the evaporation kinetics of a probe droplet, of either NaCl solution or water, to a simulation using the Kulmala model [61]. This method to determine the RH has an accuracy of approximately ±1% and is outlined in greater detail in a previous publication [40]. In addition, the temperature of the CK-EDB chamber was controlled in a range from 0 °C to 25 °C by a recirculating ethylene glycol coolant. The error in the temperature determination using the thermocouple is ±0.5 °C. An overview of this instrument is shown in Figure 2.1a.

A 532 nm CW laser illuminated the droplet, and the resulting scattering pattern caused by the interference between reflection and refraction at the droplet surface, *i.e.* the phase function was collected at an angular range of 24° by a CCD mounted at 45° to the direction of laser propagation. The angular separation between the fringes in the phase function was used to calculate the radius of the droplet using a geometrical optics approximation, with an associated error of ±100 nm [40].

2.2.3 Monodisperse Droplet Chain Instrument

The monodisperse droplet chain setup used in this study was a modified version of an in-house instrument discussed in more detail previously [59, 60]. This instrument consisted of three main subsystems: feeding, imaging, and collection, as illustrated in Figure 2.1b. The specific solution for each experiment was passed through two 0.45 µm pore sized syringe filters (SLHN033NS, EMD Millipore, Darmstadt, Germany) into an S-shaped reservoir with a volume of 3 mL. It was then dispensed using a high-temperature piezoceramic dispenser (MJ-AL-HT-40-8mx, MicroFab Technologies, Plano, Texas, USA), with an ori-

fice diameter of 40 µm. The piezoceramic dispenser was operated by a driver (MD-E-3000 Microdrop Technologies, Norderstedt, Germany), which allowed control over the applied voltage and frequency. The voltage and frequency of the dispenser directly affect the initial diameter, production frequency of the droplets in the chain and the injection velocity. The solution droplets were injected into a heated airflow with a controlled flow rate in a circular flow tube, which had two walls to assist in temperature control. An imaging system with a high magnification lens (35-41-41-000, Excelitas, Fremont, California, USA), attached to a camera (GO-5000M-USB, JAI, Shanghai, China) was used to capture images of the droplet at the injection point which were later analyzed to determine the initial droplet diameter. Dried particles were collected for data analysis at the end of the flow tube using custom-made scanning electron microscope (SEM) sample stubs onto which a membrane filter (0.8 µm Isopore Polycarbonate, Millipore, Darmstadt, Germany) was attached using a double-sided adhesive carbon tape. Collected particles were coated with a vacuum gold sputter (Desk II, Denton Vacuum LLC, Moorestown, NJ, USA) and analyzed using field emission scanning electron microscopy (Sigma FE-SEM, Zeiss, Jena, Germany) with an accelerating voltage of 5 kV and an average working distance of 6 mm. A number of sample particles were also imaged using helium-ion microscopy (ORION NanoFAB HIM with Ga FIB, Zeiss, Jena, Germany) at an accelerating voltage of 29 kV, an average working distance of 9 mm and using a 10 µm aperture; the particles were cut using a gallium-focused-ion beam (Ga-FIB) from the same instrument at an accelerating current of 300 pA with dwell times between 0.5 and 1.0 µs and beam spacing between 2 and 5 nm for fine and rough cuts, respectively.

2.3 Theory and Modeling of Multicomponent Evaporation and Particle Formation

Two different methods of increasing complexity were used to study the evaporation of multicomponent microdroplets relevant to pharmaceutical applications. The first method is based on Maxwell's solution of mass transfer from a

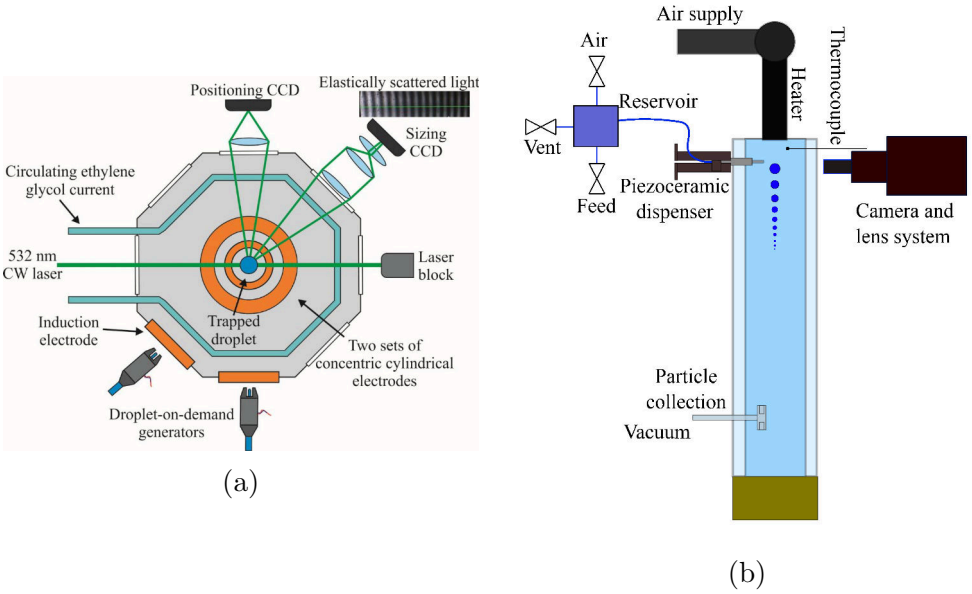

Figure 2.1: The experimental instruments, (a) CK-EDB, (b) Droplet chain setup.

spherical liquid droplet in a quiescent environment [1, 62]. This quasi-steady model was modified for a multicomponent droplet to account for the simultaneous evaporation or condensation of different volatile species [63]. It does not, however, account for the interaction of different vapors in the gas phase and assumes no bulk radial velocity or Stefan flow around the droplet.

The second method is based on the analytical solution of mass and energy transport equations with the inclusion of radial convection in the gas phase. For a single component droplet, this methodology produces the results of Fuchs [53] and is sometimes called the Stefan-Fuchs method [43]. In both of these schemes, the mass transfer of each volatile component in the gas phase is considered independently of the transfer of other species and the diffusion obeys Fick's law [62, 64]. Inclusion of inter-species diffusion effects during the evaporation or condensation of multicomponent droplets requires a full Maxwell–Stefan diffusion model [51] and is beyond the scope of this study; it will be seen later that the simplified models have the required accuracy pertaining to spray drying of pharmaceutical particles.

In both models, some assumptions and simplifications were made based on the specific conditions prevailing in pharmaceutical processes. Some of these

conditions include small droplets (diameters: 5-50 µm), low settling velocity and Reynolds numbers, and low-to-moderate temperatures (less than 150 °C gas temperature). The assumptions are as follows:

1. Spherical symmetry and negligible droplet motion with respect to the gas phase
2. Quasi-steadiness in the gas phase
3. Negligible Soret and Dufour effects and radiation heat transfer
4. Negligible Kelvin effect
5. Continuum regime
6. Infinite thermal and solvent mass diffusivity in the droplet (well-mixed approximation).

The spherical symmetry assumption is justified because of the small size of the droplets encountered in spray drying of pharmaceuticals or emitted from different inhalers. At diameters of less than 50 µm, the settling velocities and relaxation times are small enough to neglect internal convection [1]. The Knudsen number is also small enough at atmospheric conditions to neglect non-continuum corrections. As an example, for an ethanol droplet with a diameter of 50 µm evaporating in air with a temperature of 80 °C, the settling velocity and relaxation time are about 60 mm/s and 6 ms, respectively. The droplets might have larger initial velocities upon atomization but will reach their terminal or settling velocity in a time comparable to the relaxation time. The time it takes for complete evaporation for a droplet of this size at this temperature is about 0.15 s, which is about 25 times the relaxation time. Thus, the initial transient phase is a small fraction of the total droplet lifetime, and the effects of the internal circulation in this phase can be neglected given the longer life span of the droplet. At the terminal velocity, the droplet has a Reynolds number of about 0.14, so that neglecting the relative droplet motion with respect to the gas phase will under-predict the Nusselt and Sherwood numbers by only about 2% [43, 65]. Assuming quasi-steady evaporation

requires that any changes in the boundary conditions at the droplet-gas interface instantaneously appear in the gas conditions around the droplet. In other words, transient effects are neglected in the solution of the mass and energy transports in the gas phase [1, 53, 66]. The characteristic time required for the thermal and composition profiles around a droplet to reach equilibrium, t_{t}, can be approximated as [66, 67]:

$$t_{\mathrm{t}} = \frac{d^2}{16\alpha_{\mathrm{v}}}, \tag{2.1}$$

where d is the droplet diameter and α_{v} is the appropriate diffusivity in the gas phase, *i.e.* either the thermal diffusivity or the mass diffusion coefficient of the vapor. For a 50 µm diameter ethanol droplet in air, the time scales associated with thermal and mass diffusions are approximately equal to 7 and 14 µs, respectively, which are small enough compared to the droplet lifetime to justify the quasi-steady assumption.

Similarly, the well-mixed assumption for the interior of the droplet is based on the low temperature and small diameter ranges encountered in the applications pertaining to this study. At these conditions, the solvent diffusion and thermal conduction is fast enough to assume constant radial profiles for the solvent compositions and temperatures inside the droplet [68].

In both models, numerical integration was performed using a simple first-order Euler method to advance in time. During each time-step, the droplet composition and temperature were updated based on the analytical solutions of the mass and energy transport in the gas phase.

2.3.1 Maxwell Model

In the absence of any bulk radial gas flow, the solution of Fick's law of diffusion with the appropriate boundary conditions provides the mass transfer rate, $\dot{m}$, of a single-solvent droplet as [1]:

$$\dot{m} = -2\pi d D \left(C_{\mathrm{s}} - C_{\infty}\right), \tag{2.2}$$

in which d is the droplet diameter and D is the binary diffusion coefficient of the vapor in the gas. C_{s} and C_{∞} are the vapor mass concentrations near the droplet surface and at infinity, respectively.

If it can be assumed that the diffusion of each volatile component in the gas phase is independent of the others, different mass transfer rates of separate species of a multicomponent droplet can be superimposed in accordance with Equation (2.2). Hence, the total mass transfer rate from the droplet, $\dot{m}_{\mathrm{t}}$, can be obtained from the following equation:

$$\dot{m}_{\mathrm{t}} = \sum \dot{m}_i = \sum_i -2\pi d D_{\mathrm{v},i} \left(C_{\mathrm{s},i} - C_{\infty,i}\right) \tag{2.3}$$

in which $D_{\mathrm{v},i}$ is the diffusion coefficient of the ith volatile component in the gas mixture at an intermediate temperature and gas composition, which will be discussed later (*cf*. Equations (2.11) and (2.12)). By assuming equilibrium between the vapor and the liquid phases at the interface, the surface vapor concentration, $C_{\mathrm{s},i}$, can be obtained from the modified Raoult's law as:

$$C_{s,i} = x_{\mathrm{ls},i} \frac{P_{\mathrm{sat},i}\left(T_{\mathrm{d}}\right) M_i}{R T_{\mathrm{d}}} \gamma_i \ , \tag{2.4}$$

where $x_{\mathrm{ls},i}$ is the molar fraction of the ith component in the liquid at the surface, and $P_{\mathrm{sat},i}\left(T_{\mathrm{d}}\right)$ is the saturation vapor pressure, which can be obtained from Clausius–Clapeyron or Antoine equations at the droplet temperature, T_{d}. M_i and γ_i are the molar mass and activity coefficient of the ith component, respectively, and R is the universal gas constant. In this study, the activity coefficients were calculated using the NRTL method [69]. The vapor concentration far away from the droplet can be obtained from the partial pressure of each component, $P_{\infty,i}$, as:

$$C_{\infty,i} = \frac{P_{\infty,i} M_i}{R T_{\infty}}. \tag{2.5}$$

To find the droplet temperature according to the infinite thermal conductivity or lumped-capacitance assumption inside the droplet, the following relationship was used [1]:

$$\rho_{\mathrm{l}} c_{\mathrm{p,l}} \frac{d^2}{12} \frac{\mathrm{d}T_{\mathrm{d}}}{\mathrm{d}t} = -\bar{k}\left(T_{\mathrm{d}} - T_{\infty}\right) - \sum L_i D_{\mathrm{v},i}\left(C_{\mathrm{s,i}} - C_{\infty,i}\right), \tag{2.6}$$

where ρ_{l} is the liquid mixture density, $c_{\mathrm{p,l}}$ is the specific heat of the liquid mixture, $\bar{k}$ is the gas thermal conductivity at the intermediate conditions and L_i is the latent heat of vaporization of each material.

At each time-step, Equations (2.3) and (2.6) were solved and the composition and temperature of the droplet were updated. In order to obtain the droplet size, the following mass balance was used:

$$\frac{\pi}{6}\frac{\mathrm{d}\left(\rho_{\mathrm{l}}d^{3}\right)}{\mathrm{d}t}=\dot{m}_{\mathrm{t}}. \tag{2.7}$$

Noting that the composition and the temperature of the droplet can change temporally, Equation (2.7) could be rewritten as:

$$\frac{\mathrm{d}d}{\mathrm{d}t}=\frac{2\dot{m}_{\mathrm{t}}}{\pi\rho_{\mathrm{l}}d^{2}}-\frac{d}{3\rho_{\mathrm{l}}}\frac{\mathrm{d}\rho_{\mathrm{l}}}{\mathrm{d}t}. \tag{2.8}$$

By knowing the new and previous droplet compositions and temperatures, the time derivative of the droplet density could be approximated using first order discretization, and the new droplet diameter was obtained at the end of each time-step. Using Equation (2.8), the thermal and compositional expansion and shrinkage of the droplet could be accurately modeled if an accurate correlation for the mixture density was used. For instance, for water/ethanol mixtures, the following semi-empirical relationship was used [70]:

$$\begin{aligned}\ln\rho_{\mathrm{l}}=x_{\mathrm{l,w}}\ln\rho_{\mathrm{l,w}}+x_{\mathrm{l,eth}}\ln\rho_{\mathrm{l,\ eth}}\ -30.808\left(\frac{x_{\mathrm{l,w}}x_{\mathrm{l,\ eth}}}{T_{\mathrm{d}}}\right)\\ -18.274\left[\frac{x_{\mathrm{l,w}}x_{\mathrm{l,eth}}\left(x_{\mathrm{l,w}}-x_{\mathrm{l,eth}}\right)}{T_{\mathrm{d}}}\right]+13.89\left[\frac{x_{\mathrm{l,w}}x_{\mathrm{l,\ eth}}\ \left(x_{\mathrm{l,w}}-x_{\mathrm{l,\ eth}}\ \right)^{2}}{T_{\mathrm{d}}}\right],\end{aligned} \tag{2.9}$$

where $x_{\mathrm{l,w}}$ and $x_{\mathrm{l,eth}}$ are the mole fractions of water and ethanol in the droplet, respectively; $\rho_{\mathrm{l,w}}$ and $\rho_{\mathrm{l,eth}}$ are their respective temperature-dependent liquid densities in $\mathrm{kg/m^3}$ and T_{d} is the droplet temperature in K. In the absence of such empirical relations for the mixture of interest, one can use the following relationship for the mixture density assuming ideal mixing:

$$\frac{1}{\rho_{\mathrm{l}}}=\sum\frac{y_{\mathrm{l},i}}{\rho_{\mathrm{l},i}}, \tag{2.10}$$

where, $y_{\mathrm{l},i}$ and $\rho_{\mathrm{l},i}$ are the mass fraction and liquid density of the ith component in the droplet, respectively.

As mentioned previously, the transport properties in the gas phase of the droplet-gas interface were assumed to be radially constant. In this study, a 1/3 approximation was used [32, 43], according to which the intermediate

temperature, $\bar{T}$, and intermediate mass fraction of the ith component in the gas phase, $\bar{y}_{\mathrm{g},i}$, are

$$\bar{T} = \frac{2}{3}T_{\mathrm{d}} + \frac{1}{3}T_{\infty} \tag{2.11}$$

and

$$\bar{y}_{\mathrm{g},i} = \frac{2}{3}y_{\mathrm{s,g},i} + \frac{1}{3}y_{\infty,\mathrm{g},i} \ , \tag{2.12}$$

where $y_{\mathrm{s,g},i}$ and $y_{\infty,\mathrm{g},i}$ are the mass fractions of the ith volatile component in the gas phase, near the surface and far from the surface of the droplet, respectively. This approximation becomes defective at very high drying gas temperatures, as observed in spray combustion applications; but it is sufficiently accurate for the mild temperatures encountered in pharmaceutical processes. These intermediate conditions are updated at the start of each time-step based on the droplet temperature of the last step.

2.3.2 Stefan-Fuchs Model

In the second model, the effects of the radial convection or Stefan Flow were considered. The governing transport equations in the gas phase were the mass transfer equations of the inert gas (*e.g.* air) and each of the volatile components as well as the energy transfer equation [50, 62, 64].

The quasi-steady equations governing the species transfer around the droplet for the inert gas and each component i were as follows:

$$\frac{\mathrm{d}}{\mathrm{d}r}\left\{4\pi r^2 n_{\mathrm{inert}}\right\} = \frac{\mathrm{d}}{\mathrm{d}r}\left\{4\pi r^2\left(C_{\mathrm{inert}}U - D_{\mathrm{inert,m}}\cdot\rho_{\mathrm{t}}\frac{\mathrm{d}y_{\mathrm{inert}}}{\mathrm{d}r}\right)\right\} = 0, \tag{2.13}$$

$$\frac{\mathrm{d}}{\mathrm{d}r}\left\{4\pi r^2 n_i\right\} = \frac{\mathrm{d}}{\mathrm{d}r}\left\{4\pi r^2\left(C_i U - D_{i,\mathrm{m}}\cdot\rho_{\mathrm{t}}\frac{\mathrm{d}y_{\mathrm{g},i}}{\mathrm{d}r}\right)\right\} = 0, \tag{2.14}$$

where n_{inert}, C_{inert}, $D_{\mathrm{inert,m}}$ and y_{inert} are the mass flux, mass concentration, diffusion coefficient in the mixture at the intermediate conditions and mass fraction of the inert gas, respectively. Similarly, n_i, $C_{\mathrm{g},i}$, $D_{i,\mathrm{m}}$ and $y_{\mathrm{g},i}$ are the mass flux (*i.e.* transferred mass per time and cross sectional area), mass concentration, diffusion coefficient in the gas mixture at the intermediate conditions (obtained from Equations (2.11) and (2.12)) and mass fraction of each volatile component i. U and ρ_{t} are the bulk radial velocity of the gas and

total gas density, respectively, and r is the radial coordinate. The summation of Equations (2.13) and (2.14) results in a relationship for the radial velocity, U, assuming that the inert gas mass flux, n_{inert}, is zero everywhere (due to the negligible solubility of air in the droplet). To write an explicit expression for the total evaporation rate from the droplet as a function of the radial velocity, it is usual to assume that the diffusion coefficients of all the components, including air, are equal. Note that the correct diffusion coefficient of each volatile component is maintained during the derivation of individual evaporation rates [64]. The radial velocity is then given by:

$$U = -\frac{\dot{m}_{\text{t}}}{4\pi r^2 \rho_{\text{t}}}. \tag{2.15}$$

Note that this equation is an approximation that is valid when the droplet density is much higher than the gas phase density, which is a reasonable assumption in this study. Combining Equations (2.13) and (2.15) and noting again that the mass flux of the inert gas (*i.e.* air) is zero results in an ordinary differential equation for the mass fraction of the inert gas whose solution, using the appropriate boundary conditions, gives [62, 64]:

$$\dot{m}_{\text{t}} = -2\pi d \rho_{\text{t}} D_{\text{inert,m}} \ln\left(\frac{y_{\infty,\text{inert}}}{y_{\text{s,inert}}}\right) \tag{2.16}$$

where $y_{\infty,\text{inert}}$ and $y_{\text{s,inert}}$ are the inert gas mass fractions far away from the droplet and near the surface, respectively. This relationship is the same as the one obtained by Fuchs for a single component droplet [53]. The next step is to find the contribution of each individual volatile component to the droplet mass transfer by combining Equations (2.14) and (2.15) to result in a second order differential equation for the mass fractions of each of these components, the solution of which gives a relationship for $y_i(r)$ [64]. To find $\dot{m}_i$, note that:

$$\dot{m}_i = -\pi d^2 n_i\big|_{r=\frac{d}{2}} = -\pi d^2 \left(C_i U|_{r=\frac{d}{2}} - \rho_{\text{t}} D_{i,\text{m}} \frac{\mathrm{d}y_i}{\mathrm{d}r}\bigg|_{r=\frac{d}{2}} \right). \tag{2.17}$$

Combining Equation (2.17) with Equation (2.15) and the relationship obtained for $y_i(r)$, gives

$$\dot{m}_i = -2\pi d \rho_{\text{t}} D_{\text{inert,m}} \ln\left(\frac{y_{\infty,\text{inert}}}{y_{\text{s,inert}}}\right) \frac{y_{\infty,i}\beta_i - y_{\text{s},i}}{\beta_i - 1} = \dot{m}_{\text{t}} \frac{y_{\infty,i}\beta_i - y_{\text{s},i}}{\beta_i - 1}, \tag{2.18}$$

where $y_{\infty,i}$ and $y_{\mathrm{s},i}$ are the vapor mass fractions of the ith component far away from the droplet and near the surface, respectively, and

$$\beta_i = \left(\frac{y_{\mathrm{s,inert}}}{y_{\infty,\mathrm{inert}}} \right)^{\frac{D_{\mathrm{inert,m}}}{D_{i,\mathrm{m}}}}.$$

A careful examination of Equation (2.18) reveals several important points. First, if there is only one solvent, then $D_{\mathrm{inert,m}}/D_{i,\mathrm{m}} = 1$ and this in turn will result in $\dot{m}_i/\dot{m}_{\mathrm{t}} = 1$ as expected. Second, if $\dot{m}_{\mathrm{t}} \to 0$ or $y_{\infty,\mathrm{inert}}/y_{\mathrm{s,inert}} \to 1$, then $\ln\left(y_{\infty,\mathrm{inert}}/y_{\mathrm{s,inert}}\right) \approx \left(y_{\infty,\mathrm{inert}}/y_{\mathrm{s,inert}}\right) - 1$ and $\beta_i \approx 1 + \left(D_{\mathrm{inert,m}}/D_{i,\mathrm{m}}\right)$ $\left(y_{\mathrm{s,inert}}/y_{\infty,\mathrm{inert}} - 1\right)$. If we define $\eta = y_{\mathrm{s,inert}}/y_{\infty,\mathrm{inert}}$, then:

$$\lim_{\eta\to 1} \dot{m}_i = -2\pi d \rho_{\mathrm{t}} D_{\mathrm{inert,m}} \lim_{\eta\to 1} \left\{ \left(\frac{1}{\eta} - 1 \right) \frac{y_{\infty,i}\left[1 + \frac{D_{\mathrm{inert,m}}}{D_{i,\mathrm{m}}}(\eta - 1)\right] - y_{\mathrm{s},i}}{1 + \frac{D_{\mathrm{inert,m}}}{D_{i,\mathrm{m}}}(\eta - 1) - 1} \right\}.$$

Noting

$$\lim_{\eta\to 1} \frac{\frac{1}{\eta} - 1}{\eta - 1} = \lim_{\eta\to 1} \frac{\frac{1-\eta}{\eta}}{\eta - 1} = -1,$$

the following is obtained in the limiting case when $\dot{m}_{\mathrm{t}}$ is approximately equal to zero:

$$\dot{m}_i = -2\pi d \rho_{\mathrm{t}} D_{\mathrm{inert,m}} \left(y_{\mathrm{s},i} - y_{\infty,i} \right).$$

In this limiting case, the radial convection or Stefan flow vanishes, which is evident from Equation (2.15), and this equation is similar to Equation (2.3) based on Maxwell's solution. Note that individual components might have non-zero contributions to the droplet evaporation or condensation, but the total evaporation rate of the droplet can be zero when these contributions cancel each other out.

Lastly, as also noted in [64], there is a problem of inconsistency with Equation (2.18), since $\sum \dot{m}_i$ is not equal to $\dot{m}_{\mathrm{t}}$ from Equation (2.16). This is due to the previous assumption of equal mass diffusivities for different species in deriving Equation (2.16). The error due to this inconsistency is relatively small in most practical applications, as the vapor diffusivities of most species of interest are comparable.

The energy equation for the gas phase also contains the radial convective term shown in the following differential equation:

$$\frac{\mathrm{d}^2T}{\mathrm{d}r^2} + \left(\frac{2}{r} + \alpha_\mathrm{t}\frac{1}{r^2}\right)\frac{\mathrm{d}T}{\mathrm{d}r} = 0, \tag{2.19}$$

where

$$\alpha_\mathrm{t} = \frac{\sum \dot{m}_i c_{\mathrm{p,g},i}}{4\pi\bar{k}},$$

here $c_{\mathrm{p,g},i}$ is the specific heat of each vapor species. The solution of this equation with the boundary conditions at infinity, T_∞, and near the droplet surface, T_d, gives:

$$T(r) = \frac{1}{\mathrm{e}^{\frac{2\alpha_\mathrm{t}}{d}} - 1}\left[\left(T_\infty \mathrm{e}^{\frac{2\alpha_\mathrm{t}}{d}} - T_\mathrm{d}\right) - \left(T_\infty - T_\mathrm{d}\right)\mathrm{e}^{\frac{\alpha_\mathrm{t}}{r}}\right]. \tag{2.20}$$

The heat transfer to the droplet can be obtained from Equation (2.20) and used in the equation of energy balance for the droplet to give:

$$\frac{\mathrm{d}T_\mathrm{d}}{\mathrm{d}t} = \frac{6}{\rho_\mathrm{l} c_\mathrm{p,l}\pi d^3}\left[\frac{4\pi\bar{k}\alpha_\mathrm{t}}{e^{-\frac{2\alpha_\mathrm{t}}{d}} - 1}\left(T_\mathrm{d} - T_\infty\right) + \sum L_i \dot{m}_\mathrm{i}\right]. \tag{2.21}$$

2.3.3 Internal Solute Diffusion

The internal distribution of different solutes plays an important role in determining the dried particle morphology [32, 33]. As the droplets shrink during drying, there is a tendency for the solutes to enrich the surface. The established concentration gradient will cause the solute molecules to diffuse to the center of the droplet, in accordance with Fick's law of diffusion. Hence, the amount of surface enrichment is a consequence of two competing effects, the evaporation rate, κ, and the diffusion rate of each specific solute. The evaporation rate is defined as:

$$\kappa = -\frac{\mathrm{d}d^2}{\mathrm{d}t}. \tag{2.22}$$

A careful scale analysis of Fick's second law of diffusion in an evaporating droplet shows that the competition of these mechanisms can be characterised by the Péclet number, Pe_j, defined as [14, 32]:

$$Pe_j = \frac{\kappa}{8D_j}, \tag{2.23}$$

in which D_j is the diffusion coefficient of the jth solute in the droplet. A very large Péclet number, much larger than one, is consistent with a surface recession that is much faster than diffusion. This fact results in much larger surface concentrations of the solute than the average concentration inside the droplet, while the concentrations at other radial positions away from the surface are relatively constant and smaller. At the other extreme, with Péclet numbers less than one, the concentration is relatively uniform throughout the droplet. Péclet numbers between these two extremes will result in smooth concentration profiles with a minimum at the center and a maximum at the surface during evaporation. Note that these discussions are only valid under spherical symmetry inside and around the droplet and in the absence of internal convective transport.

For a solution droplet with only one solvent, both the evaporation rate and the diffusion coefficients of different species can often be assumed constant during the evaporation process, resulting in a constant Péclet number for each solute. This assumption is good as long as the dependence of the diffusion coefficient on the solute concentration can be neglected, *i.e.* at moderate to low concentrations [71]. For this case, an analytical model, known as the VFL model [32, 33], was previously developed to calculate the steady-state surface enrichment of each solute from the Péclet number. Surface enrichment, E_j, is defined as the instantaneous surface concentration of each solute, $C_j(d/2, t)$, divided by the instantaneous mean concentration of that solute, $C_{m,j}(t)$. These concentrations should not be confused with the vapor concentrations from the previous sections. In general, for a constant Péclet number, the surface enrichment undergoes a transient stage before converging to a constant value. The VFL model gives this steady-state surface enrichment value as [32]:

$$E_{j,\text{steady}} = \frac{C_j\left(\frac{d}{2}, t\right)}{C_{\text{m},j}(t)} = 1 + \frac{Pe_j}{5} + \frac{Pe_j^2}{100} - \frac{Pe_j^3}{4000} \tag{2.24}$$

which is applicable for $Pe_j < 20$. The unsteady Fickian diffusion of solutes inside a single solvent droplet with a constant evaporation rate was solved in another study to account for the initial transient stages of the surface enrichment, and different correlations for different Péclet number regimes were

presented [33]. It was concluded that the initial transient stage is very short compared to the total droplet lifetime at small Péclet numbers, less than ~ 0.5. At larger Péclet numbers, the surface enrichment converges to the steady value only near the end of the droplet lifetime.

In the case of solutions with more than one volatile solvent, both the evaporation rate and the diffusion coefficients generally change with time, resulting in a time-varying Péclet number. This fact requires the numerical solution of the internal diffusion of each solute at each time-step to obtain the concentration profiles. The one-dimensional Fick's law of diffusion inside an evaporating droplet in the spherical coordinate system is [33]:

$$\frac{\partial C_j}{\partial t} = \frac{4D_j}{d^2}\left(\frac{\partial^2 C_j}{\partial R^2} + \frac{2}{R}\frac{\partial C_j}{\partial R}\right) - \frac{\kappa R}{2d^2}\frac{\partial C_j}{\partial R}, \tag{2.25}$$

where $R = r/(d(t)/2)$ is the non-dimensional radial coordinate, d is the instantaneous diameter of the droplet and κ, the evaporation rate, is obtained from one of the two different methodologies discussed in the previous subsections. The appropriate initial and boundary conditions of this second order partial differential equation are:

$$\begin{cases} C_j = C_{0,j} & t = 0 \\ \frac{\partial C_j}{\partial R} = 0 & R = 0 \\ D_j \frac{\partial C_j}{\partial R} - \frac{\kappa}{8} C_j = 0 & R = 1 \end{cases}$$

D_j is assumed to be constant in the radial direction in arriving at Equation (2.25). In the case of a single solvent, D_j can be approximated as the diffusion coefficient at infinite dilution of each specific solute in the solvent as the effects of increasing concentration on the diffusion coefficients are neglected in the current study. The diffusion inside a droplet composed of more than one solvent is more complicated, and in general the use of a binary diffusion equation such as Equation (2.25) is not accurate. One could solve the Maxwell-Stefan or generalized Fick's equations to account for the interspecies diffusion [72]. However, the solution of these equations requires knowledge of every binary diffusion coefficient of every component, either solvent or solute, in the other components to make up the diffusion coefficient matrix, which makes the use of such diffusion equations impractical in most cases. Instead,

it is assumed that each solute behaves as if it were at infinite dilution in a single solvent, with the diffusion coefficient equal to a value dependent on the binary diffusion coefficients of this specific solute in each of the solvents as well as on the composition of the solvents. This simplification gives an exact relationship for dilute ideal gas mixtures based on Maxwell-Stefan theory [73, 74] but introduces an error for dense gases and non-ideal liquids [72]. For the water and ethanol binary system, the following relationship was shown to be more accurate for the effective binary diffusion of solute j in the mixture, D_j [75]:

$$D_j\sqrt{\eta_{\mathrm{m}}} = x_{\mathrm{l,w}}D_{j,\mathrm{w}}\sqrt{\eta_{\mathrm{l,w}}} + x_{\mathrm{l,eth}}D_{j,\mathrm{eth}}\sqrt{\eta_{\mathrm{l,eth}}}, \tag{2.26}$$

were η_{m}, $\eta_{\mathrm{l,w}}$ and $\eta_{\mathrm{l,eth}}$ are the liquid viscosity of the mixture, water, and ethanol at the droplet temperature, respectively. $D_{j,\mathrm{w}}$ and $D_{j,\mathrm{eth}}$ are the binary diffusion coefficients of solute j in water and ethanol, respectively, which, if unknown, can be calculated using the Stokes-Einstein equation [76].

In this study, after the calculation of droplet temperature, evaporation rate and solvent compositions at the end of each time-step, Equation (2.25) is solved numerically to give the radial concentration distribution of each solute inside the droplet. These distribution profiles can then be used to find the relevant particle formation thresholds, such as the time to reach saturation, time to reach true density, etc [14].

2.4 Results and Discussions

2.4.1 Evaporation of Water/Ethanol Microdroplets

In order to study the accuracy and applicability of the two reviewed models, namely the Maxwell and Stefan-Fuchs models, mixtures of water and ethanol were considered due to their safety and their potential in the pharmaceutical industry for the spray drying of inhalable microparticles. This mixture was specifically difficult to study numerically and experimentally because of its associated highly non-ideal behavior. The evaporation CK-EDB measurements of microdroplets of the pure solvents at two different temperatures and 0% relative humidity are compared with the two different models in Figure 2.2.

These plots were normalized by the initial droplet diameter squared to permit the comparison of different sized droplets in a single figure [49]. The experiments conducted with the CK-EDB had uncertainties in temperature and relative humidity of about ±1.5 °C and ±1%, respectively. The initial droplet diameters ranged from 40 to 52 µm in these experiments and, in all of the simulations in this study, the initial droplet temperature was equal to 20 °C, unless stated otherwise. In the experiments, the initial droplet diameters were obtained from retrograde extrapolation of a number of consecutive data points, as the diameter could only be measured using light scattering once the droplets were trapped inside the balance, not immediately upon generation. Typically, five experiments were conducted for each case resulting in the error bars in Figure 2.2, calculated from the standard deviation of the size at each time point. These error bars do not account for the different uncertainties of the experimental procedure such as those caused by the temperature and relative humidity measurements. At these low ambient temperatures, the differences between the Maxwell and Stefan-Fuchs models were negligible. There was good agreement between both models and the experimental data, showing that both models were suitable for single solvent systems at low temperatures.

The evaporation curves of a mixture of 0.3:0.7 w/w water/ethanol at three different gas temperatures are compared in Figure 2.3. Good agreement was observed between the experimental and numerical data including the changes in the evaporation rates due to compositional variation of the droplets. There were small differences between the measured and simulated droplet diameters, which besides the experimental uncertainty, were likely due to the simplifications in the numerical model such as the well-mixed and quasi-steady assumptions, as well as the inaccuracies in the material properties and activity coefficients. Specifically, the time at which ethanol was depleted from the droplet, seen as the sharp change in the slope of the plots, was slightly overpredicted in the model.

The evaporation histories for three different water and ethanol mixtures, all at 20 °C gas temperature, are shown in Figure 2.4a. The point at which the evaporation rate was suddenly reduced, due to the ethanol depletion inside

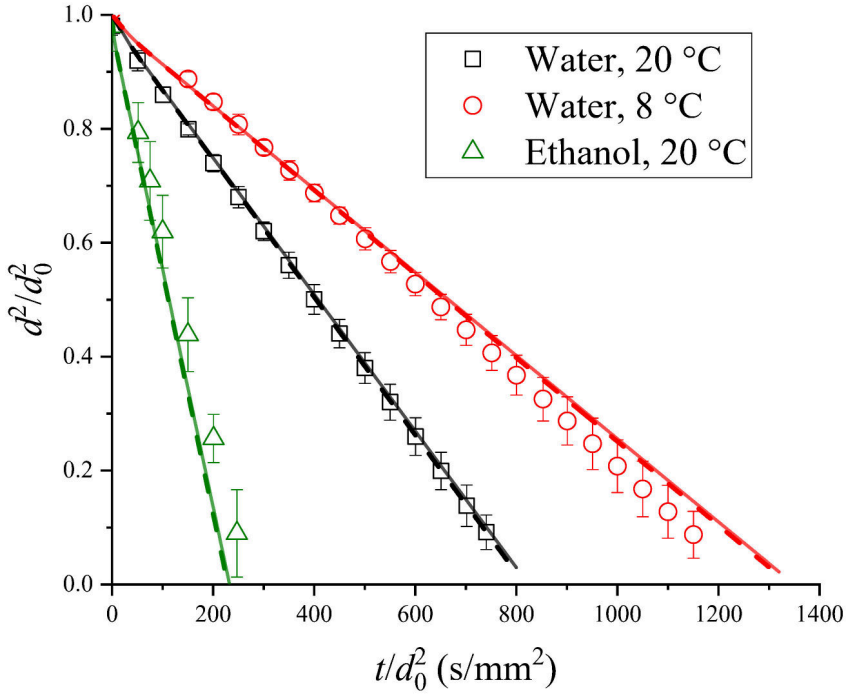

Figure 2.2: Evaporation histories of water and ethanol microdroplets at different temperatures and 0% RH. Symbols: Experimental CK-EDB data, solid lines: Stefan-Fuchs model, dashed lines: Maxwell model.

the droplet, was delayed by decreasing the water content to a point at which the change in evaporation rate was no longer experimentally observed. At this point, the numerically predicted evaporation rate displayed an increasing trend as seen in the 0.2:0.8 w/w water/ethanol case. This phenomenon can also be seen from the predicted evolution of the water mass fraction as shown in Figure 2.4b, in which the droplet evolved into a water-rich composition for the cases of lower ethanol content, while in the last case the opposite was observed. These observations point to an intermediate composition at which the mixture had a relatively constant fraction [49]. This important scenario will be discussed in more detail later.

In actual spray drying applications, the drying temperatures are much higher than those studied above. In order to confirm the validity of the model and compare the Maxwell and Stefan-Fuchs models at elevated temperatures, evaporation histories of some mixtures of water and ethanol at 200 °C are compared to the numerical results of Lupo and Duwig [49] in Figure 2.5. The

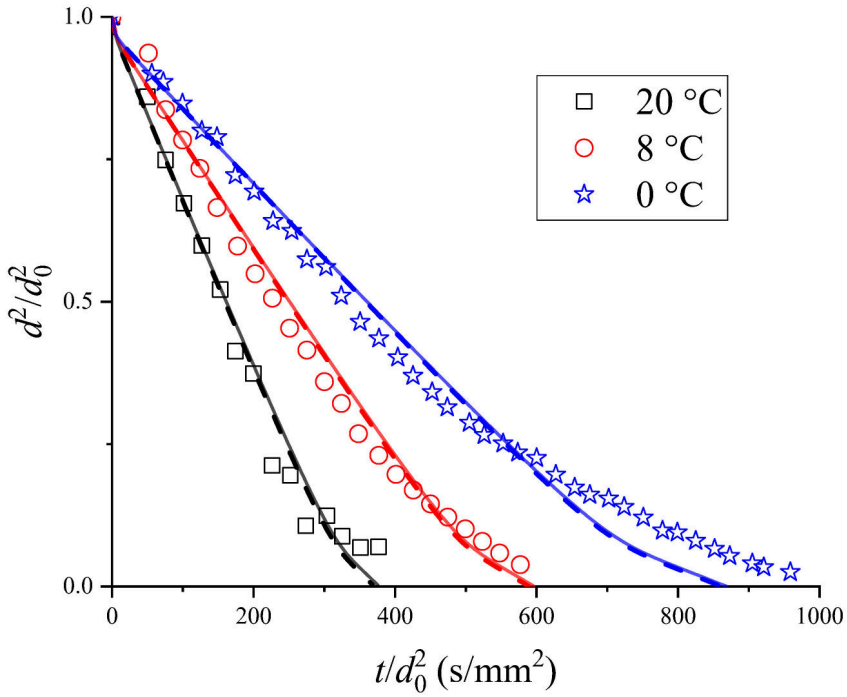

Figure 2.3: Evaporation histories of 0.3:0.7 w/w water/ethanol mixtures at three different temperatures. Symbols: Experimental CK-EDB data, solid lines: Stefan-Fuchs model, dashed lines: Maxwell model.

Stefan-Fuchs model showed close agreement with their results, even though there were two major differences between the models. First, they modeled the internal solvent and heat diffusion explicitly, while a well-mixed droplet was assumed here. Second, they used an average value for the vapor diffusion coefficient of different solvents, while we retained the diffusion coefficients of each specific vapor in Equation (2.18). These differences are suspected to be responsible for the small dissimilarities between their model and the Stefan-Fuchs model, while as expected the Maxwell model deviates more significantly. Even the Maxwell model overpredicted the evaporation rates by less than 20% at this high temperature, which in turn would overpredict the Péclet number by the same value. This overprediction is likely an acceptable error in qualitative particle formation studies, considering the presence of other uncertainties. Hence, either model can be considered acceptable for most particle engineering studies aimed at process design.

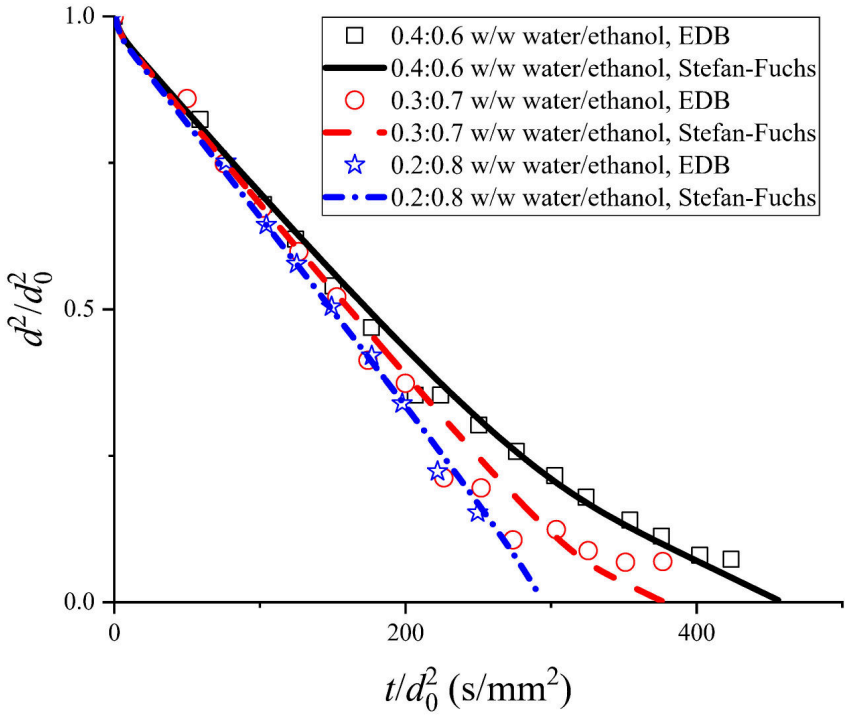

(a)

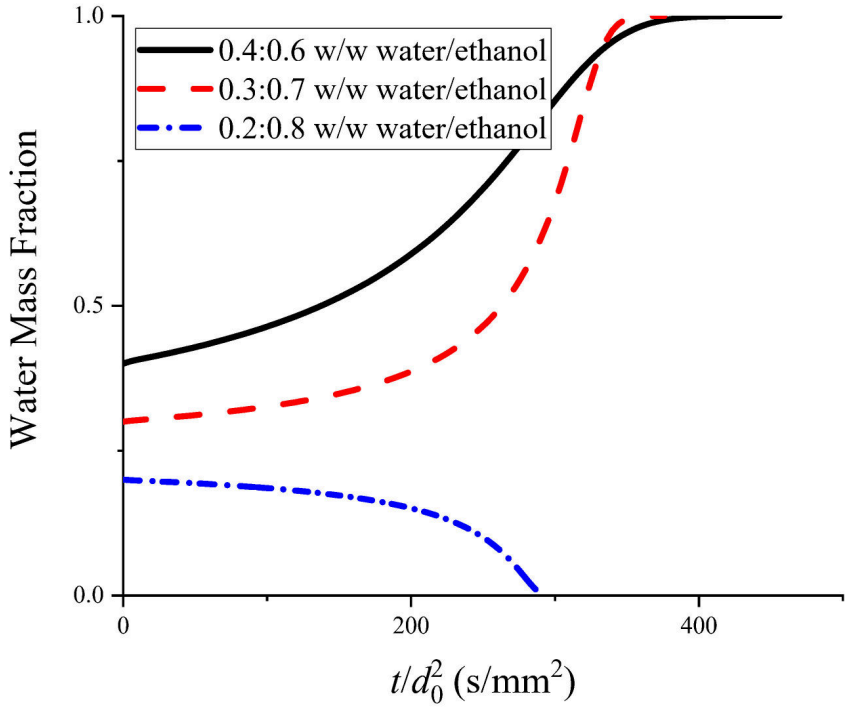

(b)

Figure 2.4: (a) Evaporation histories of three different compositions of water and ethanol at 20 °C, (b) their predicted water mass fraction histories.

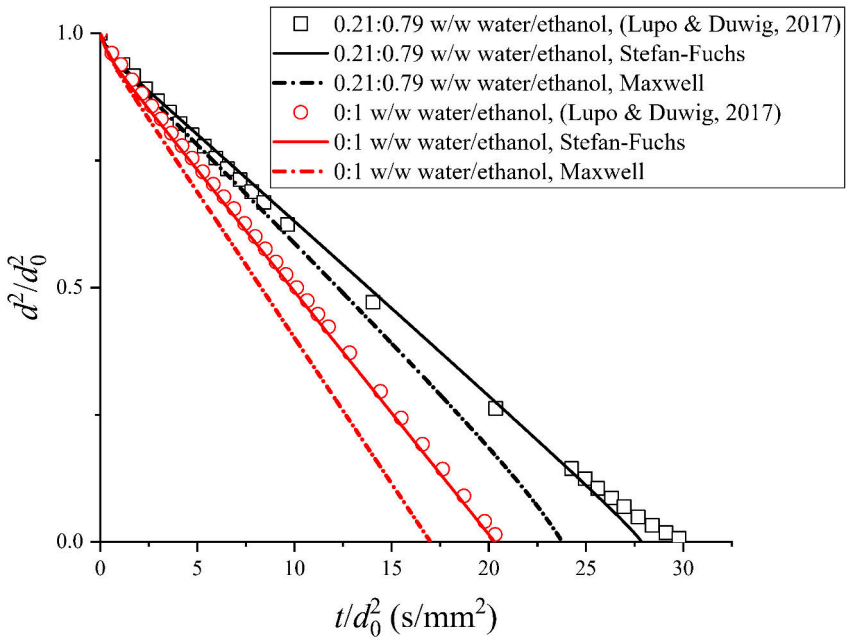

Figure 2.5: Evaporation histories of some water and ethanol mixtures using both the Stefan-Fuchs and Maxwell models compared to another numerical work at 200 °C [49].

2.4.2 Iso-Compositional Drying

It is well known in the distillation and boiling literature that the proportions of certain compositions of liquid mixtures remain constant during boiling. These specific compositions are called azeotropes of the mixture, whose vapors maintain the exact same composition during boiling [77]. For example, a water/ethanol mixture at 101 kPa with 95.57% water by mass will boil at a constant temperature of 78.15 °C while maintaining this composition [78]. An evaporating multicomponent droplet might also show similar behavior at a specific composition and ambient temperature, relative humidity, and pressure, which conditions we shall collectively call the iso-compositional drying, with the composition of the droplet constant for the majority of the droplet's lifetime. The evaporation rate, the Péclet number, droplet temperature, different solute solubilities and all other temperature- and composition-dependent properties of the droplet will also remain constant. These facts simplify the particle formation study, as the system behaves as a single-solvent solution and all the previous studies on the particle formation of such systems can be

employed [32, 33]. It is worthwhile to note that this "iso-compositional" state might or might not happen for different solvents, as it is strongly related to the level of non-ideality of the components and their vapor pressures [79]. For example, for ideal mixtures, no possible iso-compositional evaporation of the droplet can be achieved at any temperature or composition as discussed in more detail in [79]. For an evaporating droplet to be iso-compositional during drying, the following relationship must hold:

$$\frac{\dot{m}_i}{\dot{m}_\mathrm{t}} = y_{\mathrm{l},i}. \tag{2.27}$$

In other words, the fractional evaporation rate of each species should be equal to its mass fraction inside the droplet. Using Equations (2.18) and (2.27) and relating the surface vapor mass fractions to the liquid mass fractions, one can arrive at an implicit equation to solve for the specific iso-composition. However, the solution is complicated as the droplet temperature is unknown and therefore requires an iterative procedure. Alternatively, for the specific case of ethanol/water mixtures in this study, the initial droplet composition was varied to identify a nearly constant water composition during the drying to arrive at the iso-composition at the specific drying temperature and relative humidity. For example, the iso-composition at a drying temperature of 20 °C and in dry air was obtained using a plot similar to the one shown in Figure 2.6, which shows the dependence of the instantaneous water mass fraction normalized by the initial water fraction on the time normalized by the total drying time of the droplet. The initial mass fraction around the suspected iso-compositional point was varied by 0.1% to approximate this value accurate to ±0.1%. At these conditions, the iso-compositional water mass fraction was estimated to be about 23.7%. As seen from Figure 2.6, when the water content is less than the iso-compositional value, the water will evaporate completely before the ethanol, and there will be an increase in the ethanol content with time. The reverse is observed for water contents higher than the iso-compositional value. The same procedure was performed for other drying temperatures ranging from 10 °C to 200 °C and at 0% RH, all with an initial droplet temperature of 20 °C. The iso-compositional mass fractions and the wet-bulb temperatures

for this temperature range are shown in Figure 2.7. It is observed that the iso-composition was relatively constant and equal to 23.7% between 10 °C and 40 °C with a small decrease above this temperature range reaching a value equal to 22.6% at 200 °C. This small variation of the iso-compositional fractions with temperature simplifies the formulation design in an actual spray-dryer, whose drying gas temperature gradients are generally large. The droplet temperature or the wet-bulb temperature also increased steadily with a decreasing slope when the drying gas temperature was increased. Even at a drying gas temperature of 200 °C, a typical maximum temperature for the spray drying of pharmaceuticals, the droplet temperature was only about 34 °C due to the evaporative cooling—well below the boiling temperature of the azeotrope of water and ethanol at atmospheric pressure, which is about 78.15 °C. This fact encouraged the use of the term "iso-compositional point" instead of the "azeotropic point" in this study.

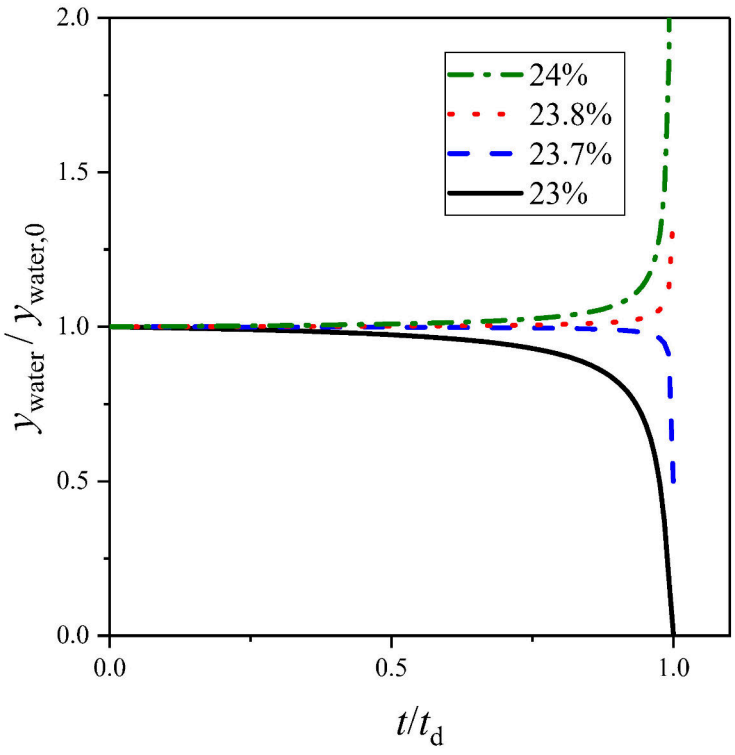

Figure 2.6: The composition variation of a water/ethanol droplet with different initial water mass fractions in dry air at 20 °C, used to find the iso-compositional point.

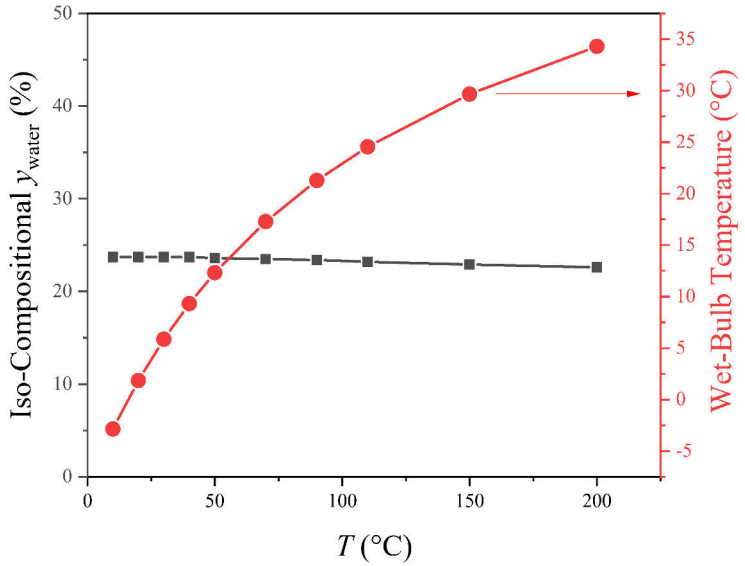

Figure 2.7: The iso-compositional water mass fractions of water/ethanol mixtures and the corresponding droplet temperatures at different drying temperatures in dry air.

The evaporation rates, κ, of the water/ethanol mixtures at the calculated iso-compositions, accompanied by the evaporation rates of the pure solvents, are shown in Figure 2.8. It was also observed that the evaporation rate at the iso-compositional point was approximately equal to the molar weighted average of the evaporation rates of pure water and ethanol at the respective drying temperature.

Spray drying in iso-compositional conditions holds some advantages during the formulation and process design of pharmaceutical aerosols, where predicting the evaporation rates of the solution droplets is an important step [32, 33]. First, as mentioned before, temperature, composition and all the dependent properties such as the solubility values of the solutes are constant, greatly simplifying the calculations pertaining to particle design. Furthermore, some of the hydrophobic corticosteroids such as beclometasone dipropionate (BDP) and budesonide (BUD) have a maximum solubility close to this iso-composition in water/ethanol mixtures as shown in Figure 2.9. For BDP the solubility at the iso-composition is about 40% greater than that in pure ethanol, while for BUD this increase is about 10%. Hence, for a given initial droplet size, a single spray-dried particle of BUD or BDP at the iso-composition can contain 40%

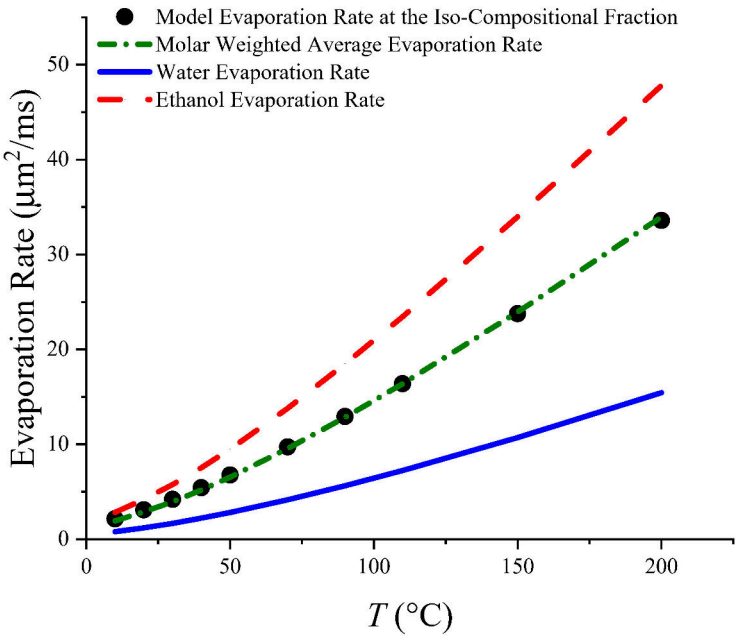

Figure 2.8: The evaporation rates, κ, of water/ethanol mixtures at the iso-compositional point compared to those of pure components and the molar weighted average.

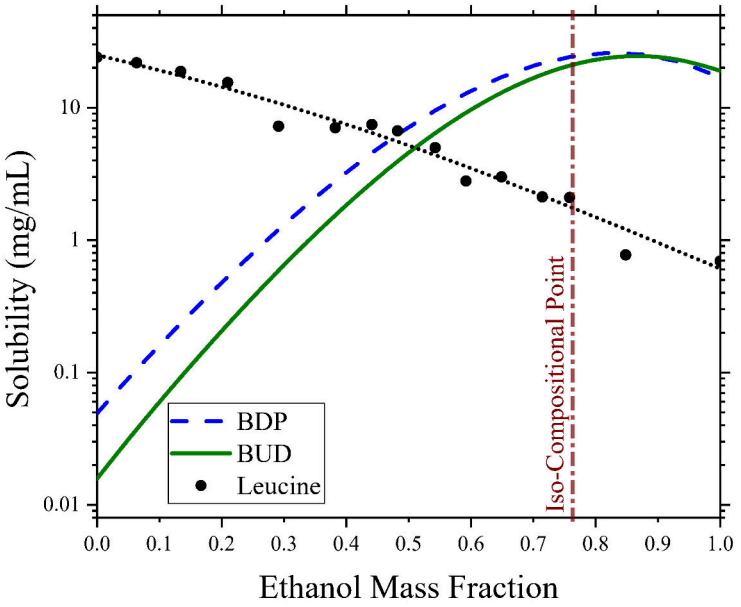

Figure 2.9: Equilibrium solubility values of beclometasone dipropionate (BDP), budesonide (BUD) and leucine in water/ethanol mixtures at 25 °C. The BDP and BUD solubilities are predicted using the Jouyban-Acree model [80], while the leucine solubility is from [37].

and 10% more mass of the actives, respectively, than a particle spray-dried in

pure ethanol.

BUD and BDP are usually spray-dried from ethanol or ethanol/water mixtures because of the low solubility of these actives in water. Spray drying of these drugs in the absence of any shell former will produce amorphous or semi-amorphous particles with a smooth and rather cohesive surface [37, 81, 82]. The cohesive nature of the resulting particles reduces their manufacturing and aerosolization efficiencies. To address this problem, different shell formers can be employed, *e.g.* to increase the rugosity of the particles. A shell former is an excipient that precipitates early during droplet evaporation and then forms a shell around the internal actives and excipients. These shells are often crystalline or rugose and can lower the cohesive forces between the particles. Leucine is considered in this study as a shell former candidate which has been used to make a shell around the actives in the center of the particles in order to increase production yield, dispersibility, and long-term storage stability of the final product [14, 31]. Unlike hydrophobic drugs, leucine has a higher solubility in water and very small solubility in alcohols, as shown in Figure 2.9. Hence the required fraction of the shell former should also be taken into consideration during the design stage of the formulation and the co-solvent system. This is specifically more important for leucine because it may produce different solid phases at different solid fractions [31]. A completely crystalline leucine shell is preferred, as small amounts of amorphous leucine in the presence of crystalline leucine may affect the long-term stability of the product.

2.4.3 Particle Formation in Co-solvent Systems

The internal profiles of the dried particles play an important role in the resulting properties of the product. As previously noted, the behavior of solutes inside an evaporating droplet can be characterized by the Péclet number, which is constant in a single solvent droplet (considering the composition-dependent diffusion coefficient) but varies with time in a multi-solvent system. During the drying process of a multi-solvent system, the evaporation rate and the effective diffusion coefficients generally change with time, and thus the Péclet number varies accordingly, as seen from Equation (2.23). Hence, as opposed

to reaching the steady-state value characteristic of pure solvent cases, the surface enrichment evolves in a way that cannot be predicted by the steady-state model.

How much the change in evaporation rate, solvent composition and solute solubility will affect particle formation depends on the type of the excipient: As a first example, the internal solute diffusion of trehalose, a typical disaccharide glass former used as a stabilizer for biologics, in different compositions of water and ethanol at 80 °C was modelled and the predicted time dependence of the Péclet number and surface enrichment, E_s, are reported in Figure 2.10. The Péclet numbers of trehalose in pure water and pure ethanol reached constant values of 1.0 and 4.3, respectively. The initial change in evaporation rates and thus the Péclet number was due to the equilibration of the droplet temperature, as the initial droplet temperature was 20 °C in all of the simulated cases. The surface enrichment of the single solvent cases reached the steady-state values as predicted by the VFL model shown in Equation (2.24). The value predicted by the VFL model was the final surface enrichment, reached after a transient stage (discussed in more detail in [33]). Iso-compositional drying was observed for droplets with a composition of 0.23:0.77 w/w water/ethanol and, as expected, the system behaved like a single solvent, with a steady Péclet number and surface enrichment converging to a steady value. In the other cases, with 0.3:0.7 and 0.7:0.3 w/w water/ethanol, the Péclet number started at intermediate values and eventually reached that of pure water. This is expected as the mass fraction of water increased over time, a consequence of initial water mass fractions that were higher than the iso-compositional value. The Péclet number of the 0.3:0.7 w/w water/ethanol case and the droplet composition were relatively constant throughout most of the drying time, a consequence of an initial composition close to the iso-composition. The surface enrichment for this case increased and reached the stable value of 1.9 with the initially constant Péclet number of 4.0, but then fell abruptly as the ethanol content in the droplet was depleted and converged to the steady-state surface enrichment of pure water. The surface enrichment of the 0.7:0.3 w/w water/ethanol case reached a maximum at about 20% of the droplet

lifetime and then gradually decreased to reach the steady value of pure water. Precipitation was not considered in these calculations; in reality, solid particles might be formed well in advance of the predicted final drying times depending on the initial amount of dissolved solids. This is especially true for shell formers and crystallizing solutes which might crystallize or precipitate on the surface, with a liquid phase remaining near the center of the particle. Indeed, the process could be designed to create an iso-compositional-like state using solvent compositions close to the actual iso-composition with precipitation occurring before the abrupt change in composition as seen in the 0.3:0.7 w/w water/ethanol case in Figure 2.10. Such a process would take advantage of drying at constant evaporation rates.

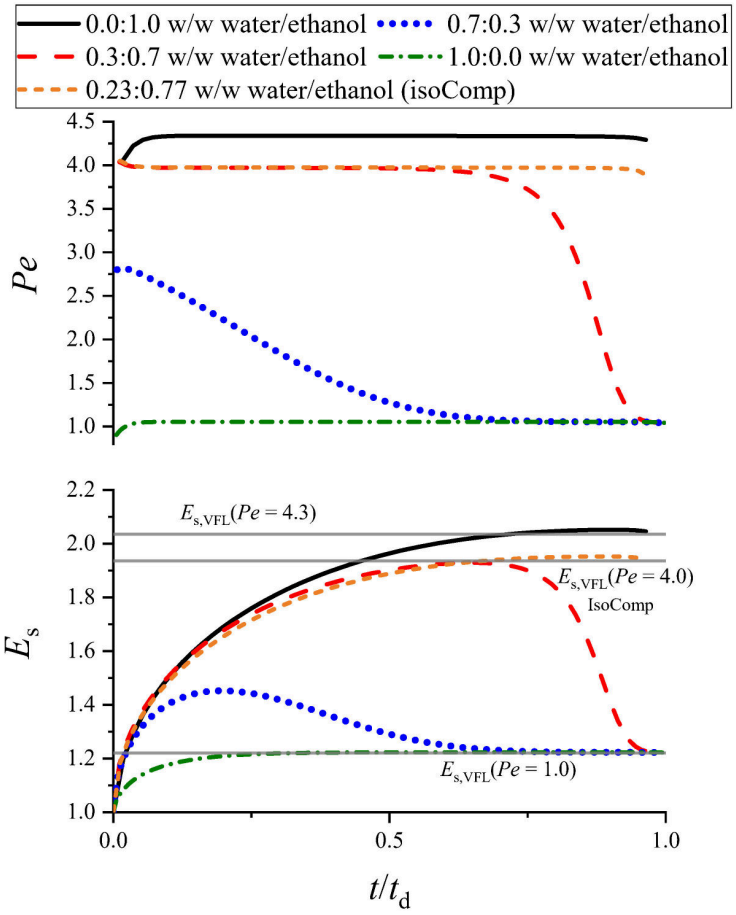

Figure 2.10: Histories of Péclet number and surface enrichment of trehalose at different compositions of water and ethanol drying at a gas temperature of 80 °C.

In the specific example of trehalose, the solute enrichment at the particle surface in ethanol was only double that of water; hence diffusion alone is unlikely to cause severe morphological differences. It has been shown previously that spray-dried particles from different co-solvent compositions can produce particles of significantly different aerosol performance and morphologies [37, 83, 84]. In all of these previous studies, the solid component that contributed to the change in morphology showed different crystallization behavior at different solvent compositions. For an excipient that rarely crystallizes during spray drying and has relatively similar Péclet numbers in the solvents of interest, such as trehalose, the change of solvent and solvent compositions does not strongly alter the general particle morphology. This can be seen from the Field Emission Scanning Electron Microscopy (FESEM) images shown in Figure 2.11. These trehalose particles were collected using the monodisperse droplet chain instrument for pure water and 0.30:0.70 w/w water/ethanol at 80 °C drying temperature. The initial feed concentration was 100 mg/mL in pure water and 10 mg/mL in the co-solvent case, due to solubility limitation. The internal structure of a single trehalose particle from the co-solvent case, cut by a Focused Ion Beam (FIB) under a Helium Ion Microscope (HIM), is also observed in the inset figure, which confirms a solid structure throughout the radial direction, similar to that of spray-dried trehalose in pure water [32]. Based on these observations it can be concluded that the general particle morphology of trehalose, which usually forms an amorphous solid during spray drying, is similar between these two cases. Hence, previous experience with aqueous systems can be employed for particle design of trehalose-containing formulations in ethanol/water solvent systems.

On the other hand, if there is an excipient in the formulation that can either crystallize during spray drying (with possibly different crystallization kinetics in different solvents), or has significantly different Péclet numbers in different solvents, or shows noticeably different surface activity behavior in different solvents, then the particle morphology is expected to vary with any change in composition of the co-solvent system. To illustrate this theory, leucine particles were generated in the monodisperse droplet chain setup at

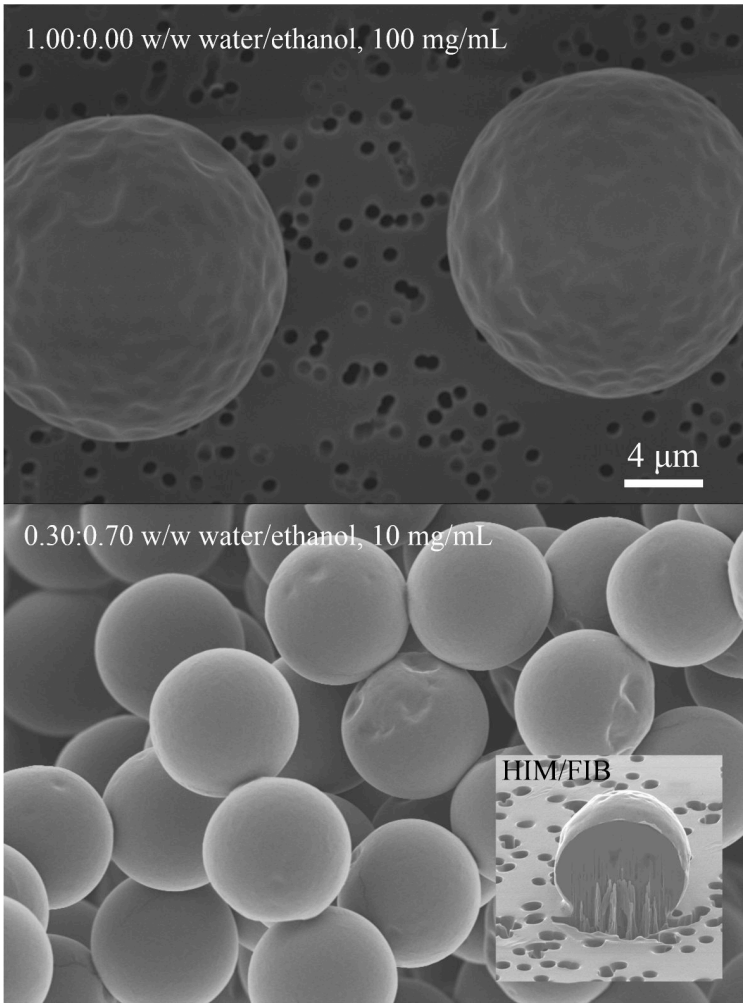

Figure 2.11: Trehalose particles collected from the monodisperse droplet chain instrument all at 80 °C. Top figure: 100 mg/mL in pure water, Bottom figure: 10 mg/mL in a mixture of water and ethanol and a sample HIM/FIB cut particle in the inset figure. The scale bar applies to all three figures.

20 °C with an initial concentration of 0.5 mg/mL in different initial water and ethanol compositions of 1.00:0.00, 0.75:0.25, 0.50:0.50 and 0.25:0.75 w/w water/ethanol, noting that the last case is close to the iso-compositional point of the co-solvent system. The FESEM micrographs of the collected particles are shown in Figure 2.12. Significant changes in morphology are observed with increasing initial ethanol content. First, the volume equivalent diameter of the particles increased with increasing ethanol content. The lower solubility of leucine and the higher Péclet number in ethanol compared to water initiates shell formation at an earlier point in the evaporation process and at a larger

diameter. Second, the general surface properties of the particles looked similar for the first three cases, with an outer shell and a single dimple, but were substantially different in the case with the highest amount of ethanol content with particles exhibiting a porous structure throughout. A higher resolution micrograph of one of the particles from the 0.25:0.75 w/w water/ethanol case was obtained using Helium Ion Microscopy (HIM). The particle was cut using a Focused Ion beam (FIB) to verify its porous internal structure. The results are shown in Figure 2.13.

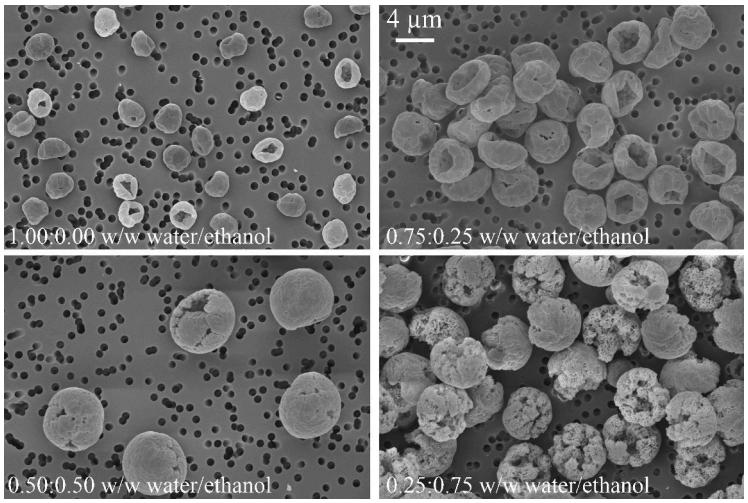

Figure 2.12: Monodisperse leucine particles collected from the droplet chain instrument dried at 20 °C from a solution of 0.5 mg/mL of different water and ethanol compositions.

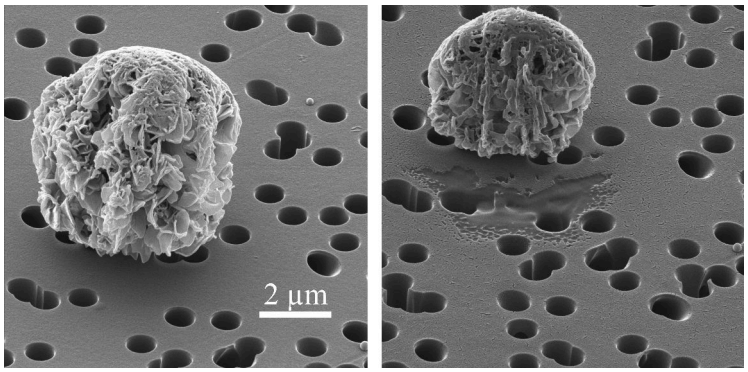

Figure 2.13: HIM images of a leucine particle dried at 20 °C from a solution of 0.5 mg/mL with 0.25:0.75 w/w water/ethanol initial co-solvent ratios. Left panel: uncut particle, Right panel: cut particle.

In order to understand and explain these changes in morphology, the nu-

merical model was used to predict the evaporation histories using the same experimental conditions and for initial leucine concentrations of 0.5 and 1.5 mg/mL. As leucine can crystallize during spray drying [31], the available time for crystallization after reaching saturation, $t_{\text{final}} - t_{\text{sat}}$, is an important parameter in determining the precipitation dynamics [32, 33], in which t_{final} is the total evaporation time of the droplet and t_{sat} is the time at which the solute reaches saturation. The dimensionless values of the available time for crystallization after reaching saturation $\tau_{\text{c}} = 1 - t_{\text{sat}}/t_{\text{final}}$ are shown in Figure 2.14a. τ_{c} is seen to gradually increase with increasing initial ethanol content for both concentrations, with a sharp increase at about 65% and 55% ethanol fractions for the 0.5 mg/mL and 1.5 mg/mL cases, respectively. This increase in τ_{c} is a consequence of the dependence of t_{sat} on the solubility, which is smaller for leucine in ethanol than in water. Also, τ_{c} is longer for the 1.5 mg/mL case since a higher solid concentration means an earlier saturation and a longer time available for crystallization to occur. The general increasing trend in τ_{c} is responsible for the larger particle diameters with increasing ethanol content observed from the experiments, since earlier crystallization means precipitation in a larger droplet. The iso-compositional point of the co-solvent system is close to 77% by mass of ethanol, and leucine solubility is much lower in ethanol than in water, as seen in Figure 2.9. Hence, the abrupt increase of τ_{c} is due to the occurrence of saturation in a pure water droplet before the abrupt change, as opposed to saturation in a water and ethanol mixture after this point. This can be seen from the mass fraction of ethanol left in the droplet at the time of saturation, $y_{\text{ethanol,sat}}$, versus drying time, as shown in Figure 2.14b. It is seen that at lower initial ethanol contents, leucine reaches saturation in pure water as these conditions are well below the iso-compositional point, and the droplet loses its ethanol fraction quickly as discussed earlier. At initial ethanol fractions of about 60% and 50% for the 0.5 mg/mL and 1.5 mg/mL cases, respectively, $y_{\text{ethanol,sat}}$ starts to rise, pointing to possible change in the crystallization kinetics as also indicated by the sharp increase in the τ_{c} plot. Some sample particles of the respective cases are also shown in Figure 2.14b to compare the change in the morphology of the leucine particles to $y_{\text{ethanol,sat}}$. It

is seen that when leucine reaches saturation while a small fraction of ethanol is present, the overall morphology of the particles is similar, but saturation during the presence of significant amounts of ethanol causes clear morphological differences. This variance can explain previously published observations that increasing the initial ethanol content above a certain limit increased the dispersibility and process yield of spray-dried budesonide particles with leucine as a shell former [37].

2.5 Conclusion

Spray drying of inhalable pharmaceuticals from co-solvent systems is more complex than it is for pure solvents because of temporal and droplet-size dependent variations in the evaporation rate, solubility, and crystallization kinetics. In such systems, the morphology of the particles – and consequently the performance of the dosage form – is sensitive to co-solvent ratio and other formulation and process parameters. This additional complexity heightens the need for numerical modeling during product development, *e.g.* when choosing initial processing conditions or during scale-up. Here, both the Maxwell and the Stefan-Fuchs models were used to study the evaporation kinetics of multi-solvent droplets in conjunction with appropriate methods of solving internal diffusion equations for particle formation applications. The Stefan-Fuchs model is most accurate at higher temperatures but is more complex and requires knowledge of more transport properties, while the Maxwell model can accurately be used at low temperatures with minimal complexity.

Exploring a variety of water/ethanol systems with different actives and excipients (trehalose, leucine), we find that co-solvent droplets can exhibit azeotropic-like behavior during evaporation at specific compositions, which we refer to as iso-compositional. We also find that the iso-compositional point in a water ethanol co-solvent system is a weak function of the drying temperature at drying conditions typical for spray drying. For a water/ethanol droplet, the evaporation rate at the iso-compositional point can be obtained from the molar weighted average of the evaporation rates of the pure components at

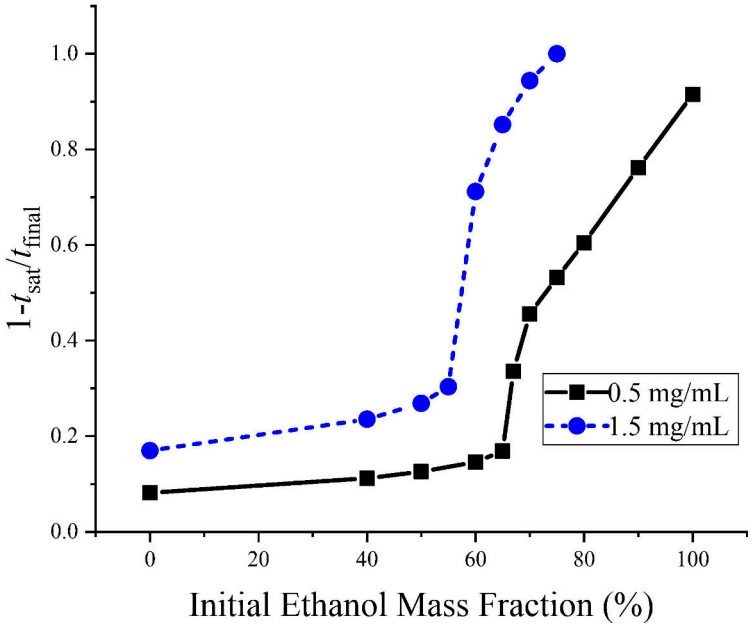

(a)

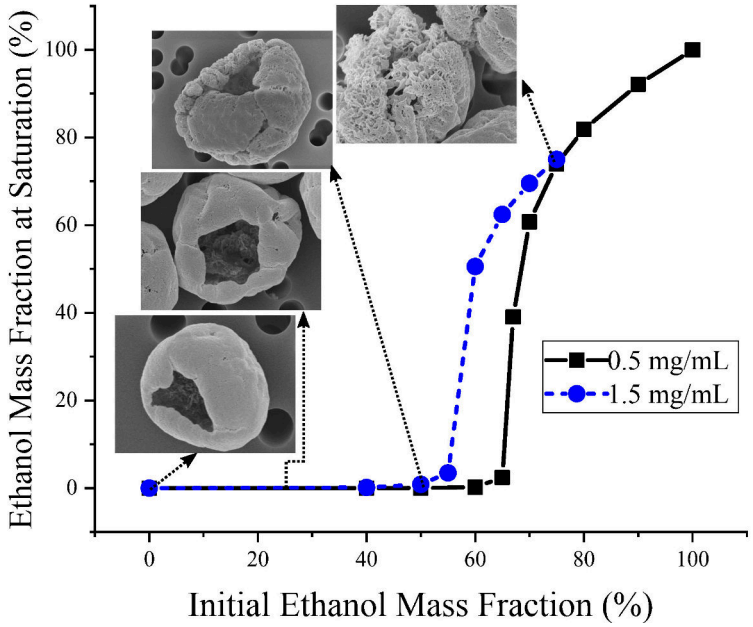

(b)

Figure 2.14: Numerical results for different concentrations of leucine drying at 20 °C in a range of initial water and ethanol compositions. (a) Dimensionless available time for crystallization, τ_c, (b) amount of ethanol left at saturation, $y_{ethanol,sat}$ accompanied by samples of collected leucine particles with initial concentration of 0.5 mg/mL.

any specified drying temperature. At the iso-compositional point the particle formation resembles that of a pure solvent case, and simple analytical particle formation models such as the VFL model can be used. The effect of relative humidity on the existence or composition of the iso-compositional state has not been analyzed and will be considered in later studies as even small amounts of ambient humidity can alter the vapor-liquid-equilibrium of the system.

Finally, we find that for non-crystallizing excipients for which particle formation is mostly diffusion controlled and the Péclet number is relatively similar in different co-solvent systems (*e.g.* trehalose), the morphologies of the dried particles are likely similar to those formed using water alone. This similarity allows experience from aqueous systems to be transferred to co-solvent systems for these excipients. In contrast, the presence of crystallizing components with large solubility differences in different co-solvent compositions (*e.g.* leucine) will likely exhibit noticeably different particle morphologies. A detailed knowledge of crystallization kinetics and solubility data is then required for such systems in order to explain and understand the source of these differences. This methodology can then be applied to practical systems of interest containing multiple active pharmaceutical ingredients and excipients.

Chapter 3

On the Particle Formation of Leucine in Spray Drying of Inhalable Microparticles

The particle formation of L-leucine, a dispersibility-enhancing amino acid used in the spray drying of inhalable pharmaceutical aerosols, was extensively studied using three experimental methods, and the results were interpreted with the aid of theory. A comparative-kinetics electrodynamic balance was used to study the shell formation behavior in single evaporating microdroplets containing leucine and trehalose. Different concentration thresholds of solidification and shell formation were determined for trehalose and leucine, which were then used in the particle formation model to predict the properties of spray-dried particles. Furthermore, a droplet chain instrument was used to study the particle morphologies and particle densities that were not accessible in the single particle experiments. Lab-scale spray drying was also used to produce powders typical for actual pharmaceutical applications. Raman spectroscopy confirmed that a glass former, such as trehalose, can inhibit the crystallization of leucine. The surface compositions of these spray-dried powders were analyzed via time-of-flight secondary ion mass spectrometry. The leucine surface coverage in a polydisperse powder was determined to be a function of the particle size or the initial droplet diameter of each respective particle. This observation confirms the important role of leucine crystallization kinetics in its shell-forming capabilities. A critical supersaturation ratio of 3.5 was also calculated for leucine,

at which it is assumed to instantaneously nucleate out of solution. This ratio was used as the threshold for the initiation of crystallization. Crystallinity predictions for the leucine-trehalose particles based on this supersaturation ratio were in good agreement with the solid-state characterizations obtained by Raman spectroscopy. This study improves the fundamental understanding of the particle formation process of leucine-containing formulations, which can apply to other crystallizing systems and potentially facilitate the rational design of such formulations with reduced experimental effort.

3.1 Introduction

Spray drying is a scalable industrial process that evaporates an atomized spray of a solution, a suspension or an emulsion into a solid powder with a well-controlled size distribution. In the pharmaceutical industry, spray drying has been used extensively in manufacturing solid dosage forms intended for pulmonary delivery. An aerosol needs to have specific aerodynamic properties for successful delivery to the intended areas of the lungs. Larger particles tend to deposit in the delivery device or the mouth-throat region due to inertial impaction, while very small particles might be exhaled [1]. For efficient delivery to the lungs, particles need to have aerodynamic diameters between approximately 1 and 5 µm [10]. Therefore, particle deaggregation is an important stage in the passive or active delivery of dry powder to the lungs, because an agglomerate behaves aerodynamically much like larger particles and might not reach the targeted pulmonary site [85, 86]. To assist with the aerosolization of the particles, dispersibility-enhancing agents have been used in spray drying of inhalable pharmaceutical aerosols. These materials operate in part by decreasing the surface energy and increasing the surface rugosity and roughness of the particles and hence decreasing inter-particle cohesion. It has been shown that increasing particle roughness reduces the cohesive forces between particles due to reduction in their effective contact area [87, 88]; while a reduction in surface energy directly reduces the cohesive forces [29].

L-leucine, an essential amino acid, has been widely used and studied as a

dispersibility enhancer of spray-dried inhalable microparticles [30, 37, 89, 90]. Leucine is a moderately surface-active material, compared to the stronger dispersibility enhancer trileucine [29, 88, 91], and has relatively low aqueous solubility, 22 mg/mL at room temperature [30]. These characteristics result in rugose spray-dried particles with low surface energies, which contribute to lower interparticle cohesion and thereby good aerosol performance [28]. Besides the dispersibility enhancement, it has been shown that a crystalline leucine barrier can also reduce moisture uptake and enhance aerosol performance in humid conditions [30, 92]. These desirable effects are direct consequences of the surface morphology and surface composition of the particles containing leucine [30, 89], which can to some extent be predicted from surface rheology properties [93] and particle formation models [14]. Based on these observations, the utilization of leucine as an excipient in spray drying inhalable particles is beneficial for different respirable dosage forms, such as colloidal suspensions in pressurized metered-dose inhalers [94] and in dry powder inhalers [89].

The fundamental understanding of the particle formation of leucine-containing formulations facilitates the rational design of such powders with minimal experimental effort. Available particle formation models can approximate the relative radial distribution of each component in an evaporating droplet and predict the general morphology of the resulting spray-dried particles in single-solvent [32, 33] and multi-solvent formulations [95]. The approximation is relatively straightforward for non-surface-active materials and those which do not crystallize during spray drying, such as most polysaccharides and polymers. However, leucine can crystallize during spray drying [31], which complicates the prediction of the final particle morphology and the surface composition of multi-component systems. This is because, upon nucleation and crystal growth, modelling of the distribution of different components inside the droplet becomes difficult due to rapid changes in their diffusion coefficients and because nucleation and crystal growth kinetics are not captured in the available models.

To predict the onset of phase separation, precipitation or shell formation, particle formation models compare the maximum concentration of each com-

ponent inside the droplet, which is generally reached on the surface of an evaporating droplet, to some predetermined value [33]. For a crystalline material, the solubility value is often considered as this limit, after which crystallization can commence; while for an amorphous component, the concentration at which precipitation occurs is compared to the true density of the material. For multicomponent amorphous systems, the total concentration of the amorphous material can be compared to the true density of the amorphous mixture [96]. Nevertheless, the solidification does not happen exactly upon reaching these limits [14]. For each specific system, further experimental observations are required to explain the particle formation process. For example, for a crystallizing component, such as leucine, a critical supersaturation is required for nucleation, which is a function of different chemical properties of the participating molecules and the process parameters [97]. Even if a value for a critical supersaturation can be determined theoretically, the modeling of the ensuing phenomena such as the rate of nucleation, crystal growth, and the subsequent surface enrichment of these crystallites is complicated by the fact that they likely occur in highly supersaturated solutions due to the fast evaporation of microdroplets in spray dryers [60]. Hence, experimental investigation is essential to better understand the particle formation in such systems.

Different experimental techniques have been used to study the drying kinetics of droplets containing solidifying or crystallizing components. For example, the drying behavior of single droplets, usually in the millimeter range, suspended from thin filaments has been studied [98]. In this method, the droplet is placed in a controlled environment with specified temperature and relative humidity. The drying kinetics can be accurately measured via either an imaging technique or attachment of the thin filament to a microbalance. The intrusive presence of the filament has been reported to affect the heat and mass transfer between the environment and the droplet [98, 99]. In another class of techniques used in such studies, single droplets have been successfully levitated using acoustic forces [100, 101], drag forces induced by an air stream [102, 103], the Leidenfrost effect [104], and electrodynamic forces [105–107]. In these methods, the environment conditions can be controlled easily, and the

instantaneous size of the droplets can be measured accurately, as the single droplets are usually held in place in a stable condition. The main disadvantage of these methods is that the dried particle cannot be collected for any subsequent analysis. A chain of falling monodisperse droplets has also been used to mimic the actual spray drying conditions to some extent [32, 59, 60, 87, 95]. In this method, usually called "the monodisperse droplet chain technique", the final dried particles were collected to study their morphology using electron microscopy. However, the small quantity of collected particles was not enough to allow other measurements such as Raman spectroscopy, which requires milligrams of powder. Also, the inherent instability of the droplet chain can make accurate measurement of the droplet size difficult, particularly in micrometer-size ranges. Although these experimental tools are promising for the study of the drying kinetics of droplets and provide insights into the particle formation processes, none of them represents actual spray drying conditions such as polydispersity of the powder and the temperature and relative humidity variations in the spray plume. Also, previous methodologies do not provide enough powder for a broad range of characterization techniques. Consequently and not surprisingly, actual spray drying on laboratory-scale dryers is still a popular method used in studying the particle formation of inhalable pharmaceutical aerosols [89, 92, 108]. The downside of lab-scale spray drying is that the drying kinetics and the exact initial droplet size distributions cannot be measured directly, and the drying conditions for the droplets are much less controlled.

In this study a theoretical model was compared to results from three experimental techniques: a single-particle electrodynamic balance, a droplet chain instrument, and a lab-scale spray dryer, in order to overcome their individual limitations. The particle formation of leucine was studied in combination with a disaccharide, trehalose. Trehalose was chosen as a model excipient for a glass stabilizer of biologics and other active pharmaceutical ingredients [28, 31, 96].

3.2 Materials and Methods

3.2.1 Materials

Different solutions of L-leucine (Cat. No. BP385-100, Fisher Scientific, Ottawa, ON, Canada) with D-(+)-trehalose dihydrate (Cat. No. BP2687-1, Fisher Scientific, Ottawa, ON, Canada) were prepared using HPLC-grade water (Cat. No. W5-4, Fisher Scientific, Ottawa, ON, Canada). The total excipient concentrations were varied in the range of 5 to 50 mg/mL with different mass fractions of trehalose and leucine.

3.2.2 Experimental Investigation of Particle Formation

Three different experimental techniques were used for this study. A single-particle analysis was performed using a Comparative-Kinetics Electrodynamic Balance (CK-EDB); in which single aerosol droplets were levitated in a controlled environment to measure their size and to infer their general morphology using scattered light [105, 109]. Using this method, the exact time and diameter at solidification can be determined accurately, enabling the estimation of the critical point for shell formation for each formulation. To study the morphology of the resulting microparticles using electron microscopy and to find the particle densities, a monodisperse droplet chain instrument was used to collect dried particles. The initial droplet diameters in both of these instruments (EDB: ∼50 µm, droplet chain: ∼40 µm) were larger than the typical sizes encountered in actual pharmaceutical spray dryers of about 10 µm. To generalize the results to practical applications and to produce enough powder for different characterization methods, a laboratory-scale spray dryer was used to produce bulk powders in the respirable range (1-5 µm aerodynamic diameter).

Comparative-Kinetics Electrodynamic Balance (CK-EDB)

The drying and solidification of single aerosol droplets in the form of aqueous solutions of the excipients were studied using a CK-EDB [58]. A single droplet (∼50 µm diameter) was generated using a droplet-on-demand dispenser (MJ-

ABP-01, MicroFab Technologies, Plano, Texas, USA) and charged by ion imbalance using DC voltage applied to an induction electrode positioned close to the tip of the dispenser. The droplet was then trapped inside a temperature- and RH-controlled environment at the center of the electrodynamic field, generated by applying an AC potential difference to two sets of concentric cylindrical electrodes mounted vertically opposite one another. An additional DC voltage was applied to the lower electrodes to counteract the gravitational force on the droplet. This electrodynamic field was dynamically manipulated to account for the changes in droplet mass. Upon confinement of the droplet in the trap, a 532 nm CW laser illuminated the particle. The interference between the reflected and refracted light produced an elastically scattered pattern also known as the phase function. The phase function was captured every ∼10 ms using a CCD sensor at a forward-scattering angle of 45° over an angular range of about 24°. The collected phase functions were then compared to Mie theory calculations to determine the size of the droplet at each time-point with an accuracy of ±100 nm [105]. The approximate morphology of the droplet during drying was also determined using a novel method based on the irregularities observed in the phase function [109]. The different morphologies detected are homogeneous and spherical, spherical with inclusions, core-shell with high radial concentration gradients, and non-spherical or inhomogeneous. The instance of shell formation or solidification was determined for each case using these measured qualitative morphology data as well as deviations from constant-rate evaporation. Further details and technical information pertaining to this instrument can be found in previous publications [40, 105, 109].

The formulations studied using the EDB instrument are presented in Table 3.1. For each case, two to five droplets were studied at a chamber temperature of 20 °C and relative humidity of ∼0% or ∼35%. This temperature was chosen based on the instrument limitations and also to allow accurate determination of the particle solidification behavior at higher temporal resolutions. The higher relative humidity was used to increase the relative temporal resolution of the EDB measurements in order to measure the onset of shell formation more accurately. The high total feed concentrations were chosen such

Table 3.1: The composition of the samples studied using the electrodynamic balance, accompanied by their feed concentrations, measured average initial droplet diameters and the relative humidities studied for each case. The drying temperature was set to 20 °C for all cases. The uncertainties of the initial droplet diameters are the standard deviation of multiple droplets studied for each case.

Sample Name	**Total Solids Content (mg/mL)**	**Trehalose Mass Fraction (%)**	**Leucine Mass Fraction (%)**	**RH (%)**	**d_0 (µm)**
EDB5L100	5	0	100	0,35	53.0±1.6
EDB10L100	10	0	100	0,35	53.4±0.2
EDB20L100	20	0	100	0,34	53.0±0.2
EDB10T20L80	10	20	80	37	55.8±0.4
EDB10T50L50	10	50	50	37	53.4±0.1
EDB10T70L30	10	70	30	39	50.1±0.2
EDB10T80L20	10	80	20	34	52.8±0.0
EDB10T90L10	10	90	10	34	53.5±0.0
EDB10T100	10	100	0	38	53.4±0.2
EDB5T100	5	100	0	35	53.6±0.2

that the shell formation would happen at large enough diameters to be accurately measured in the balance. The leucine concentrations were also chosen in such a way to cover a range of low saturation to high saturation.

Monodisperse Droplet Chain Instrument

A custom-made droplet chain instrument was used to produce and collect monodisperse particles for electron microscopy purposes [59, 60, 95]. In this setup, a droplet-on-demand piezoceramic dispenser with an orifice diameter of 40 µm (MJ-AL-HT-40-8MX, MicroFab Technologies, Plano, Texas, USA) horizontally injected droplets into a vertical glass tube with a frequency of 60 Hz. Dry air, at room temperature, passed through the flow tube from above with a flow rate of approximately 10-15 L/min. Dried particles were then collected at the bottom of the flow tube on a SEM sample stub with a hole drilled through it, onto which a membrane filter with a pore size of 0.8 µm (Isopore Polycarbonate, Millipore, Darmstadt, Germany) was attached with the help of a punched double-sided carbon tape. The other end of the SEM stub was connected to a vacuum line with a monitored flow rate of about 10-15 L/min.

Table 3.2: The composition of the samples studied using the droplet chain instrument, accompanied by their feed concentrations and measured average initial droplet diameters. The drying temperature was set to 20 °C for all cases. The uncertainties of the initial droplet diameters are the standard deviation of hundreds of droplets per case.

Sample Name	**Total Solids Content (mg/mL)**	**Trehalose Mass Fraction (%)**	**Leucine Mass Fraction (%)**	d_0 **(µm)**
MDC5L100	5	0	100	39.8±0.1
MDC10L100	10	0	100	36.2±0.1
MDC20L100	20	0	100	35.8±0.4
MDC10T50L50	10	50	50	37.2±0.2
MDC10T80L20	10	80	20	37.1±0.3
MDC10T90L10	10	90	10	37.7±0.3
MDC10T100	10	100	0	42.4±0.1

The flow rate of the dry air passing through the flow tube was slightly larger than the vacuum-line flow rate in order to maximize the collection efficiency of the particles and reduce contamination from the surrounding environment. A lens and digital camera system was used to measure the initial diameters of the generated droplets.

The formulations studied with this instrument are shown in Table 3.2. The formulations were chosen to be similar to some of the formulations studied using the CK-EDB instrument. The average initial droplet diameters were obtained using the image processing tool of MATLAB [110] from two sets of images, one hundred per set, taken at the start and near the end of each experimental run to factor in any changes in droplet diameter throughout the duration of the particle collection, which was about 3 hours.

Lab-scale Spray Drying

In order to produce enough powder for further characterization and also to assess the applicability of the conclusions obtained from the previous experiments in a manufacturing environment, a lab-scale spray dryer (B-191, Büchi Labortechnik AG, Flawil, Switzerland) was used in conjunction with a customized twin-fluid atomizer [96]. A thermodynamic process model developed for this specific spray dryer was used to select process conditions so as to have

Table 3.3: The compositions, feed concentrations and approximate median initial droplet diameters of the spray-dried formulations. Inlet temperature was 75 °C for all cases.

Sample Name	**Total Solids Content (mg/mL)**	**Trehalose Mass Fraction (%)**	**Leucine Mass Fraction (%)**	$d_{0,50}$ **(µm)**
SD50T60L40	50	60	40	∼8
SD50T80L20	50	80	20	∼8
SD50T90L10	50	90	10	∼8
SD50T100	50	100	0	∼8

appropriate outlet temperature and humidity, as explained elsewhere [15]. For all of the spray-dried formulations, the inlet temperature was set to 75 °C, the liquid feed flow rate was set to 2.5 mL/min, drying gas flow rate was 540 L/min, and atomizer air-to-liquid ratio was 10. Based on the process model, these parameters resulted in an outlet temperature of about 48 °C and predicted outlet relative humidity of about 7%. The measured outlet temperatures were between 48.6 and 49.2 °C. Based on the chosen air-to-liquid ratio and available characterization curve of the atomizer [111], the initial mass median diameter of the atomized droplets was approximately 8 µm. The collected powders were stored in a dry box (RH ∼0%) at room temperature (20 °C).

The initial compositions of the spray-dried formulation are shown in Table 3.3. The formulations were chosen so that most of the resulting particles would be in the respirable regime. The leucine contents were also chosen to cover the probable transition from partially amorphous to fully crystalline state.

3.2.3 Characterization Techniques

Scanning Electron Microscopy

The micrographs presented in this article were obtained using a field emission scanning electron microscope (Sigma FESEM, Zeiss, Jena, Germany) with an accelerating voltage of 5 kV and working distances ranging from 5 to 10 mm.

The sizes of the particles obtained from the monodisperse droplet chain instrument were measured from the SEM images at 1000x using ImageJ soft-

ware [112]. The projected area of about 40 particles per sample was measured manually to find the average projected area diameter of the particles. The projected area diameter represents the volume equivalent diameter of the particles only if the particles are completely spherical. As will be seen later, for some of the studied cases the particles were not completely spherical. Nevertheless, the projected area diameter was used as an estimate of the particle sizes for each sample.

Raman Spectroscopy

Spray-dried powders were measured with a custom-designed dispersive Raman spectrometer [113] to determine the solid phase of each component. Powder samples were first loaded into a 0.2 µL cavity of an aluminum sample holder and kept under dry condition with less than 3% relative humidity during spectra acquisition. A 671 nm diode laser (Ventus 671, Laser Quantum, UK) with a maximum output power of 500 mW was used as the light source for Raman signal excitation. Raw trehalose and L-leucine were measured directly as received to obtain their respective crystalline Raman reference spectra. Spray-dried pure trehalose was measured to be amorphous and used as the reference spectrum [31]. Because an amorphous leucine powder reference could not be produced, the reference spectrum of amorphous leucine was approximated by measuring its saturated aqueous solution and then subtracting the spectrum of water. Characteristic peaks of the reference spectra for each component were used to determine the solid phase of each component. A full multivariate deconvolution process, which has been explained in detail elsewhere [113], was used to quantitatively determine the solid phase of each component in multi-component systems. Briefly, spectral contributions of each component were subtracted from the raw spectrum of the mixture until their respective characteristic peaks were eliminated and a close-to-flat residual spectrum was obtained. The spectral intensities of each component were then correlated to their corresponding mass fractions using a calibration factor obtained by measuring a spray-dried powder with known mass fraction of amorphous leucine and using trehalose as the internal reference.

Time-of-Flight Secondary Ion Mass Spectrometry (TOF-SIMS)

The surface composition of the spray-dried powders was measured with an average depth of 3-5 nm [114] using a TOF-SIMS instrument (TOF.SIMS^5, ION-TOF GmbH, Münster, Germany) with Bi_3^+ ion source operating at 30 keV energy. Measurements were done on a raster size of 200 µm × 200 µm with a frame size of 1024×1024 pixels and five pulses per pixel. These frames were then binned 2×2 for data processing, giving 512×512 pixels. The spectrum of each raw material was also measured as a reference spectrum. The composition of each pixel was obtained from fitting the spectrum at that pixel to a linear combination of reference spectra obtained by a non-negativity constrained alternating least squares method. Further details on the processing of the SIMS spectra can be found in another publication by the authors [115].

To represent the average surface compositions, for each sample, a single 512×512 pixel 8-bit RGB image was then obtained from the spectra matrices, with the red channel reserved for leucine, the blue channel reserved for trehalose and the green channel not used. Image analysis was performed using MATLAB to obtain the average surface composition of each material for the whole frame and the surface compositions of different size fractions of particles, *i.e.* small (less than 1 µm diameter), medium (between 1 and 3 µm diameter), and large (greater than 3 µm diameter). The color intensity (0-255 for 8-bit channels) of each pixel was read and used to find the surface compositions. If the total intensity of a pixel was less than 1, that pixel was not used in the statistical calculations further on, in order not to account for pixels that were not part of any particle. The average of all the acceptable pixels of each image was then used to find the average surface coverage of each component for the whole frame and for each of the size ranges. Grouping of particles based on their sizes was performed as follows. Around 30 particles per size-bin per sample were randomly selected from each frame and manually moved onto an empty black frame using imageJ software. These mostly black images were then used to find the surface composition of each size range. The molar-based surface compositions were in turn converted into mass fractions to compare

with the bulk fractions of the formulations studied.

3.2.4 Particle Formation Theory

A preliminary understanding of the different phenomena occurring during droplet evaporation and the eventual solids formation and crystallization, requires some knowledge of the basics of particle formation theory. Predictions based on such theory can help a formulator in early design stages. The most straightforward relationship used to predict the final particle sizes during spray drying is based on a simple mass balance as [14]

$$d_{\mathrm{p}} = \sqrt[3]{\frac{C_{0,\mathrm{t}}}{\rho_{\mathrm{p}}}} d_0, \tag{3.1}$$

in which, d_{p} is the volume equivalent particle diameter, $C_{0,\mathrm{t}}$ is the initial total solids concentration, ρ_{p} is the particle density and d_0 is the initial droplet diameter. The use of Equation (3.1) requires the particle density to be known in advance, which is typically not the case for rugose and hollow particles. Particle density is defined as the total mass of the dried particle divided by the particle volume including the internal and external voids. For solid and spherical particles, such as spray-dried trehalose, the particle density can be assumed to be equal to the material's true density, *e.g.* 1530 mg/mL for amorphous trehalose [32]. If the particle density is not known, a value of 1000 mg/mL can be considered as a rough approximation. Based on the inverse cube root relationship, the effect of particle density on the particle diameter is relatively small.

There is a linear correspondence between the particle and initial droplet diameters, which makes the particle diameter more sensitive to the atomized droplet size distribution. For polydisperse spray drying applications, the mass median diameter (MMD) of the atomized droplets is usually used as d_0 in Equation (3.1) to give the mass median diameter of the spray-dried powder.

The presence of dispersibility enhancers such as leucine and trileucine in the formulation results in the production of rugose and thin-shelled particles, for which, as will be seen later, particle densities of as low as 300 mg/mL can

be achieved. In these cases, a more advanced understanding of the internal distribution, precipitation, and phase separation behavior of each component is required for successful particle design.

In an evaporating solution droplet, the recession of the liquid/air interface causes surface enrichment by the solutes. This means that the concentration of the solutes on the surface will be higher than at the center of the droplet. This induced concentration gradient causes a radial diffusion flux of each species from the surface towards the center [32, 33]. The larger or less mobile the solute molecules are, the smaller their diffusional flux will be, which means a higher level of surface enrichment. For example, a polymer with a large molecular size causes early shell formation during drying [96]. The magnitude of surface enrichment during droplet evaporation can be calculated by solving the mass transfer equation inside the droplet [32, 33, 95]. The surface enrichment is defined mathematically as the instantaneous surface concentration of each solute normalized by the mean concentration of that solute inside the droplet. This normalized parameter has an asymptotic behavior and over time approaches a value called the steady-state surface enrichment, $E_{\mathrm{s},i}$. For small molecules, this steady-state value can be obtained from what is known as the VFL method [32]:

$$E_{\mathrm{s},i} = \frac{C_{\mathrm{s},i}}{C_{\mathrm{m},i}} \approx 1 + \frac{Pe_i}{5} + \frac{Pe_i^2}{100} - \frac{Pe_i^3}{4000} \qquad Pe_i = \frac{\kappa}{8D_i} < 20, \tag{3.2}$$

where $C_{\mathrm{s},i}$ and $C_{\mathrm{m},i}$ are the instantaneous surface and mean concentrations, respectively and Pe_i is the Péclet number of the ith component. Here, κ is the evaporation rate of the droplet (defined later) and D_i is the mass diffusion coefficient of the respective component. The Péclet number compares the timescales associated with surface recession and diffusion. A very large Péclet number ($Pe > 20$) means the solute does not have enough time to diffuse inwards due to the rapid recession of the droplet surface. This phenomenon results in a very high surface enrichment and large concentration gradients near the surface, but relatively constant concentrations elsewhere. At these high Péclet numbers, the steady state surface enrichment is only reached at the very end of the droplet evaporation time. At moderate Péclet numbers

($0.5 < Pe < 20$), the intensities of diffusion and surface recession are relatively equal, and there will be a smooth concentration profile with a maximum at the surface and a minimum at the droplet center. For low Péclet numbers ($Pe < 0.5$) the evaporation rate is much smaller than the diffusion of the solute such that the internal concentration will be approximately equal to the mean concentration at each time throughout the droplet. In this case, the steady state surface enrichment is approached quite early, and it can be assumed that the surface enrichment is equal to the steady state value obtained from Equation (3.2). The evaporation rate is defined as

$$\kappa = -\frac{\mathrm{d}d^2}{\mathrm{d}t}, \tag{3.3}$$

in which d is the instantaneous diameter of the droplet. The evaporation rate is constant for a large proportion of the droplet drying time for single-solvent formulations and can be obtained from the solution of the coupled heat and vapor mass transfer equations around a spherical droplet [95, 105]. Using a numerical model [95], the evaporation rates of water droplets at different drying temperatures and four different relative humidities were calculated and are shown in Figure 3.1. The evaporation rates at higher relative humidity values are presented as a reference for comparison, because in actual spray dryers the humidity can be high in the vicinity of the spray plume due to high spray rates and low temperatures due to evaporative cooling. It is worthwhile to note that at higher relative humidity values, droplets begin to boil at lower drying temperatures, at which the evaporating droplet temperature approaches 100 °C, represented by the gray dashed line and arrow in this figure, after which no increase in evaporation rate is possible.

Using a simple mass balance between the initial droplet state and any time during the drying period, the mean concentration of any solute in solution form can be obtained from [14]:

$$C_{\mathrm{m},i}(t) = C_{0,i}\left(1 - \frac{t}{t_\mathrm{d}}\right)^{-\frac{2}{3}}, \tag{3.4}$$

in which $C_{0,i}$ is the initial feed concentration of the solute and t_d is the droplet lifetime. Equation (3.4) can be obtained by assuming a constant evaporation

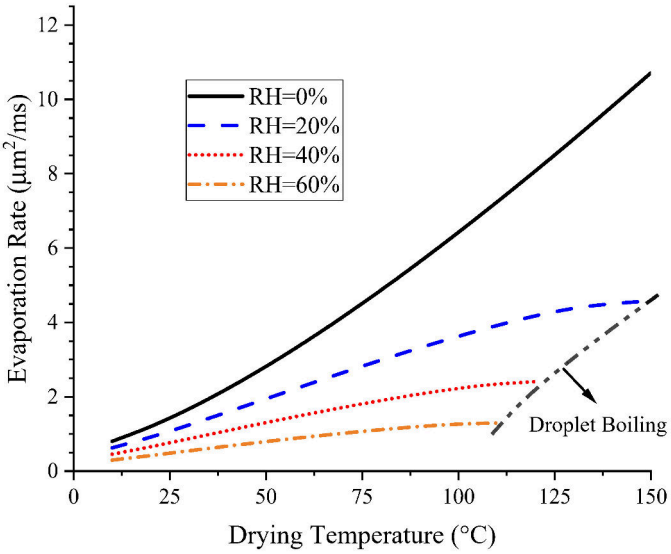

Figure 3.1: Water droplet evaporation rates, κ, at different drying temperatures and relative humidities.

rate and integrating Equation (3.3) to give $d^2(t) = d_0^2 - \kappa t$, and then using this result for the diameter in the mass balance equation. The droplet lifetime can be obtained similarly by setting the diameter equal to zero, which gives

$$t_{\mathrm{d}} = \frac{d_0^2}{\kappa}. \tag{3.5}$$

In a simple particle formation model, for a crystallizing component such as leucine, the time at which saturation is reached (*e.g.* $C_{\mathrm{s,leu}} = C_{\mathrm{sol,leu}} = 22$ mg/mL) is usually considered as a first instance at which nucleation can commence. By using Equation (3.4) and the definition of surface enrichment, it is possible to obtain the time needed by any component to reach saturation from

$$t_{\mathrm{sat},i} = t_{\mathrm{d}} \left[1 - (S_{0,i} E_{s,i})^{\frac{2}{3}} \right], \tag{3.6}$$

where $S_{0,i}$ is the initial concentration of the solute normalized by its solubility, *i.e.* the initial saturation ratio of the solute. Note that it is assumed that the surface enrichment is approximately equal to the steady state surface enrichment, $E_{\mathrm{s},i}$, during much of the droplet lifetime, which is true for small Péclet numbers associated with small molecules, such as trehalose and leucine. For

larger Péclet numbers, the relationships presented in [33] can be used to find the instantaneous surface enrichment.

Upon reaching supersaturation, some time is required for the solute molecules to crystallize before the remaining water content of the droplet is evaporated off and the molecules lose their mobility. Another important timescale that determines the crystallization behavior of a component is the available time for crystallization or the precipitation window, defined as

$$t_{\mathrm{p},i} = t_{\mathrm{d}} - t_{\mathrm{sat},i} = t_{\mathrm{d}} \left(S_{0,i} E_{\mathrm{s},i}\right)^{\frac{2}{3}} , \tag{3.7}$$

or in dimensionless form as

$$\tau_{\mathrm{p},i} = \frac{t_{\mathrm{p},i}}{t_{\mathrm{d}}} = \left(S_{0,i} E_{\mathrm{s},i}\right)^{\frac{2}{3}} . \tag{3.8}$$

In the remainder of this article, the Greek letter τ will denote the dimensionless time of the respective timescale normalized by the droplet drying time. The larger this value, the more crystallinity is expected for a crystallizing component [31]. The presence of another component such as a saccharide (*e.g.* trehalose) can also hinder the mobility of the crystallizing components due to the increase in viscosity of the solution at higher saccharide concentrations [116] or their earlier solidification. This explains the fact that leucine has a higher amorphous fraction in spray-dried powder with high fractions of trehalose [31].

For nucleation to start and stable nuclei to form and grow, a certain level of supersaturation is required to surpass the energy barrier of nucleation [117]. Therefore, a more relevant point during the evaporation history can be identified, namely the critical supersaturation ratio, $S_{\mathrm{n},i}$, at which the component can instantaneously nucleate. In a manner similar to the derivation of Equation (3.6), the time to reach this critical supersaturation, $t_{\mathrm{n},i}$, can be obtained as

$$t_{\mathrm{n},i} = t_{\mathrm{d}} \left[1 - \left(\frac{S_{0,i} E_{s,i}}{S_{\mathrm{n},i}}\right)^{\frac{2}{3}}\right] . \tag{3.9}$$

Upon reaching this level of supersaturation, nucleation can start on the surface of the droplet. The subsequent growth of the crystallites reduces their

mobility and causes their Péclet numbers to increase substantially, meaning that any crystallite that is collected by the receding surface of the droplet is practically trapped on the surface. Further surface accumulation of these crystallites and their simultaneous growth causes a solid shell to form on the surface of the droplet [60] at time t_c, defined as the time of shell formation. Upon reaching this time, the evaporation rate as defined by Equation (3.3) is reduced substantially, even though the particle continues to lose water and may shrink further. This process, as shown schematically in Figure 3.2, explains the observed hollow particle morphologies for a crystallizing material with low aqueous solubility such as leucine [14, 31]. For a component that crystallizes during drying, the time of shell formation, t_c, does not follow the behavior of the other timescales such as t_n, t_{sat} and t_d. This is because the rates of nucleation, crystal growth and surface accumulation cannot be correlated with the evaporation rate alone. For this reason, it is possible instead to find t_c from the EDB observations, defined in this article as the time at which deviation from d^2-law is observed in the evaporation history, rather than by using the mass balance equations similar to Equation (3.6).

He et al. successfully measured the critical supersaturation at which nucleation commences instantaneously in evaporating microdroplets via the extrapolation of nucleation times for a broad range of compounds and proposed a practical model to predict this critical supersaturation, S_n, based on classical nucleation theory and as a function of crystal and solution properties [97]. The appropriate properties for leucine in aqueous solutions were crystalline leucine density, ρ_{leu} = 1293 mg/mL [118] and its aqueous solubility, $C_{sol,leu}$ = 22 mg/ml at 25 °C [119]. The activity coefficient of water at leucine saturation was approximated to be equal to 1 [120]. Inserting these values in equations given by He et al. gave $S_{n,leu} = 3.5$. Hence, based on this simple model, leucine was expected to start nucleating instantaneously at a supersaturation of 3.5 in a water microdroplet.

For materials that are spray dried into an amorphous state, such as trehalose [31] and pullulan [96], solidification starts upon reaching a very high concentration, denoted as $C_{c,i}$ in this study. The time to reach this critical

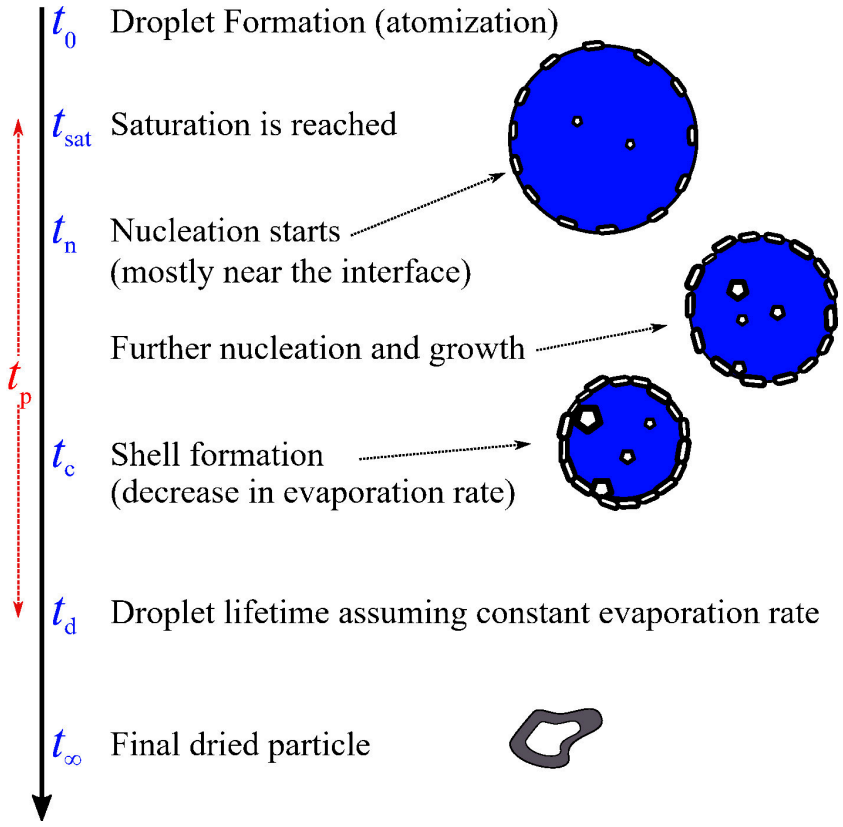

Figure 3.2: The proposed particle formation process and characteristic times for a crystallizing component with low solubility.

concentration can be obtained from

$$\tau_{c,i} = 1 - \left(\frac{C_{0,i} E_{s,i}}{C_{c,i}} \right)^{\frac{2}{3}} . \tag{3.10}$$

Note that based on the Stokes-Einstein equation, the diffusion coefficients of leucine and trehalose in water at 20 °C are 6.6×10^{-10} and 5.2×10^{-10} m^2/s, respectively. These give Péclet numbers of about 0.8 and 1.1 at a drying temperature of 75 °C and 0.2 and 0.3 at a drying temperature 20 °C, for leucine and trehalose, respectively. Hence, for the drying temperatures encountered in this study, the use of the steady state surface enrichment equations is reasonable. If that is not the case for a large excipient or API or at much higher evaporation rates, the methodology presented in [33] can be employed to approximate the evolution of surface enrichment with time.

The important time scales and diameters encountered in this study are summarized in Table 3.4.

Table 3.4: Important time scales and diameters relevant to the solidification and shell formation of the particles encountered in this study.

Parameter	Dimensionless Form	Description
t_{d}	-	The drying time of the droplet assuming constant evaporation rate (Equation (3.5)).
$t_{\mathrm{n,leu}}$	$\tau_{\mathrm{n,leu}} = t_{\mathrm{n,leu}}/t_{\mathrm{d}}$	The time for leucine to reach its critical supersaturation. Obtained from Equation (3.9) with $S_{\mathrm{n,leu}} = 3.5$.
t_{c}	$\tau_{\mathrm{c}} = t_{\mathrm{c}}/t_{\mathrm{d}}$	The time of shell formation or solidification obtained from the EDB measurements.
$t_{\mathrm{c,leu}}$	$\tau_{\mathrm{c,leu}} = t_{\mathrm{c,leu}}/t_{\mathrm{d}}$	The time of shell formation of leucine obtained from Equation (3.11), which was a non-linear fit based on the EDB measurements.
$t_{\mathrm{c,treh}}$	$\tau_{\mathrm{c,treh}} = t_{\mathrm{c,treh}}/t_{\mathrm{d}}$	The solidification time of trehalose obtained from Equation (3.10) with $C_{\mathrm{c,treh}} = 830$ mg/mL. This concentration was obtained from the EDB measurements.
d_0	-	The initial droplet diameter.
d_{c}	d_{c}/d_0	The diameter at which shell formation or solidification was detected in the EDB measurements.
d_{p}	d_{p}/d_0	The final projected area equivalent diameter of the monodisperse particles generated using the droplet chain instrument.

3.3 Results and Discussions

As mentioned in the previous sections, different combinations of trehalose and leucine were studied. The main object of the experimental procedure was to study the shell formation and crystallization kinetics of leucine-containing particles to support future mechanistic design attempts in spray drying microparticles containing different excipients and APIs intended for pulmonary aerosol delivery.

3.3.1 Comparative-Kinetics Electrodynamic Balance

The CK-EDB instrument allowed the accurate measurement of the time at which deviation from d^2-law is observed in the evaporation history, which we define here as the time to shell formation, t_{c}. A novel method was also employed to approximate the general morphology of the solution droplet based on the irregularities observed in the phase function of the scattered light [109].

Two to five droplets per formulation (Table 3.1) were studied at 20 °C and at dry (RH = 0%) and humid (RH ≈ 35%) conditions. Samples of droplet data per formulation are shown in Figure 3.3. The data points are color-coded based on the detected morphologies. The square of the droplet diameter is plotted as a function of time, yielding a straight line for constant-rate evaporation according to the d^2-law. However, the droplet diameters are only reliable for the completely spherical morphologies (color-coded dark blue). It can be seen that there is some noise in most cases during the initial or middle stages of the evaporation upon droplet generation, resulting in unexpected morphology results like a core-shell structure early in the evaporation process (color-coded red). These anomalies may have been be caused by instability of the droplet inside the chamber.

By reviewing the droplet data for pure leucine cases in Figure 3.3, *i.e.* the first row of panels, a region can be observed at which inclusions were detected, shown by the black points. At these instances, significant deviation from the d^2-law, *i.e.* from a constant evaporation rate, is also visible. Later on, the morphology was detected to be non-spherical or non-homogenous, denoted by the purple points. Increasing the initial concentration of leucine accelerated the occurrence of this critical point, meaning that the inclusions happened at a larger droplet diameter. It was also observed that increasing the initial leucine concentration likewise caused the elapsed time between the onset of inclusions and the first non-spherical point (purple points) to increase.

These observations agree with our previous explanation regarding leucine particle formation (Figure 3.2). A critical supersaturation is reached at the time $t_{\mathrm{n,leu}}$ at which nucleation commences. This point cannot be detected in the measurements because the droplet is still optically homogeneous with nuclei present that are too small to be detected by changes in the phase function. Then the crystallites grow and enrich the surface to a point at which the phase function of the scattered light is affected, and the evaporation rate is decreased. At this point the time for shell formation ($t_{\mathrm{c,leu}}$) is reached. The detected morphologies in Figure 3.3 follow the same sequence, showing optically homogeneous spheres during the constant rate evaporation phase,

inclusions and core-shell structures at the point of shell formation and then non-spherical, irregular morphology once the shell begins to deform or fold.

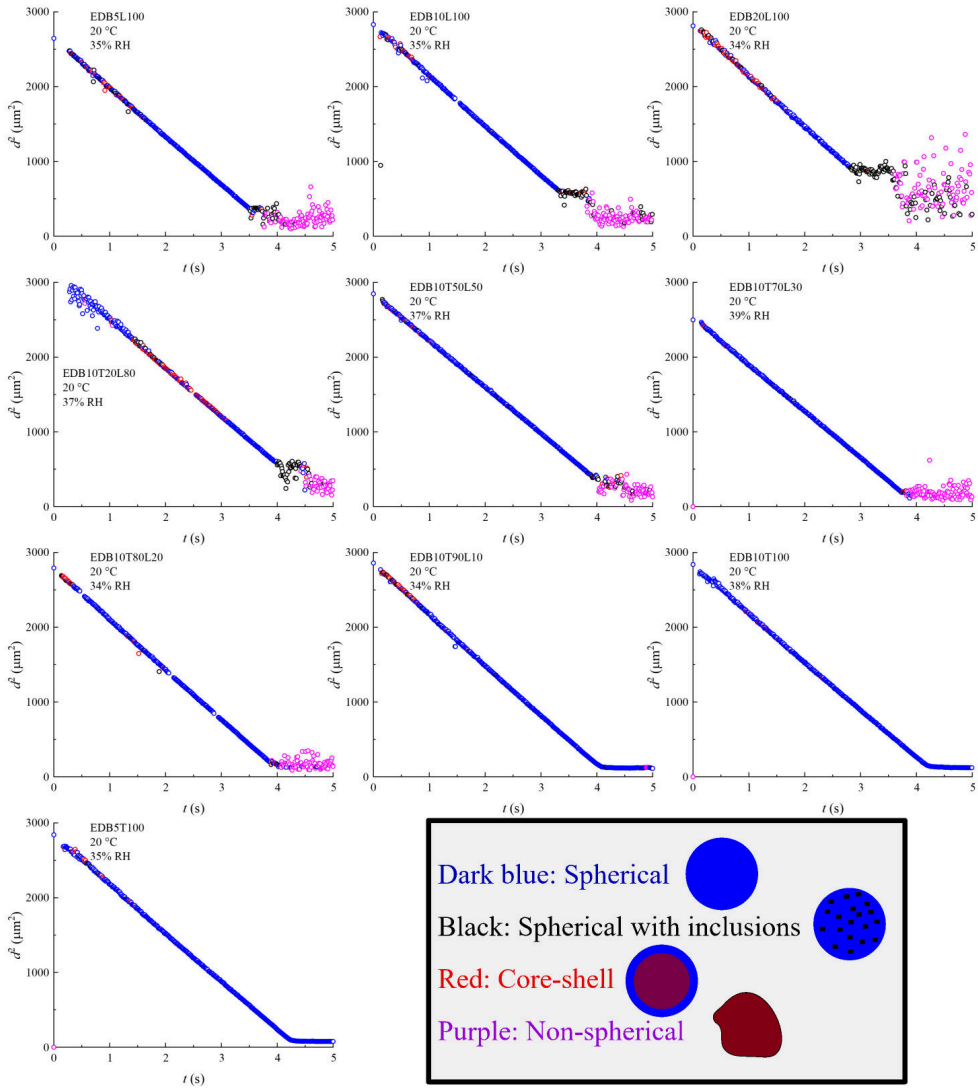

Figure 3.3: Sample droplet evaporation histories of the formulations studied using the CK-EDB instrument. The data are color-coded according to the detected morphologies. A label such as EDBαTβLγ means the formulation studied with the EDB instrument had a total feed concentration of α with trehalose and leucine mass fractions of β and γ, respectively.

In the cases of mixtures of leucine and trehalose, shown in the next five plots in Figure 3.3, similar behavior was observed. Increasing the leucine fraction at constant total solids content initiated shell formation at an earlier time, indicating the potential to obtain larger, less dense and more rugose particles.

By a qualitative comparison of plots for the samples EDB5L100 (5 mg/mL pure leucine) and EDB10T50L50 (10 mg/mL with 50% leucine), which had the same absolute initial leucine concentrations, relatively similar behavior was observed. The shell formation time was also similar. From this observation, we can conclude that at high leucine fractions, trehalose does not interfere with the crystallization of leucine. For the cases with leucine fractions less than 30%, a reversal in behavior was observed. No significant period of inclusions and crystal growth was observed before complete solidification. For the case of 10% leucine, the particles remained spherical even after the evaporation rate was reduced. These observations are in agreement with previous studies which demonstrated that high fractions of trehalose can hinder the crystallization of leucine to the point at which leucine is mostly amorphous, possibly due to rapid increase of droplet viscosity [31].

For the last two formulations of neat trehalose, a very sharp drop in the evaporation rate was observed after which a spherical particle was detected. This was expected, as neat spray-dried trehalose particles are spherical (see Figure 3.7). Using the measured diameter at the points at which the evaporation rates decrease, a trehalose bulk concentration at which solidification commenced was obtained. The measured concentration was practically the same for the two cases studied, each with a number of replicates. We call this concentration the solidification concentration for trehalose, $C_{\mathrm{c,treh}} = 830 \pm 15$ mg/mL; the error represents one standard deviation. It was shown previously that the particle density of spray-dried trehalose particles was approximately equal to the density of amorphous trehalose, which is 1530 mg/mL [32]. The lower measured critical concentration for trehalose points to the fact that the particles keep shrinking at a much smaller rate, while losing their water content, until the true density is reached.

For all of the experiments performed (2-5 droplets per formulation), the shell formation time, t_{c}, and corresponding diameter, d_{c}, were measured. The normalized values d_{c}/d_0 and $\tau_{\mathrm{c}} = t_{\mathrm{c}}/t_{\mathrm{d}}$ are plotted as a function of initial leucine concentration in Figures 3.4 and 3.5, respectively. In these figures, the error bars represent one standard deviation. As seen from these plots and as

pointed out earlier, the time of shell formation was decreased, and the critical diameter increased, by increasing the initial leucine concentration. These phenomena can be explained by the fact that leucine reaches critical supersaturation earlier in the evaporation process if the initial leucine concentration is higher (see Equation (3.9)). This trend was similar between the pure leucine formulations and the formulations containing trehalose. Again, this fact points to our previous observation that trehalose has no discernible effect on the crystallization and shell formation of leucine at high leucine fractions. The mean concentrations of leucine at the point of shell formation, $C_{\mathrm{c,leu}}$, were also calculated from a mass balance equation and are shown in Figure 3.6. The level of leucine saturation is also shown on the right axis. The leucine saturation ratio at the point of shell formation was 5 ± 1 and independent of the initial leucine concentration. For leucine solution droplets with an initial diameter of about 50 µm, shell formation can be detected at a supersaturation of about 5, which, as expected, is larger than the previously calculated critical supersaturation of 3.5, because nucleation and some crystal growth must precede the point of shell formation. Therefore, the time of shell formation and its related normalized parameters, d_{c}/d_0 and τ_{c}, are suspected to be also a function of initial droplet diameter. These assumptions will be verified by comparing the morphologies of polydisperse spray-dried particles of different sizes of the same formulation later on. A detailed analysis of the combination of these effects is outside the scope of this study.

Interestingly, it was noticed that the points in Figure 3.5 can be fitted using a function such that $\tau_{\mathrm{c,leu}} = 1 - a\,(C_{0,\mathrm{leu}})^{2/3}$, where a is the fitting parameter. According to the explanation above, a is expected to be a function of the initial droplet diameter and possibly the evaporation rate for smaller droplets. Comparing this function to equations obtained from mass balance, such as Equations (3.6) and (3.9), a non-linear fit was performed on the data to find the diameter dependent coefficient k_{d0} such that

$$\tau_{\mathrm{c,leu}} = 1 - k_{d0}\,(E_{\mathrm{s,leu}} S_{0,\mathrm{leu}})^{2/3}\,, \tag{3.11}$$

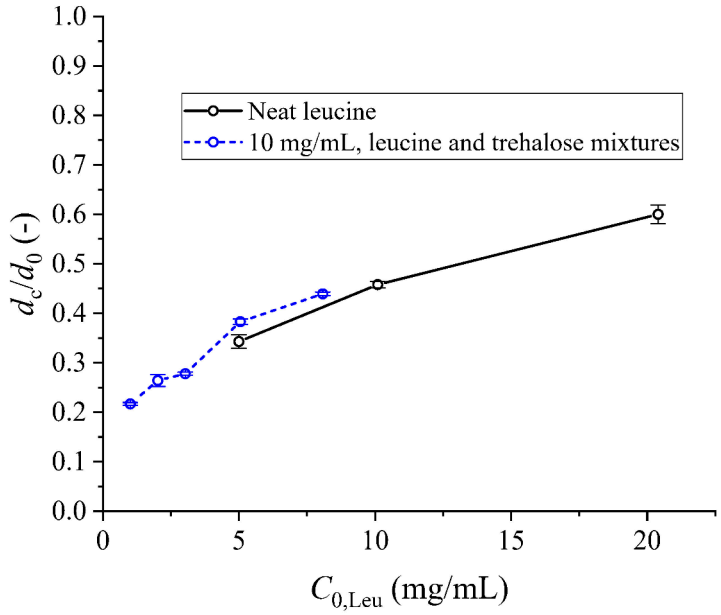

Figure 3.4: The normalized diameter of shell formation obtained from CK-EDB measurements, for $d_0 \approx 50$ µm.

which resulted in $k_{d0} = 0.35$ for the parameters of the CK-EDB experiments with initial diameters of about 50 µm. Like a, this coefficient should also be a function of other process parameters such as the evaporation rate. The sensitivity of this coefficient to other parameters is believed to be lower than it is to the droplet diameter, as it was observed that τ_c was practically constant for different droplets studied for a single formulation but at two different relative humidities (hence different evaporation rates). Using this empirical equation, one can predict the instance of shell formation for leucine in the course of droplet evaporation. This time-point can be compared to the critical points of other components in the system in order to predict the levels of surface coverage. The dimensionless time to reach critical supersaturation, τ_n, obtained from Equation (3.9), can also be compared to the time of shell formation of other components to check if leucine has enough time to nucleate in the first place. Previously, the time to reach saturation was used for this purpose [14], but the theoretical time to critical supersaturation and the time of shell formation are better approximations for the actual shell formation timing.

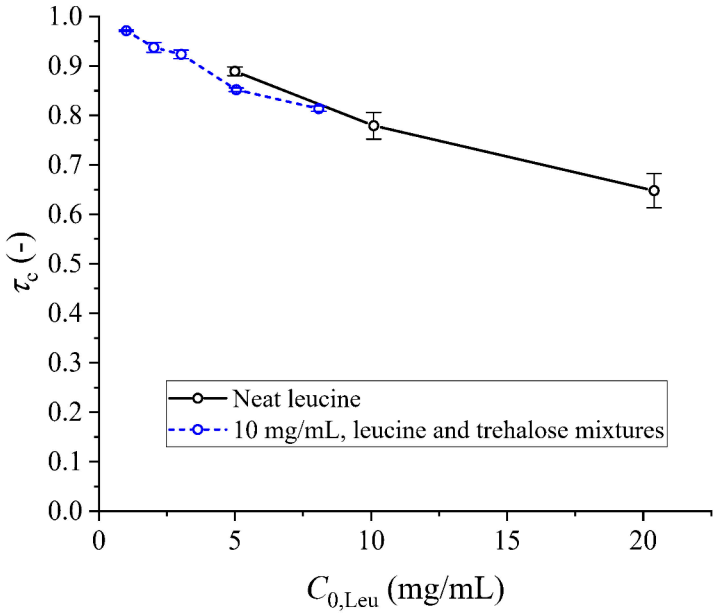

Figure 3.5: Normalized time of shell formation obtained from CK-EDB measurements, for $d_0 \approx 50$ µm. The normalization was performed using the droplet drying time. Larger values mean shell formation happens later and closer to the end of the evaporation period.

3.3.2 Monodisperse Droplet Chain Instrument

In order to measure the particle densities and show the corresponding particle morphologies of the cases studied using the CK-EDB instrument, similar formulations were analyzed using the droplet chain instrument (see Table 3.2). The SEM micrographs of these particles are shown in Figure 3.7. The first three micrographs for the neat-leucine cases show a morphology consistent with previously published results [31], namely a hollow core with a shell that consists of smaller individual pieces. Increasing the initial concentrations resulted in larger particles with thicker shells. This result is expected, as higher initial leucine concentrations mean critical supersaturation and the time of shell formation are reached earlier and at larger droplet diameters. It is apparent from the last four micrographs that decreasing the leucine content in a leucine/trehalose mixture causes the morphologies of the particles to change from hollow ones with shells to solid spheres. As will be seen for the spray-

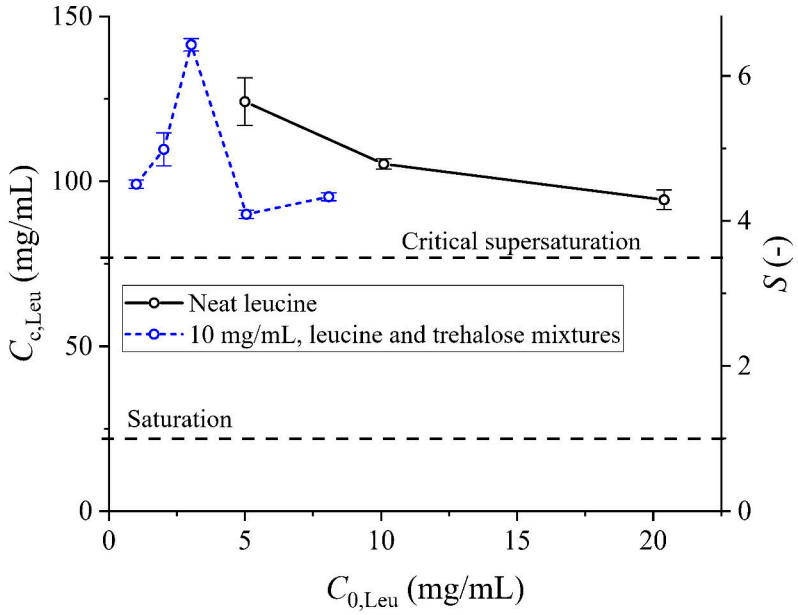

Figure 3.6: The mean leucine concentration and saturation ratios at the point of shell formation, obtained from the CK-EDB measurements, for $d_0 \approx 50$ µm. The dashed horizontal lines represent the saturation at the leucine solubility concentration of 22 mg/mL and the theoretical critical supersaturation ratio of 3.5.

dried particles, and as was also shown elsewhere [31], decreasing the leucine content also decreases its crystalline fraction. The ultrahigh magnification inset figures were included to show the patched surfaces due to presence of crystalline leucine compared to the relatively smooth surfaces of amorphous trehalose particles.

As explained previously, the projected area diameter of these particles was measured as a representation of their size. The resulting particle diameters, d_p, normalized by the measured initial diameters, d_0, are presented in Figure 3.8. Because of the high accuracy in the measurement of the initial droplet diameters and the high monodispersity of the particles, the particle densities could be obtained confidently using Equation (3.1). The measured particle densities are also shown in blue (right axis) in Figure 3.8. In this figure, error bars represent one standard deviation. As expected, increasing the initial leucine concentration caused the normalized particle diameters to increase, and the

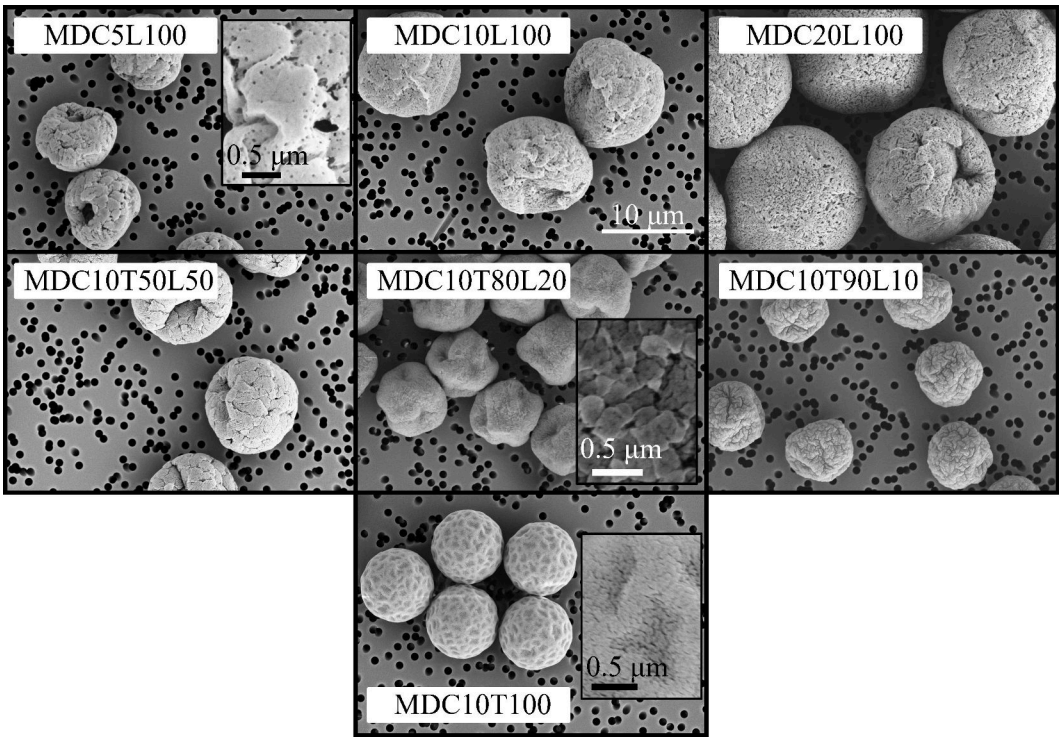

Figure 3.7: SEM micrographs of the particles generated using the monodisperse droplet chain setup at 20 °C with initial droplet diameters of about 40 µm. The 10-µm scale bar applies to all images except the inset figures, for which separate scale bars are provided. A label such as MDCαTβLγ means the formulation studied with the MDC instrument had a total feed concentration of α with trehalose and leucine mass fractions of β and γ, respectively.

particle densities to decrease. It was observed that at a leucine fraction of 50% the particle density was reduced by more than 60%. It was also observed from the two cases at 5 mg/mL leucine, MDC10T50L50 and MDC5L100, that the general morphology of the particles was similar. This fact points to previous observations that at mass fractions of up to around 80% trehalose does not interfere with the crystallization and shell formation of leucine [31]. It is also worthwhile noting that the general trend and the actual values in this figure are very similar to the data in Figure 3.4. These similarities may be due to the slow drying kinetics in the droplet chain and the CK-EDB instruments as well as to the relatively large initial droplet diameters in both instruments. Hence, enough time for crystal growth is available in both experimental techniques. Under these circumstances the lowest particle densities can be achieved by

choosing an initial leucine concentration close to its solubility of 22 mg/mL at room temperature.

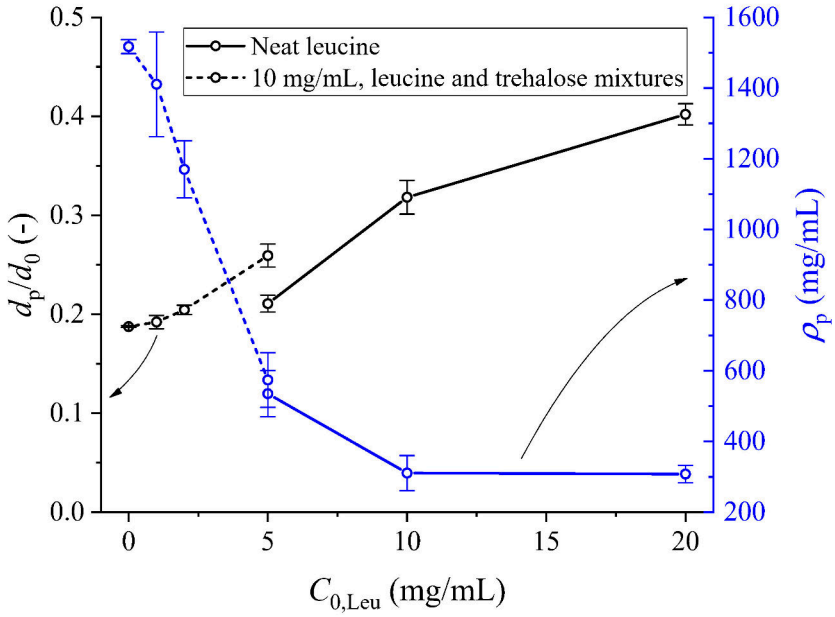

Figure 3.8: The measured normalized particle diameters and densities obtained from the monodisperse droplet chain setup at 20 °C with initial droplet diameters of about 40 µm.

3.3.3 Spray-Dried Powder

The SEM micrographs of the four different spray-dried formulations containing leucine and trehalose are shown in Figure 3.9. The increase in surface roughness due to the shell formation and crystallization of leucine is clear, which is an important factor for the reported enhancement of aerosolization properties of such powders [89, 90, 92]. Similar to the monodisperse particles obtained from the droplet chain, surfaces of the particles for which leucine is expected to be crystalline were composed of distinguishable crystals, as seen from the higher-magnified micrographs at the bottom row of Figure 3.9.

Another important note to take from these images of the polydisperse powders is the difference in morphologies observed for a single formulation. Larger particles were hollow with a thinner shell, while smaller particles were

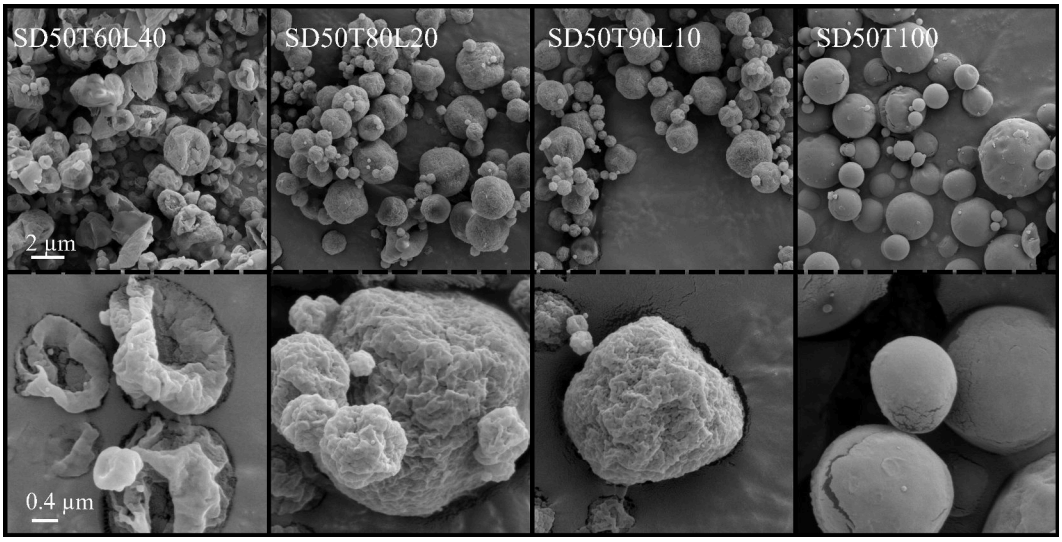

Figure 3.9: SEM micrographs of the spray-dried leucine/trehalose particles dried at an inlet temperature of 75 °C. The scale bars apply to each row, and each column is of the same formulation. A label such as SDαTβLγ means the spray-dried formulation had a total feed concentration of α with trehalose and leucine mass fractions of β and γ, respectively.

denser. This difference supports our previous remarks that the whole process of crystallization and shell formation cannot be normalized by the drying time as can be done for amorphous precipitation, *e.g.* for trehalose particles. This fact is also expected to cause variations in surface compositions of the particles, with larger particles having higher leucine surface fractions, as will be seen from the TOF-SIMS data below.

The leucine crystalline fractions obtained from the deconvolution of the Raman spectra are presented in Figure 3.10, accompanied by the results of Feng et al. [31]. Note that the total concentrations were different compared to the formulations studied in the present article, hence the differences between the data. Feng et al. mentioned that the formulation with 5% leucine fraction was dominantly amorphous, but quantification was not possible due to the very small amount of leucine in the particle. The trehalose was completely amorphous in all cases, as expected. In the current study, there was a transition from partially to completely crystalline leucine between leucine fractions of about 10% to 20%. A mixture of amorphous and crystalline molecules of the same material in the particles is undesirable for long-term stability. That

is because, in humid conditions, the crystals in the particles can act as nucleation sites for the crystallization of the amorphous content of the same material. In other words, the crystalline content of a material lowers the energy barrier for crystallization of its amorphous counterpart. This fact may cause crystallization in the particles, leading to physical instability.

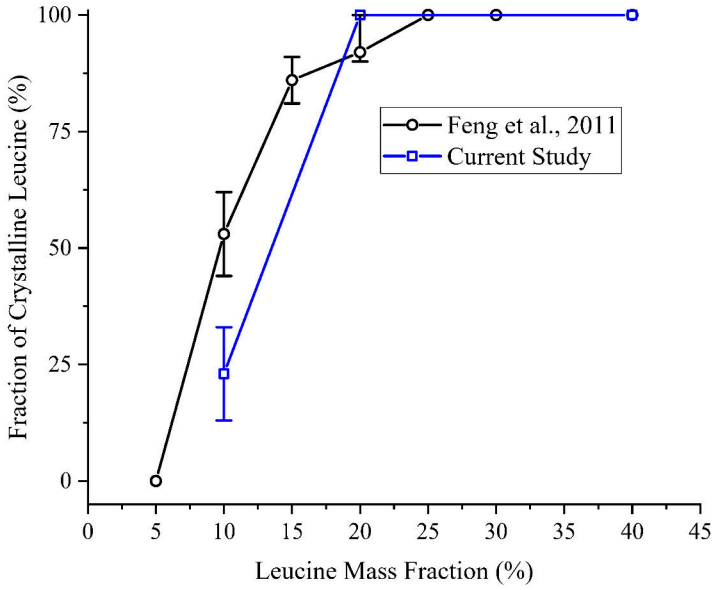

Figure 3.10: The fractions of crystalline leucine in spray-dried leucine/trehalose particles. The drying temperature was 75 °C in both studies, but the total feed concentrations were different.

The surface compositions of the spray-dried particles measured by TOF-SIMS are shown in Figure 3.11, with red and blue representing leucine and trehalose molecules, respectively. As expected, the average leucine surface composition increased by increasing the leucine feed fraction from 10 to 40%. It can be seen in all three cases that smaller particles had more trehalose on the surface than larger particles, confirming the previous remarks on size-dependency of the particle morphology.

The pixel-average surface compositions of the spray-dried leucine/trehalose particles from the TOF-SIMS spectra are plotted versus the bulk composition in Figure 3.12. These pixel-average values are presented for the whole powder,

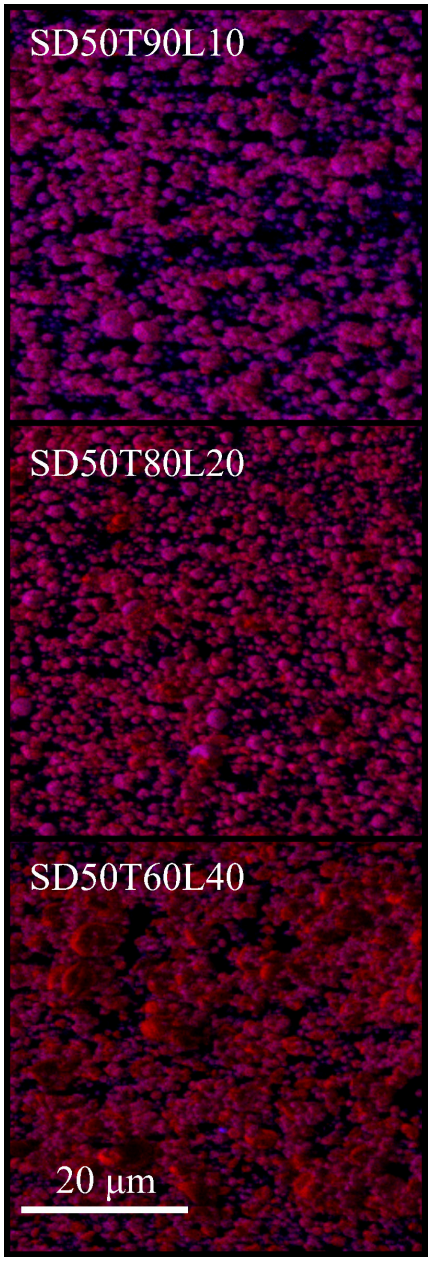

Figure 3.11: The surface compositions of the spray-dried leucine/trehalose particles from the TOF-SIMS measurements. Red represents leucine molecules and blue represents trehalose. The scale bar applies to all three images. A label such as SDαTβLγ means the spray-dried formulation had a total feed concentration of α with trehalose and leucine mass fractions of β and γ, respectively.

and for small, medium and large particle fractions. The error bars for the total averages are equal to the standard deviation of the pixel fractions of the whole frame. The total average leucine surface coverage is seen to increase

with leucine mass fraction. On average, 23% (mass basis) of the particles are covered by leucine at a mass fraction of 10%, compared to the 48% coverage at a mass fraction of 40%. It is also evident from these results that large particles have more leucine coverage than small particles in all cases. It is likely that these small particles are composed of mostly amorphous leucine with some small crystallinity, even for the case with the highest leucine mass fraction (SD50T60L40). This can be deduced from the fact that the surface coverage of the small leucine particles is smaller than even the bulk leucine fraction. This means that for these particles, the surface was enriched by trehalose not leucine, due to the larger Péclet number of trehalose compared to leucine in molecular form. Thus, there is no evidence of crystal growth. These small particles comprise only a very small mass fraction of the total powder. Hence, their effect on the crystallinity measurements using the Raman instrument are minimal. Nevertheless, it cannot be ruled out that the presence of even a small quantity of amorphous leucine in the powder can potentially hinder the long-term physical stability of the product in the form of both dry powder and suspension pressurized metered-dose inhalers (pMDIs).

In order to further interpret the phenomena explained above, the available time for leucine crystallization versus the initial droplet diameter of the spray-dried powder is shown in Figure 3.13. As opposed to the precipitation window explained in Equation (3.7), here the available time for crystallization was defined more precisely as the time for trehalose to reach a concentration of 830 mg/mL, less the time for leucine to reach a critical supersaturation of 3.5. Assuming a logarithmic normal distribution with a mass median diameter of 8 µm and an approximate geometric standard deviation of 2.2 for the atomized droplets, the $d_{0,50}$, $d_{0,16}$ and $d_{0,84}$ are also indicated by the vertical grey lines. It is evident from these data that the time available for crystallization increases sharply with increasing initial droplet diameter in all cases. Assuming a particle density of 1000 mg/mL and a feed concentration of 50 mg/mL, Equation (3.1) gives initial droplet diameters smaller than 2.7 µm for solid particles smaller than 1 µm. Hence, for these particles the time available for leucine crystallization is less than 1 ms. The difference in crystallization

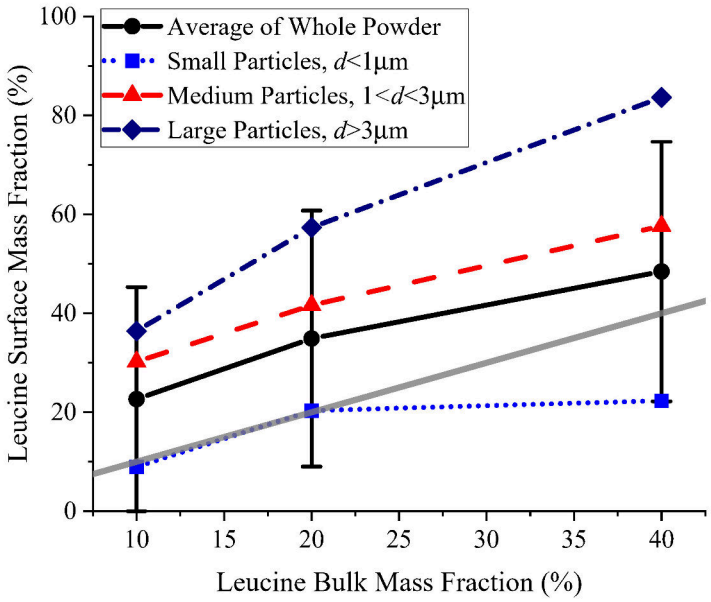

Figure 3.12: The pixel-average surface compositions of the spray-dried leucine and trehalose particles from the TOF-SIMS spectra. The total feed concentration was 50 mg/mL and the drying temperature was 75 °C for all cases. The grey line is the identity line ($x = y$).

times is the reason behind the large differences observed in the morphologies, leucine surface coverage and possibly the crystallinity of the polydisperse particles. The crystallization windows of a sample case for the CK-EDB and the droplet chain instrument are also shown in Figure 3.13 as the individual data points. It is apparent from these calculated values that for both of these large droplets enough time is available for complete crystallization of leucine, hence their similar behavior.

3.3.4 Application to Formulation Design

Based on the data available in the literature and the results obtained from the experiments conducted in this study, it is possible to design and analyze spray-dried particles containing leucine as a dispersibility enhancer. Such an approach has the potential to greatly reduce the number of experimental iterations required in the design of a spray-dried platform containing other excipients and actives intended for pulmonary delivery. The same framework

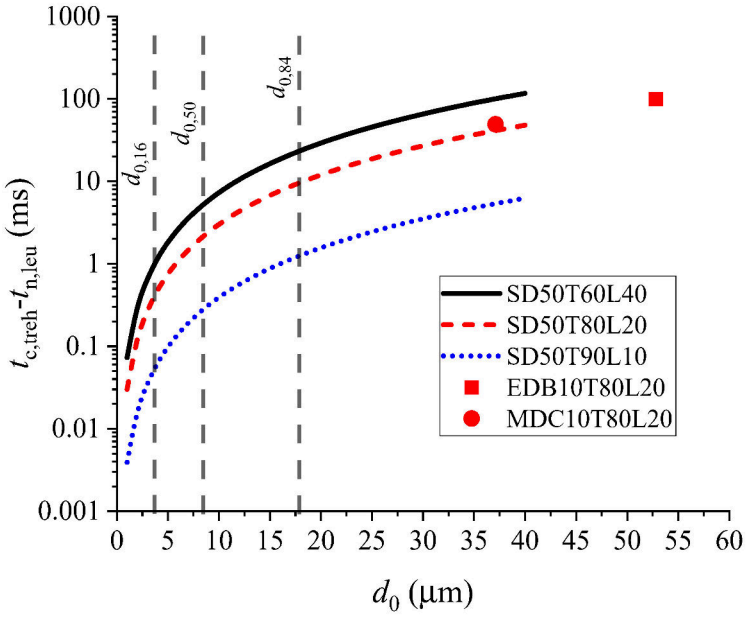

Figure 3.13: The available time for crystallization of leucine based on the difference between the time for trehalose to solidify and the time for leucine to reach the critical supersaturation, as a function of the initial droplet diameter. The curves apply to the spray-dried samples (drying temperature of 75 °C) accompanied by the vertical grey lines representing the approximate atomized droplet size distribution. The two individual data points represent a sample case of the electrodynamic balance and the droplet chain instruments (drying temperature of 20 °C).

may be used for other crystallizing components if the critical parameters are determined in a similar fashion.

A dispersibility enhancing excipient needs to attain enough surface coverage on the final particle to have the desired effects. If the solidification time of another excipient, τ_c, which is not intended to be on the particle surface, is smaller, it will be faster to precipitate, leading to a higher surface composition. Hence, the shell former should have the smallest τ_c compared to other excipients for maximum surface coverage. For a crystallizing component, such as leucine, the dimensionless time to reach critical supersaturation, τ_n, is also important. If the other excipients solidify near the surface before the crystallizing component can nucleate, then the shell former is expected to remain partially or completely amorphous. This is because in this case the shell for-

mer molecules do not have enough mobility to fit into a crystal lattice or reach the surface in the fast time scales of spray drying. For example, in the present case of leucine and trehalose particles, if trehalose reaches its critical concentration before leucine can nucleate, *i.e.* $\tau_{c,treh} < \tau_{n,leu}$, leucine will most likely be completely amorphous and will not have a very high surface coverage. On the other hand, if $\tau_{n,leu} < \tau_{c,treh} < \tau_{c,leu}$, then leucine is expected to be partially amorphous with low surface coverage. Lastly, if $\tau_{c,leu} << \tau_{c,treh}$, then most of leucine should have had enough time to crystallize and cover the surface. It should be noted that even if leucine does not crystallize in a formulation, it can still lower the surface energy of the particles due to its surface activity and molecular surface enrichment.

These considerations can be extended to other systems containing other excipients and APIs in order to design the formulation in such a way as to ensure optimal surface coverage by the shell former.

3.4 Conclusion

This study demonstrates that the combination of the results obtained from an electrodynamic balance, a monodisperse droplet chain instrument, and a spray dryer holds great potential for the study of particle formation of different excipients and APIs in spray-dried microparticles. These results may greatly reduce the experimental efforts necessary in the early stages of the formulation design of a solid dosage form.

It was confirmed that the surface accumulation of leucine is based on nucleation and crystal growth and that the presence of other materials in high concentrations can decrease surface enrichment due to crystallization. It was also observed that the surface coverage and solid phase of leucine, as a crystalline dispersibility enhancer, can be dependent on the initial droplet diameter due to the amount of time required to nucleate, crystallize and form a shell. This fact has important implications for scale-up and optimization of manufacturing parameters in these systems. A critical supersaturation ratio at which leucine can spontaneously nucleate was also determined theoreti-

cally and supported by experimentation. Furthermore, critical solidification and shell formation times were obtained for trehalose and leucine using the single-particle experiments, which can be used in the formulation design of systems containing these excipients to estimate leucine crystallinity and the extent of its surface coverage. The same methodology can be applied for other crystallizing excipients or actives.

Chapter 4

Trileucine as a Dispersibility Enhancer of Spray-Dried Inhalable Microparticles

The formation of trileucine-containing spray-dried microparticles intended for pulmonary delivery was studied in depth. A single-particle method was employed to study the shell formation characteristics of trileucine in the presence of trehalose as a glass former, and an empirical correlation was proposed to predict the instance of shell formation. A droplet chain instrument was used to produce and collect monodisperse particles to examine morphology and calculate particle density for different levels of trileucine. It was observed that the addition of only 0.5 mg/mL (10% w/w) trileucine to a trehalose system could lower dried particle densities by approximately 1 g/cm^3. In addition, a laboratory-scale spray dryer was used to produce batches of trileucine/trehalose powders in the respirable range. Raman spectroscopy demonstrated that both components were completely amorphous. Scanning electron microscopy and time-of-flight secondary ion mass spectrometry were used to study the particle morphologies and surface compositions. For all cases with trileucine, highly rugose particles with trileucine coverages of more than 60% by mass were observed with trileucine feed fractions of as little as 2% w/w. Moreover, it was seen that at lower trileucine content, smaller and larger particles of a polydisperse powder had slightly different surface compositions. The surface activity of trileucine was also modeled via a modified form of the

diffusion equation inside an evaporating droplet that took into account initial surface adsorption and eventual surface desorption due to droplet shrinkage. Finally, using the Flory-Huggins theory, it was estimated that at room temperature, liquid-liquid phase separation would start when the trileucine reached an aqueous concentration of about 18 mg/mL. Besides the surface activity of trileucine, this low concentration was assumed to be another reason behind the substantial effect of trileucine on the morphology of spray-dried particles due to early phase separation. The methodology proposed in this study can be used in the rational design of trileucine-containing microparticles.

4.1 Introduction

Spray drying is a continuous process of producing fine powder with a controlled size distribution through the rapid evaporation of a feed solution, suspension, or emulsion after atomization into a hot drying gas [34]. This production method is particularly useful in the production of microparticles containing pharmaceutical actives or biologics because of its accurate control of the outlet conditions, particle morphology, and size distributions [15]. Effective pulmonary delivery of dry powder necessitates specific particle characteristics for maximum delivery efficiency and therapeutic efficacy: 1) an approximate range of 1 to 5 micrometers in aerodynamic diameter for delivery to the lungs [1, 10], 2) acceptable physical and chemical stability for long-term shelf storage, and 3) low interparticle cohesion to allow for good dispersion and deagglomeration with minimal loss in the delivery device and the upper respiratory tract [121]. To achieve these properties, appropriate formulation excipients are used. For example, glass formers such as trehalose have been used both as bulking agents and as stabilizers of the biological components [83, 92, 96]. To improve the aerosolization characteristics of the powder, a specific class of excipients labeled as shell formers or dispersibility enhancers have been used; these include leucine [31, 92, 94, 122] and trileucine [29, 88, 123].

Trileucine is a tripeptide composed of three leucine residues and is used in the spray drying of pharmaceutical microparticles mostly as a dispersibil-

ity enhancer to produce low-density, non-cohesive and rugose particles [14, 88, 124]. It is a strongly surface-active material, typically does not crystallize during spray drying nor upon storage, and has a low aqueous solubility of about 6.8 mg/mL at neutral pH [29]. These characteristics have been reported to be responsible for considerable increase of surface roughness and efficient dispersibility enhancement of particles containing small quantities of trileucine in the formulation [88, 123, 125]. Furthermore, the high surface coverage of trileucine in spray-dried particles, as along with its high glass transition temperature of 104 °C, are believed to be the reasons behind its considerable improvement in the stability of biologics and bacteriophages during production and upon storage [29, 125]. Due to the high surface activity of trileucine, the molecules adsorbed on the droplet surface are believed to have their hydrophobic tails directed outwards, a feature that may explain the observed moisture protection features of trileucine [123].

Given its aforementioned properties, trileucine can be considered a dispersibility-enhancing excipient with far-reaching benefits. The downside of using trileucine is its current high price compared to that of other less effective alternatives such as leucine. Hence, it is desirable to include as little trileucine as possible in the formulation while still meeting the design criteria. Also, the use of particle formation models becomes relevant here, as they allow reductions in the number of experimental iterations during the formulation development by predicting the sequence of surface accumulation and solidification of different excipient and actives [14, 33]. The use of such models is less complicated for excipients and actives that are not surface-active and do not crystallize during spray drying [14], *e.g.* trehalose [32], pullulan [96], and budesonide [37]. These models have been extended to crystallizing components [126], but the incorporation of surface activity into such models has not been achieved. Further, observations that a non-surface-active dipeptide (L-tyrosyl-L-isoleucine) with low solubility, very close to the solubility of trileucine, can dry into low-density amorphous particles suggest that surface activity alone cannot be responsible for the shell formation properties of trileucine and that amorphous phase separation must also contribute [32, 127]. The formation of

particles containing trileucine is complex and cannot be described comprehensively by the current particle formation models. More information is required for the prediction of the instances of shell formation and surface coverage of trileucine in a successful rational design of the formulation.

To address the aforementioned complexities, three different and complementary experimental methods are employed here to study the particle formation characteristics of trileucine in the presence of trehalose as a glass former. These tools were previously used together successfully in explaining the particle formation of leucine [122]. A Comparative-Kinetics Electrodynamic Balance (CK-EDB) was used to measure the approximate time of shell formation from instantaneous sizing of single aerosol droplets trapped in a controlled environment [95, 105]. A monodisperse droplet chain instrument was also used to collect the dried particles for electron microscopy and measurement of the particle densities [59, 87, 95]. Furthermore, a lab-scale spray dryer was used to produce powders with diameters in the respirable range and to produce enough material for further characterization techniques. The effect of surface activity of trileucine as along with its mechanism of phase separation are also predicted theoretically.

4.2 Materials and Methods

4.2.1 Materials

The spray-dried solutions were prepared using HPLC grade water (Cat. No. W5-4, Fisher Scientific, Ottawa, ON, Canada) with total solids contents ranging from 1 to 50 mg/mL and the appropriate fractions of trehalose and trileucine. Crystalline D-(+)-trehalose dihydrate was bought directly from the vendor (Cat. No. BP2687-1, Fisher Scientific, Ottawa, ON, Canada), while spray-dried amorphous trileucine was used in solution preparation to avoid issues with low solubility. Raw crystalline trileucine (Cat. No. H-3915, Bachem, Torrance, CA, USA) was used in the preparation of the amorphous batch.

4.2.2 Experimental Methods

Comparative-Kinetics Electrodynamic Balance (CK-EDB)

A comparative-kinetics electrodynamic balance was used to estimate the shell formation behavior of trileucine-containing systems. The evaporation and solidification behavior of single solution droplets ($d_0 \sim 50$ µm) were analyzed in a comparative-kinetics electrodynamic balance [95, 105, 122]. For each experiment, a droplet-on-demand dispenser (MJ-ABP-01, MicroFab Technologies, Plano, Texas, USA) generated a single droplet, charged on generation by applying a DC voltage to an electrode near the tip. The droplet was then trapped inside a controlled environment with the help of an AC potential difference applied via two sets of concentric cylindrical electrodes mounted vertically opposite one another. The drag force from a gas flow and the gravitational force on the droplet were counteracted by applying an additional DC voltage to the bottom electrodes that was dynamically controlled to account for the change in droplet mass during drying. A 532 nm laser illuminated the particle, producing a scattered pattern and a phase-function both of which were captured on a CCD every ∼10 ms at a forward scattering angle of 45° over a range of 24°. The instantaneous size of the droplet was measured within an accuracy of ±100 nm using the fringe spacing in the obtained phase-functions and the geometric-optics approximation to Mie theory [105]. The morphology of the particle during drying was also approximated by analyzing the irregularities in the phase-function [109]. The instance of solidification and shell formation was then determined from the instantaneous morphology data and deviation from a constant evaporation rate [122].

The studied formulations using the EDB instrument are presented in Table 4.1. For each case, three to four droplets were studied at a chamber temperature of 20 °C and relative humidity of ∼35%. The formulations were selected so that the occurrence of solidification and shell formation would be at sufficiently large diameters for detection in the CK-EDB instrument and the trileucine concentrations would cover low to high initial saturations. The low drying temperature and high humidity level were chosen based on the

Table 4.1: The samples studied using the electrodynamic balance, accompanied by their compositions, trileucine initial saturation (based on a solubility of 6.8 mg/mL), and measured average initial droplet diameters. The drying temperature was set to 20 °C and the relative humidity was ∼35% for all cases. The uncertainties of the initial droplet diameters are the standard deviation of multiple droplets studied for each case.

Sample Name	**Total Solids Content (mg/mL)**	**Trehalose Mass Fraction (%)**	**Trileucine Mass Fraction (%)**	**Trileucine Initial Saturation (−)**	d_0 **(µm)**
EDB1TL100	1	0	100	0.15	53.8±0.0
EDB2TL100	2	0	100	0.29	52.9±0.1
EDB5TL100	5	0	100	0.73	53.0±0.2
EDB5T100	5	100	0	0.00	53.6±0.2
EDB5T90TL10	5	90	10	0.07	52.6±0.0
EDB5T80TL20	5	80	20	0.15	52.6±0.3
EDB5T70TL30	5	70	30	0.22	53.3±0.1
EDB5T50TL50	5	50	50	0.37	53.7±0.0

instrument limitations and to result in high temporal resolution during the measurements.

Monodisperse Droplet Chain Instrument

A droplet chain instrument was used to produce and collect monodisperse microparticles [87, 95, 96, 107]. A droplet-on-demand piezoceramic dispenser with an orifice diameter of 40 µm (MJ-AL-HT-40-8MX, MicroFab Technologies, Plano, Texas, USA) injected droplets into a glass tube with a frequency of 60 Hz. Dry air passed through the flow tube from above with a flow rate of 10 to 15 L/min and a temperature of approximately 20 °C. Dried particles falling down the tube were then collected on a membrane filter with a pore size of 0.8 µm (Isopore Polycarbonate, Millipore, Darmstadt, Germany) attached on an SEM stub with a hole drilled in the center and connected to a vacuum source. An imaging system was used to measure the initial droplet diameters. Approximately two hundred images were taken at the start and near the end of each experiment; these were then analyzed using MATLAB [110] to calculate the average initial droplet diameter and the corresponding standard deviation of each case. The formulations studied using the monodisperse droplet chain

Table 4.2: The samples studied using the droplet chain instrument, accompanied by their compositions, trileucine initial saturation (based on a solubility of 6.8 mg/mL), and measured average initial droplet diameters. The drying temperature was approximately 20 °C for all cases. The uncertainties of the initial droplet diameters are the standard deviations of two hundred droplets per case.

Sample Name	**Total Solids Content (mg/mL)**	**Trehalose Mass Fraction (%)**	**Trileucine Mass Fraction (%)**	**Trileucine Initial Saturation (−)**	d_0 **(µm)**
MDC1TL100	1	0	100	0.15	36.2±0.3
MDC2TL100	2	0	100	0.29	34.5±0.6
MDC5TL100	5	0	100	0.73	38.8±0.2
MDC10T100	10	100	0	0.00	42.4±0.1
MDC5T90TL10	5	90	10	0.07	34.9±0.3
MDC5T80TL20	5	80	20	0.15	36.8±0.2
MDC5T50TL50	5	50	50	0.37	35.9±0.2

instrument were chosen in such a way as to produce particles approximately resembling the final dried particles of the CK-EDB measurements and are presented in Table 4.2.

Spray Drying

The spray-dried powders were manufactured using a modified laboratory-scale spray dryer (B-191, Büchi Labortechnik AG, Flawil, Switzerland) with a customized twin-fluid atomizer [96]. For all formulations, the inlet temperature was set to 75 °C, the atomizer had an air-to-liquid ratio of 10, the drying gas flow rate was set to 540 L/min, and the liquid feed flow rate was 2.5 mL/min. These process parameters resulted in an outlet temperature of about 49 °C and a predicted outlet relative humidity of about 7% [122]. For the specific twin-fluid atomizer used, the initial mass median diameter of the atomized droplets was estimated to be around 8 µm [111]. The powders collected in the cyclone were then stored in dry conditions (RH∼0%) at room temperature. The compositions of the spray-dried formulation are shown in Table 4.3. These compositions were chosen to cover a range from low to high trileucine initial saturations, as well as to produce particles in the respirable range.

Table 4.3: The compositions of the spray-dried formulations. Inlet temperature was 75 °C for all cases and the estimated mass median diameter of the atomized droplets was ∼8 µm.

Sample Name	**Total Solids Content (mg/mL)**	**Trehalose Mass Fraction (%)**	**Trileucine Mass Fraction (%)**	**Trileucine Initial Saturation (−)**
SD50T100	50	100	0	0
SD50T98TL2	50	98	2	0.15
SD50T95TL5	50	95	5	0.37
SD50T90TL10	50	90	10	0.73

4.2.3 Characterization Techniques

Scanning Electron Microscopy

A field emission scanning electron microscope (Sigma FESEM, Zeiss, Jena, Germany) was used to obtain the micrographs for this study. The accelerating voltage was 5 kV, and working distances ranged from 6.5 to 8.5 mm.

The monodisperse particles collected from the droplet chain instrument were sized from the SEM micrographs via manual calculation of the projected area of about 40 particles per sample using ImageJ software [112]. The resulting projected area diameter is equal to the volume equivalent-diameter only if the particles are spherical. In the case of highly folded particles, this method provides an approximate diameter.

Raman Spectroscopy

The solid phases of the spray-dried powders were determined using a custom-built dispersive Raman spectrometer, the operation and design of which have been explained elsewhere [113]. Raw crystalline materials were analyzed to provide the reference spectra for crystalline trehalose and trileucine, and spray-dried trehalose and trileucine powders were used as their amorphous reference spectra [88].

Time-of-Flight Secondary Ion Mass Spectrometry

A TOF-SIMS instrument (TOF.SIMS^5, ION-TOF GmbH, Münster, Germany) with a Bi_3^+ source operating at 30 keV energy was used to measure the surface

compositions of the spray-dried particles to an average depth of 3-5 nm [114]. Each measurement was performed on a raster of 200 µm × 200 µm with a frame of 1024×1024 pixels. The data processing was performed on bins of 512×512 pixels of the original frames. The raw materials were also analyzed to give the reference spectrum of each component. The pixel compositions were then obtained by fitting the spectrum to a linear combination of the reference spectra. More details on the post-processing of the TOF-SIMS data can be found elsewhere [115].

The processed data were then converted to 8-bit RGB images with the pixel strength of each component giving the respective color intensity (0-255). The resulting images were analyzed to find the average surface compositions of the whole powder, as well as small ($d_\mathrm{p} < 1$ µm), medium ($1 < d_\mathrm{p} < 3$ µm), and large ($d_\mathrm{p} > 3$ µm) particle fractions. More details about the methodology with which the particles were sized and binned are given elsewhere [122].

4.2.4 Theoretical Aspects of Particle Formation

Particle Formation Theory for a Surface-Active Component

Trileucine is a surface-active material with a strong tendency to adsorb on the air-water interface and form a molecular monolayer. The approach used to predict the rate of surface adsorption of a surface-active material on the interface of an evaporating microdroplet is described below.

The surface adsorption of a surface-active material can be obtained from the equilibrium surface tension data at a specific temperature via the simplified Gibbs adsorption equation as follows [128]

$$\Gamma_\mathrm{eq} = -\frac{1}{n\mathrm{R}T} \cdot \frac{\mathrm{d}\sigma}{\mathrm{d}(\ln C)}, \tag{4.1}$$

where Γ_eq is the equilibrium surface excess in mol/m^2, $n = 1$ for non-ionic or zwitterionic solutes and $n = 2$ for one-by-one ionic solutes in the absence of any extra electrolyte [129], R is the universal gas constant, T is the solution temperature in K, σ is the surface tension in N/m, and C is the solute bulk concentration in mg/mL. For trileucine at pH levels close to the neutral value,

the majority of the solute will be in zwitterionic form [29]; hence n is here assumed to be equal to 1.

The experimental tensiometry data are fitted using different empirical isotherms such as the Szyszkowski surface equation of state, defined as [129]

$$\sigma = \sigma_0 - n\mathrm{R}T\Gamma_{\max} \ln\left(1 + K_{\mathrm{L}}C\right), \tag{4.2}$$

where σ_0 is the surface tension of the neat solvent ($\sim$ 72 mN/m at 25 °C for water) and K_{L} is the Langmuir equilibrium adsorption constant. The combination of Equations (4.1) and (4.2) results in the Langmuir isotherm, which gives the equilibrium surface excess values at different bulk concentrations as follows:

$$\Gamma_{\mathrm{eq}} = \Gamma_{\max}\left(\frac{K_{\mathrm{L}}C}{1 + K_{\mathrm{L}}C}\right). \tag{4.3}$$

The degree of surface activity of trileucine can be identified from the equilibrium surface tension data in Figure 4.1 [29]. The concentration dependence of the surface tension of aqueous trileucine solutions is shown for two temperatures of 25 °C and 45 °C, which represent typical droplet wet-bulb temperatures encountered in spray drying. Non-linear fits to Equation (4.2) are shown in Figure 4.1 with $\Gamma_{\max} = 2.8 \times 10^{-6}$ mol/m^2 (or 0.99 mg/m^2) and $K_{\mathrm{L}} = 13.3$ mL/mg at 25 °C; and $\Gamma_{\max} = 2.4 \times 10^{-6}$ mol/m^2 (or 0.87 mg/m^2) and $K_{\mathrm{L}} = 15.5$ mL/mg at 45 °C. The amount of trileucine that can be adsorbed onto the air-water interface at different bulk concentrations can now be estimated using Equation (4.3). For a trileucine initial bulk concentration of 0.5 mg/mL, the minimum value encountered in this study, the equilibrium surface excess is estimated to be around 0.9 of the maximum surface excess, $\Gamma_{\max}$. Hence, a maximum surface excess of 0.99 mg/m^2 at 25 °C will be used as a simplification in the subsequent calculations.

The surface adsorption of the surface-active molecules is composed of three stages: diffusion of the molecules towards a domain immediately below the interface; adsorption of these molecules from this subsurface domain onto the interface; and, finally, reconfiguration of the molecules on the interface according to their hydrophobic/hydrophilic orientation [130, 131]. For trileucine, a simple tripeptide, it can be assumed that surface adsorption kinetics are solely

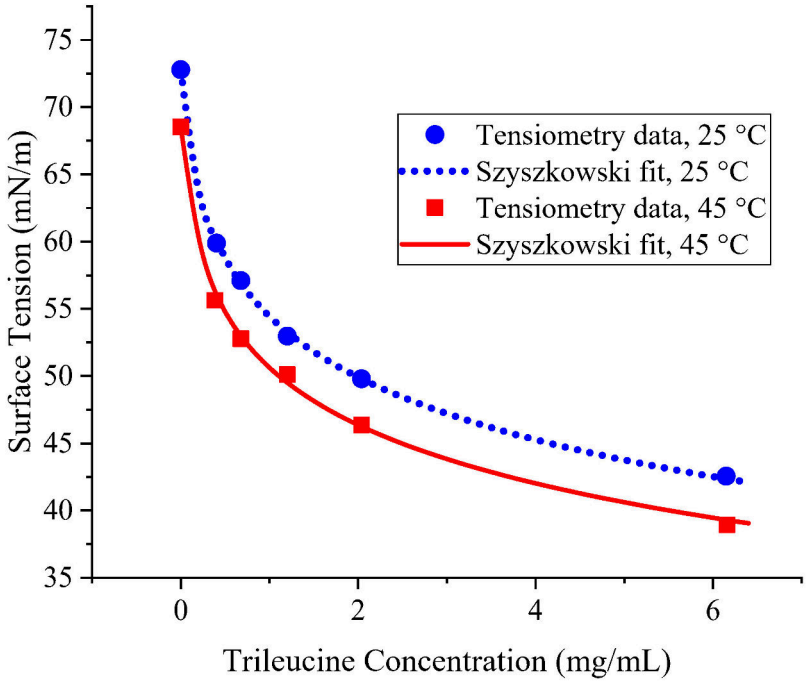

Figure 4.1: The equilibrium surface tension of aqueous trileucine solutions [29] accompanied by the non-linear fit based on the Szyszkowski surface equation of state.

controlled by the diffusion of the molecules from the bulk to the surface. This is a reasonable assumption as the incorporation of such a small molecule into the adsorbed monolayer and the consequent reorientation is rapid [131]. In such a case, the minimum theoretical time to reach a specific surface excess, t_Γ, can be approximated from the Ward and Tordai equation [132, 133]:

$$t_\Gamma = \frac{\pi \Gamma^2}{4 C_\mathrm{b}^2 D}. \tag{4.4}$$

Here, D is the diffusion coefficient of the surface-active solute in the solution. Note that this equation was derived for a semi-infinite solution volume with a constant bulk concentration of C_b. This is not the case in a droplet during spray drying because the bulk concentration increases as the droplet shrinks. If the initial concentration of trileucine is used in conjunction with the maximum surface excess calculated previously, the time to reach surface saturation can be obtained as an approximate threshold. The values obtained from Equation (4.4) are expected to be reasonable for large droplets but underestimate the actual timescale obtained from the solution of the diffusion equations

inside a microdroplet. This is because the amount of material needed to cover the surface relative to the available material inside the droplet increases as the droplet diameter decreases. Hence, for small droplets, surface adsorption can deplete the surface-active material and cause the bulk concentration to decrease considerably, making the use of Equation (4.4) questionable [134].

An accurate prediction of adsorption of a surface-active component during spray drying requires the solution of the internal diffusion equation with appropriate boundary conditions. The adsorption of the surfactant molecules from the subsurface domain to the interface causes a drop in the solute concentration near the surface. This drop in local concentration induces a diffusional flux from the inside of the evaporating droplet towards the surface as opposed to the diffusion from the surface to the center of the droplet for non-surface-active solutes due to the evaporation and surface enrichment [33]. The adsorption continues until the surface excess concentration reaches the maximum value, $\Gamma_{\max}$. Upon reaching this maximum surface concentration, further shrinkage of the droplet surface due to evaporation causes desorption of the molecules from the interface into the solution in order to maintain equilibrium, *i.e.* $\Gamma = \Gamma_{\max}$ [129].

The radial distribution due to the diffusion of a component, i, inside of an evaporating droplet can be obtained via the solution of the following equation for conservation of mass [95]

$$\frac{\partial C_i}{\partial t} = \frac{4D_i}{d^2}\left(\frac{\partial^2 C_i}{\partial R^2} + \frac{2}{R}\frac{\partial C_i}{\partial R}\right) - \frac{\kappa R}{2d^2}\frac{\partial C_i}{\partial R}, \tag{4.5}$$

where C_i is the instantaneous concentration of this component at different radial coordinates, d is the instantaneous droplet diameter, $R = 2r/d$ is the dimensionless radial coordinate, and $\kappa = -\mathrm{d}d^2/\mathrm{d}t$ is the evaporation rate. The values of the evaporation rate for different drying temperatures can be found in previous studies [122]. Equation (4.5) can be solved with the appropriate boundary conditions, $\partial C_i/\partial R = 1$ at $R = 0$ (droplet center) and $\partial C_i/\partial R - \mathrm{Pe}_i C_i = 0$ at $R = 1$ (surface) for non-surface-active components [32, 95]. Here, $\mathrm{Pe}_i = \kappa/8D_i$ is the Péclet number of the ith component. The dis-

cretized physical domain of a droplet, including the subsurface control volume and the adsorbed monolayer on the surface, is shown schematically in Figure 4.2. For a surface-active material, the surface boundary condition needs to be modified to account for the adsorption of the molecules onto the interface before reaching surface saturation ($\Gamma < \Gamma_{\max}$) as well as for desorption after reaching saturation ($\Gamma = \Gamma_{\max}$). Here, some assumptions are made to simplify the problem. First, before surface saturation, any material that reaches the subsurface (the control volume at $R = 1$) is instantaneously adsorbed onto the interface, irrespective of the number of molecules already adsorbed. Second, after saturation, the surface excess, Γ, will always remain equal to the maximum surface excess, $\Gamma_{\max}$, and further reduction of the droplet surface area due to evaporation will cause instantaneous desorption of the molecules back into the subsurface. In other words, while $\Gamma < \Gamma_{\max}$, the surface acts as an ideal sink and when $\Gamma = \Gamma_{\max}$, it acts as an ideal source. Furthermore, as mentioned before, it is assumed that the equilibrium surface excess, Γ_{eq}, is always equal to the maximum surface excess, $\Gamma_{\max}$. Consequently, the modified boundary conditions on the surface ($R = 1$) are as follows:

$$\begin{cases} C_i = 0 & \text{for } \Gamma < \Gamma_{\max}, \\ \frac{\partial C_i}{\partial R} - \text{Pe}_i C_i - \frac{4\text{Pe}_i \Gamma_{\max}}{d} = 0 & \text{for } \Gamma = \Gamma_{\max}. \end{cases}$$

The first condition is the Dirichlet boundary condition for an infinite source near the surface, and the second condition accounts for the mass flux of the surface-active component's release into the subsurface due to the evaporation.

After the solution of Equation (4.5) at each timestep, the instantaneous mass of the component on the surface needs to be updated accordingly. The numerical time advancement of Equation (4.5) allows estimation of the time required for monolayer formation and instantaneous radial concentration of trileucine inside the droplet. Comparing this time scale to similar scales of solidification or shell formation of other excipients and actives, it is possible to approximate the extent of surface coverage and morphology of the particles. The use of such a predictive tool during the formulation design of inhalable particles is discussed in the next section.

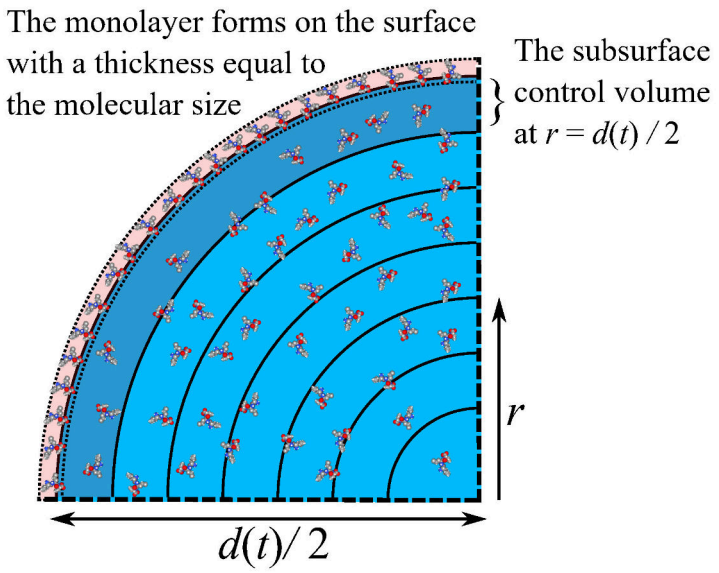

Figure 4.2: A schematic showing the discretized domains in a spherically symmetric coordinate system. The subsurface control volume is at $r = d/2$ with a finite thickness that depends on the instantaneous droplet diameter and the number of radial nodes considered. The adsorbed monolayer has a negligible thickness equal to the molecular size of the adsorbed molecules. These adsorbed molecules do not take part in the diffusion in the bulk unless they are desorbed back into the subsurface.

Phase Separation Considerations

One of the key properties behind the dispersibility enhancing abilities of trileucine has been hypothesized to be its surface activity [14, 29, 123], similar to that of other surface-active materials, such as bovine serum albumin (BSA), hydroxypropyl methylcellulose (HPMC), and poloxamer [93, 131], but without much consideration given to the phase separation mechanisms involved. It was previously demonstrated that spray-dried BSA, HPMC, and poloxamer at low concentrations had high surface coverage due to monolayer surface adsorption [93]. The much larger BSA molecules ($\sim$ 66 kDa) had lower surface coverages compared to the smaller Poloxamer ($\sim 8-10$ kDa) and HPMC molecules ($\sim$ 10 kDa), confirming that surface coverage was mostly controlled by surface adsorption of the surface-active molecules (discussed in the previous subsection) and not early solidification. It was also indicated that BSA and HPMC induced rugose morphologies, while poloxamer did not change the smooth morphology

of the control system [93]. The lower dilatational modulus of the poloxamer solutions was reported to be the possible cause of the production of smooth particles. Among other possible explanations, the rather different aqueous solubilities of BSA ($\sim$ 40 mg/mL) and HPMC ($\sim$ 10 mg/mL) compared to the much higher solubility of poloxamer (very soluble) might be another cause of the difference in particle morphologies due to the earlier shell formation of the former components. The solubility of trileucine was previously altered through changes to the solution pH, resulting in different morphologies for the spray-dried particles [29]. This is difficult to explain if surface activity is the only mechanism for particle formation, because surface activity is not a strong function of pH [29]. Moreover, the low solubility of surface-active compounds was previously stated to cause early liquid-liquid phase separation [135]. Consequently, to explain the rugose morphologies observed in the formulations containing trileucine, a detailed analysis of the phase separation mechanism is also required.

For crystalline shell formers, the surface concentrations are usually compared to a threshold, such as the solubility limit or a critical supersaturation at which nucleation can commence [33, 122]. For a material that does not crystallize during spray drying, the surface concentrations at which solidification occurs have been compared to the true density of the material [14]. However, such explanations cannot account for the early shell formation of trileucine, since an adsorbed monolayer on the surface does not increase the surface concentration to values close to the density of trileucine (more than 1000 mg/mL) and hence cannot have enough rigidity to form a solid shell without further solidification and phase separation. It is therefore hypothesized that the mechanism of shell formation and phase separation for trileucine is spinodal decomposition in the unstable regime in the free energy diagram of the aqueous solution.

At any given temperature, one can find the instability regime of a mixture from the free energy diagram. The instability starts at compositions at which the second derivative of the free energy with respect to concentration becomes negative. These points are usually called the spinodal points and are the

boundaries of the spinodal region at which, in contrast to the metastable region, the system is unstable and readily phase separates without the presence of any kind of energy barrier or nucleation barrier [136]. In the spinodal region, the system is assumed to undergo a liquid-liquid phase separation into water-rich and water-lean states [137]. The phase diagram of aqueous trileucine solutions was estimated as explained below using the Flory-Huggins theory to help understand the actual mechanisms of phase separation.

Flory-Huggins theory, an extension of the regular solution theory, was originally derived for polymer solutions to account for the different molecular volumes of the solute and the solvent [138]. Taking into account the large difference in molar volumes of trileucine ($\sim$ 341 cm^3/mol) and water ($\sim$ 18 cm^3/mol), the Flory-Huggins theory was used to estimate the phase diagram of trileucine-water systems. A ternary Flory-Huggins procedure would be required for an optimal estimation of a water-trehalose-trileucine system. Here, the presence of trehalose in the system was neglected for simplicity.

Based on the Flory-Huggins theory, the free energy of mixing of a binary system, ΔG_{mix}, at a temperature, T, can be expressed as the combination of enthalpic and entropic terms as follows [138]

$$\Delta G_{\text{mix}} = n\text{R}T\left(x_1 \ln \phi_1 + x_2 \ln \phi_2 + x_1 \phi_2 \chi_{1,2}\right), \tag{4.6}$$

where n is the total number of moles in the system, R is the universal gas constant and x_i is the mole fraction of a component. $\phi_1 = x_1/\left(x_1 + Nx_2\right)$ and $\phi_2 = Nx_2/\left(x_1 + Nx_2\right)$ are the volume fractions of the solvent and the solute, respectively, while N is the ratio of the molar volumes of the solute and the solvent. Based on this notation, subscripts 1 and 2 refer to the solvent and solute molecules, respectively, and are not interchangeable. The interaction parameter, $\chi_{1,2}$, accounts for the differences in intermolecular forces between the solvent and solute molecules and, for solutions containing polar and hydrogen bonds, can be obtained from the Hansen solubility parameters as [139, 140]

$$\chi_{1,2} = \frac{V_1}{\mathrm{R}T}\left[(\delta_{1,\mathrm{d}} - \delta_{2,\mathrm{d}})^2 + 0.25\,(\delta_{1,\mathrm{p}} - \delta_{2,\mathrm{p}})^2 + 0.25\,(\delta_{1,\mathrm{hb}} - \delta_{2,\mathrm{hb}})^2\right], \quad (4.7)$$

in which, V_1 is the molar volume of the solvent. The Hansen solubility parameters $\delta_{i,\mathrm{d}}$, $\delta_{i,\mathrm{p}}$ and $\delta_{i,\mathrm{hb}}$ account for the dispersion forces, polar forces, and hydrogen bonding interactions, respectively. The Hansen solubility parameters of trileucine were calculated using two different group contribution methods of Hoy and Van Krevelen [141]. The average value of the solubility parameters obtained from these two methods was used in this study. The obtained values were $\delta_{\mathrm{tl,d}} = 15.8$ MPa$^{1/2}$, $\delta_{\mathrm{tl,p}} = 7.8$ MPa$^{1/2}$ and $\delta_{\mathrm{tl,hb}} = 9.6$ MPa$^{1/2}$. For water, the available Hansen solubility parameters, $\delta_{\mathrm{w,d}} = 15.5$ MPa$^{1/2}$, $\delta_{\mathrm{w,p}} = 16.0$ MPa$^{1/2}$ and $\delta_{\mathrm{w,hb}} = 42.3$ MPa$^{1/2}$ were used [140]. The interaction parameter of the trileucine-water system was then calculated to be $615.3/T$, with the temperature in Kelvin. The Gibbs free energy of mixing was obtained for this binary system at any given temperature and composition. The solution of $\partial^2 \Delta G_{\mathrm{mix}}/\partial x_1^2 = 0$ resulted in the determination of the spinodal points.

The spinodal curves for this binary system versus trileucine concentration are shown in Figure 4.3 between 5 °C and 100 °C. At a solution temperature of 25 °C, the trileucine mole fraction at the left spinodal point was calculated to be about 0.09%, corresponding to a concentration of $C_{\mathrm{sp,Leu3}} = 18$ mg/mL. Based on this simplified model, it can be assumed that upon reaching this concentration, trileucine undergoes spontaneous liquid-liquid separation into water-rich and trileucine-rich phases. During spray drying, the phase separation would most likely start near the droplet surface due to the higher local concentration (in the subsurface domain due to the surface recession) and the presence of the adsorbed monolayer at the interface. This kind of liquid-liquid phase separation was previously put forward as an explanation for the core-shell structure of atmospheric aerosols containing surface-active organic compounds with low aqueous solubility [135, 142].

As the liquid-liquid phase separation and spinodal decomposition are a bulk process with a higher probability of separation near the droplet surface, to predict the onset of phase separation the subsurface concentration can be

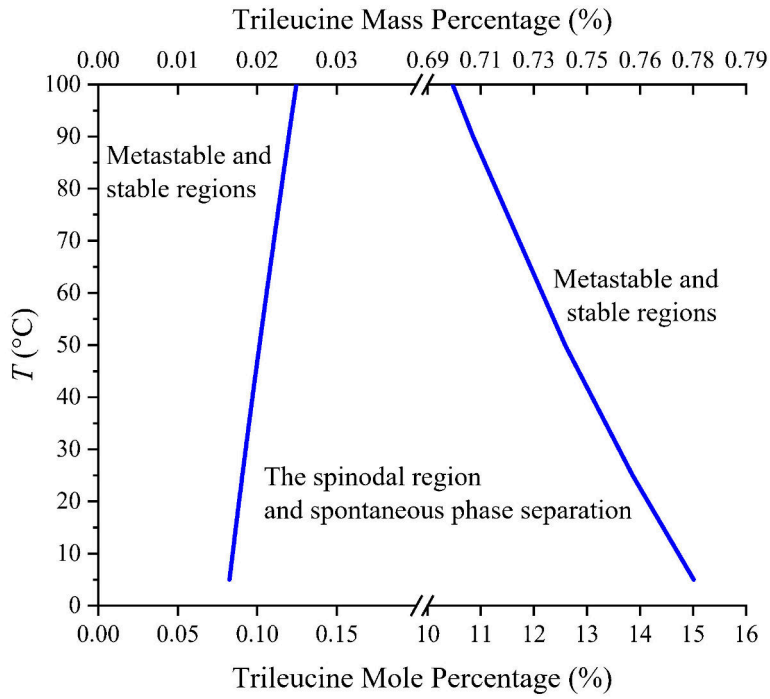

Figure 4.3: The Spinodal curve of the trileucine-water system obtained from the Flory-Huggins theory. A transition into the spinodal region will induce spontaneous liquid-liquid separation into water-rich and water-lean phases.

compared to the spinodal concentration, $C_{\mathrm{sp,Leu3}} = 18$ mg/mL. The subsurface concentration can either be calculated from the solution of Equation (4.5) or obtained by using a simplified method as follows. After reaching a saturated surface monolayer, $\Gamma(t) = \Gamma_{\max}$, and assuming the number of adsorbed molecules into the monolayer is small relative to the molecules in the bulk, the subsurface concentration of the ith component can be obtained from the steady-state surface enrichment value based on what is known as the "VFL" model [32, 33],

$$E_{\mathrm{s},i} = \frac{C_{\mathrm{s},i}}{C_{\mathrm{m},i}} \approx 1 + \frac{Pe_i}{5} + \frac{Pe_i^2}{100} - \frac{Pe_i^3}{4000} \quad \text{for } Pe_i = \frac{\kappa}{8D_i} < 20, \tag{4.8}$$

where $C_{\mathrm{s},i}$ and $C_{\mathrm{m},i}$ are the instantaneous subsurface and mean concentrations, respectively, excluding the number of adsorbed molecules in the monolayer. The mean concentration of component i can be obtained from

$$C_{\mathrm{m},i} = C_{0,i}(1-\tau)^{-3/2} - \frac{6\Gamma_{\max}}{d_0}(1-\tau)^{-1/2}, \tag{4.9}$$

where $C_{0,i}$ is the initial feed concentration of this component and $\tau = t/t_{\mathrm{d}}$ is the dimensionless time, while $t_{\mathrm{d}} = d_0^2/\kappa$ is the drying time of the droplet and d_0 is the initial droplet diameter. In Equation (4.9), the second term on the right was added to account for the amount of material adsorbed onto the interface and is negligible for non-surface-active molecules. It is important to note that Equations (4.8) and (4.9) give reasonable results only after some time has passed, since the monolayer has been saturated. Assuming the $\frac{6\Gamma_{\max}}{d_0}$ term is negligible, the dimensionless time at which spinodal decomposition commences for the ith component can be obtained from the combination of Equations (4.8) and (4.9) as

$$\tau_{\mathrm{sp},i} = t_{\mathrm{sp},i}/t_{\mathrm{d}} = 1 - \left(\frac{C_{0,i}E_{\mathrm{s},i}}{C_{\mathrm{sp},i}}\right)^{\frac{2}{3}} \tag{4.10}$$

Where the assumption in arriving at Equation (4.10) does not hold, for example, in cases of small initial droplets or droplets with low initial solute concentrations, Equation (4.5) should be solved numerically to find the respective time for the initiation of phase separation. During formulation design, Equation (4.10) can be compared to similar timescales such as time to reach saturation for crystallizing components or time to reach true density for highly soluble amorphous components in order to better predict the particle formation processes, if relevant, for other competing components present in the system [14].

4.3 Results and Discussions

4.3.1 Single-Particle Measurements Using the CK-EDB Instrument

The time of shell formation and solidification, as well as the instantaneous morphology of the droplets containing trileucine and trehalose, was estimated using the CK-EDB instrument. The evaporation histories of one sample droplet for

each case are shown in Figure 4.4. The approximate instantaneous particle morphologies are also color-coded, with blue representing optically spherical and homogenous, black representing spherical but with internal inclusions, red representing a core-shell morphology, and purple representing non-spherical. The measurement of the diameter is reliable as long as the particle maintains optical homogeneity (blue); the size estimated when the particle is non-spherical and optically inhomogeneous should not be considered accurate. For both the aqueous-trileucine and aqueous-trileucine-trehalose solution droplets, the linear portion of the d^2 vs time plots (the constant evaporation rate period) decreases with an increase in trileucine content, pointing to earlier shell formation that occurs at larger particle diameters. For all cases, the droplets were initially spherical during the constant-rate evaporation period, with a transition to non-spherical particles. For lower trileucine concentrations, this transition regime was rather sharp and sudden; with an increase of trileucine content, the transition was more gradual, with the appearance of a mixture of core-shell and spherical-with-inclusion morphologies before the final phase change. In such cases, the phase-separated domains were likely large enough to be discernible by light scattering and detected by the algorithm used for morphology detection. The core-shell morphology points to the preferential phase-separation on the droplet surface, while the appearance of individual domains (inclusions) inside the droplets might be due to additional spinodal decomposition inside the evaporating droplet.

The quantification of the data obtained from the single-particle experiments was achieved by the determination of the time and diameter at which the evaporation rates were no longer constant and a deviation from the d^2-law was observed [33]. Henceforth, this instance will be called the critical point of shell formation or solidification, denoted by the subscript c and corresponding to the approximate time at which a sufficiently thick or viscous shell forms to hinder the evaporation of the remaining water in the droplets. The normalized critical diameters, d_c/d_0, and critical times, $\tau_c = t_c/t_d$, of the trileucine and trileucine/trehalose particles are shown in Figure 4.5. These data are shown versus both the initial trileucine concentration, $C_{0,\mathrm{Leu3}}$, and the respec-

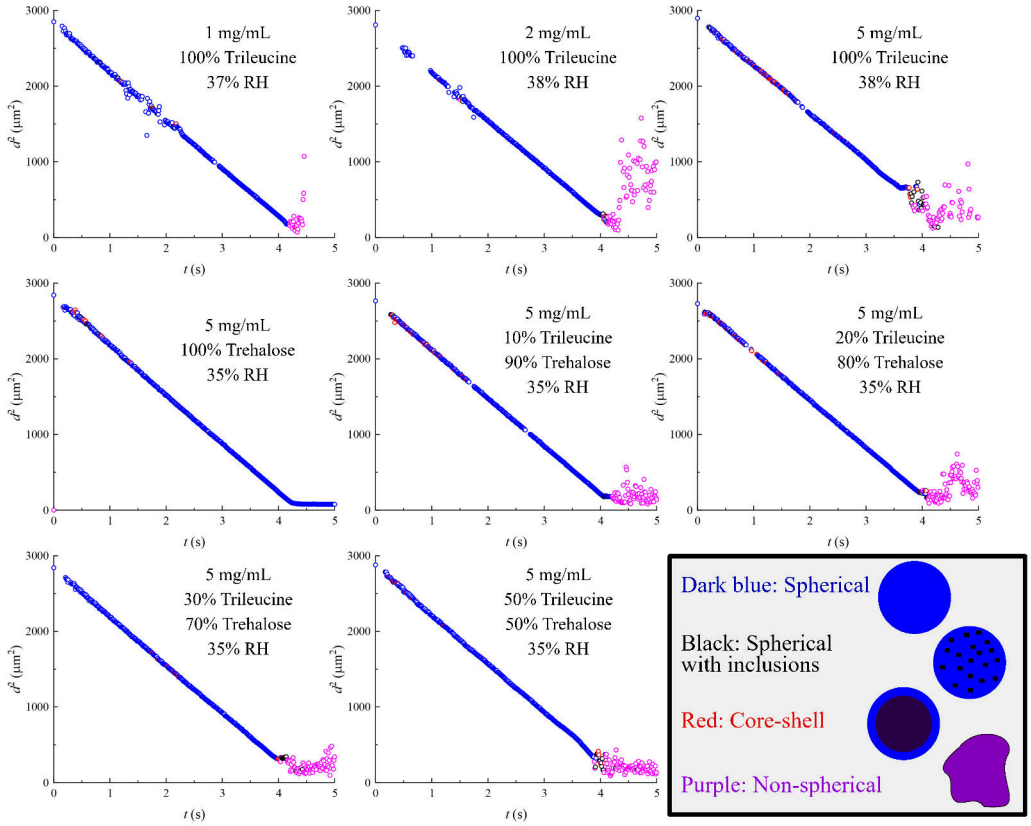

Figure 4.4: Sample evaporation histories of the formulations studied with the CK-EDB instrument. The drying temperature was 20 °C for all cases. The data points are color-coded with the approximated morphologies as explained at the bottom right. The measured sizes are reliable only for optically spherical particles (blue).

tive initial trileucine saturation, $S_{0,\mathrm{Leu3}}$, multiplied by the steady-state surface enrichment of trileucine, E_s. The steady-state surface enrichment, which is a function of the Péclet number, accounts for the amount of material accumulating on the droplet surface due to the recession of the droplet surface alone [14, 33]. The advantage of such representation of the trileucine content will be explained later. For both the trileucine and the trileucine/trehalose cases, the critical diameter increased and the critical time decreased with an increase to trileucine content, resulting in particles with lower densities. This observation supports the hypothesis that the precipitation and the subsequent shell formation of trileucine are initiated upon achieving a certain critical concentration that leads to spinodal decomposition. It is also evident that the neat trileucine

systems reached the critical shell formation state at a slightly later stage and at smaller diameters compared to the trileucine/trehalose systems, perhaps because of the higher total concentration and viscosity in the latter systems. The minor difference between the trileucine and the trileucine/trehalose systems means that trehalose does not interfere considerably with the phase separation and shell formation of trileucine. This justifies the use of a binary phase diagram for water and trileucine in the presence of trehalose. A non-linear fit to the normalized time of shell formation of trileucine gives

$$\tau_{\mathrm{c,Leu3}} = t_{\mathrm{c,Leu3}}/t_{\mathrm{d}} = 1 - 0.24\left(E_{\mathrm{s}}S_{0,\mathrm{Leu3}}\right)^{2/3}, \tag{4.11}$$

where, as stated before, E_{s} is the steady-state surface enrichment obtained from Equation (4.8) and $S_{0,\mathrm{Leu3}}$ is the initial trileucine saturation. This equation resembles the relationships obtained from the mass balance consideration inside the droplet for other thresholds, such as the time to reach saturation and the time to reach the true density of a component [14], and can be used to predict the approximate time of shell formation of trileucine. The data used in arriving at Equation (4.11) were obtained for relatively large droplets ($d_0 \cong 50$ µm), and their accuracy for smaller atomized droplets, such as those encountered in spray drying of inhalable particles, cannot be verified directly. Nevertheless, the size dependency of the time for shell formation is expected to be more considerable for crystallizing systems that need to overcome an energy barrier and undergo nucleation and crystal growth [122]. Spinodal decomposition is expected to be faster and hence the use of Equation (4.11) for smaller droplet sizes appears reasonable.

The normalized time for trileucine to reach a concentration of $C_{\mathrm{sp,Leu3}} = 18$ mg/mL at the subsurface domain was predicted using Equation (4.10) and is shown as the grey line in Figure 4.5. Similar results were obtained via the numerical solution of Equation (4.5) because for the large droplets encountered in the EDB experiments, the monolayer formation happened much earlier relative to the droplet lifetime (this will be discussed later). As expected, the subsurface concentration reached the predicted spinodal point earlier than the

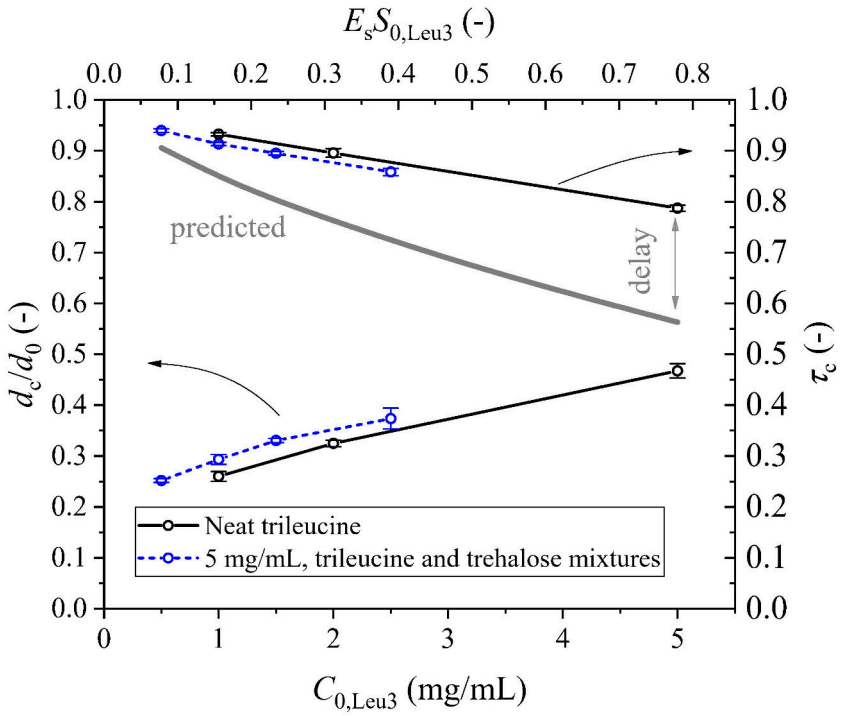

Figure 4.5: The normalized critical diameters (bottom curves) and times of shell formation and solidification (top curves) for the trileucine and trileucine/trehalose systems obtained from the deviation from the d^2-law in the CK-EDB measurements versus the initial trileucine concentration at the bottom and the initial trileucine saturation multiplied by the steady-state surface enrichment at the top. The error bars represent one standard deviation of the multiple droplets studied per case. The drying temperature was 20 °C for all cases. The initial droplet diameters were approximately 50 µm. The grey line is the predicted time for spinodal decomposition to commence obtained from Equation (4.10).

critical shell formation time measured via the single-particle measurements. Upon reaching the spinodal point, the trileucine molecules in the bulk separate into a water-rich phase and a water-lean phase quickly, most likely near the surface. The water-lean domains accumulated near the surface are expected to undergo further water loss due to the continuing evaporation, until the viscosity of the glassy phase is large enough for a shell to form and fold upon further shrinkage and evaporation.

After a while, the instrument detected a drop in evaporation rates and different morphologies. This time delay between $\tau_{sp,Leu3}$ and τ_c is shown as the area between the measured and predicted curves in Figure 4.5. The delay

increased with an increase in initial trileucine content, likely because phase separation happened at a larger droplet diameter at higher trileucine contents, and it takes more time to make a viscous shell that can arrest droplet shrinkage on the larger droplets.

To also investigate the precipitation behavior of the system, the bulk concentration of trileucine at the critical shell formation, $C_{c,Leu3}$, obtained from a simple mass balance equation and the measured d_c [122], versus the initial trileucine concentration, $C_{0,Leu3}$, is shown in Figure 4.6. In all cases, the bulk critical concentration was measured to be larger than the previously calculated spinodal point of trileucine in water ($\sim$ 18 mg/mL). This also agrees with our assumption of spinodal decomposition of trileucine during drying and the ensuing delay time as discussed above.

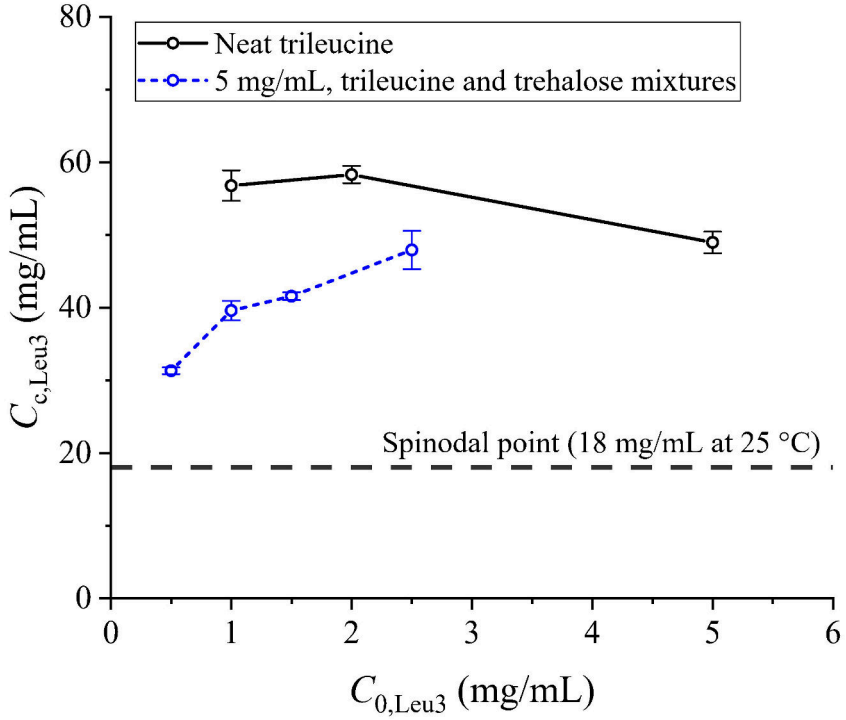

Figure 4.6: The apparent bulk concentration of trileucine at the critical time of shell formation obtained from the CK-EDB measurements. The drying temperature was 20 °C for all cases. The initial droplet diameters were approximately 50 µm. Here, the bulk concentration is obtained from the total amount of trileucine in the droplet divided by the droplet diameter at shell formation; hence it includes the amount of material adsorbed onto the surface too.

For the neat trileucine systems, $C_{c,Leu3}$ is slightly lower at higher trileucine concentrations. This agrees with the previous observations because for the cases of neat trileucine a higher $C_{0,Leu3}$ means reaching the spinodal point earlier and at a larger droplet diameter and hence at a smaller bulk concentration. This behavior is reversed for the trileucine/trehalose systems, whose critical bulk concentrations are always lower at similar neat trileucine feed concentrations. This difference could be explained by the possible coprecipitation of trileucine and trehalose. For a leucine/trehalose system, such a trend was not observed due to the independent crystallization and shell formation of leucine [122]. To further assess the validity of this hypothesis of coprecipitation of trileucine and trehalose, the surface concentration of trehalose at the time that trileucine reached its spinodal point was estimated using the VFL method. This showed a decrease from around 160 mg/mL to 20 mg/mL when the trileucine fraction was increased from 10% to 50% while the total feed concentration was kept constant at 5 mg/mL. These values were larger than the spinodal concentration of trileucine ($\sim$ 18 mg/mL). Hence, it could be expected that both of the phase-separated domains had some trehalose content, with the water-rich phases possibly having a higher trehalose content than the trileucine-rich phases. The ability of trileucine to coprecipitate with other components, along with its high glass transition temperature, $\sim$ 104 °C [29], might be contributing to its superior performance in stabilizing biologics [124, 125].

The critical bulk concentration of trehalose, $C_{c,treh}$, obtained from neat trehalose droplets was previously measured and was also confirmed from the data in Figure 4.4 to be around 830 ± 15 mg/mL [122]. This result indicates that trehalose by itself is expected to undergo a rapid rise in viscosity and glass formation upon reaching this bulk concentration.

4.3.2 Monodisperse Particles from the Droplet Chain Instrument

The SEM micrographs of monodisperse particles generated using the droplet chain instrument are shown in Figure 4.7. As mentioned earlier, the formu-

lations studied using the droplet chain instrument (seen in Table 4.2) were chosen to represent the systems measured via the CK-EDB instrument for which the final dried particles cannot be collected. Two different magnifications are provided for each sample to study both the micro- and nano-scale morphologies of the particles. In agreement with the observations from the CK-EDB, the particles were bigger and less dense at higher trileucine feed concentrations for both the trileucine and the trileucine/trehalose systems. A folded shell can be observed for all particles that contain trileucine, which is evidence of the presence of a pliable skin that can wrinkle and fold and eventually dry into a shell. The nanostructure at the surfaces of the trileucine particles was smooth, possibly due to the monolayer formation at the droplet interface and the absence of any crystals. It can also be observed that the inside of the particles is visible due to the presence of a hole for all three trileucine cases and the last case of the trileucine/trehalose systems with the highest trileucine fraction. These holes are possibly caused by the rupture of the thin-shelled particles during drying. As seen in the ultra-magnified micrographs, the morphology of the interior of these particles is completely different from the surface morphology.

The measured normalized particle diameters, d_{p}/d_0, are shown in Figure 4.8. At similar compositions, the normalized diameters of the dried particles are slightly smaller than the normalized critical diameters of shell formation obtained from the CK-EDB instrument (refer to Figure 4.5). This is because after shell formation the particles can still lose their water content and shrink, but at a slower rate. The gradual increase of the particle diameters with an increase in trileucine content is also visible. The particle densities, ρ_{p}, also shown in Figure 4.8, were obtained from the equation for the mass balance of the involatile components as [14]:

$$\rho_{\mathrm{p}} = C_{0,\mathrm{t}} \left(d_0/d_{\mathrm{p}}\right)^3, \tag{4.12}$$

where $C_{0,\mathrm{t}}$ is the total feed concentration. The particle density obtained from this equation gives an envelope density for which the internal and ex-

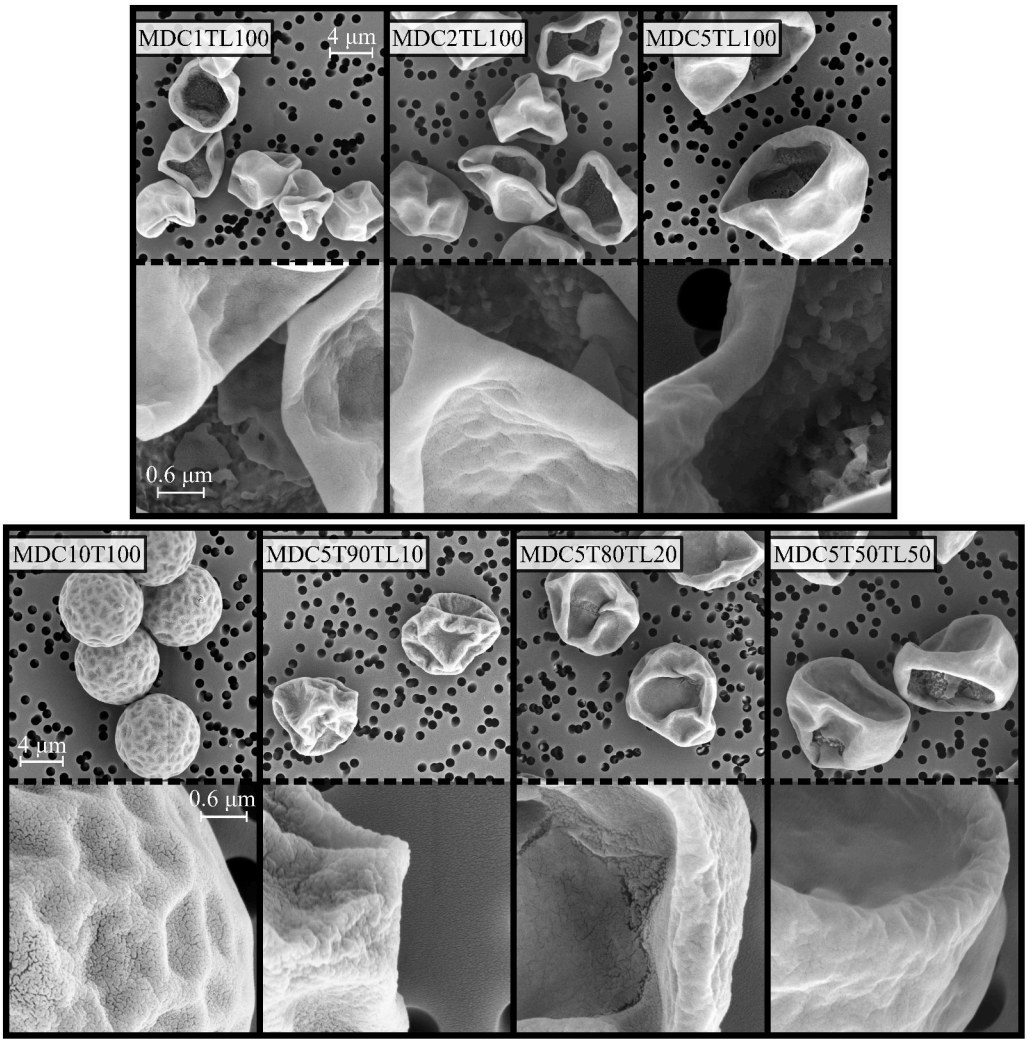

Figure 4.7: The micrographs of the monodisperse particles collected from the droplet chain instrument at two different magnifications. The drying temperature was 20 °C for all cases. Each scale bar applies to its respective row. The initial droplet diameters were approximately 40 µm.

ternal voids are also considered in the volume. The inclusion of only 10% trileucine (0.5 mg/mL) decreased the particle density to about 500 mg/mL, while the density of neat trehalose particles is measured to be larger than 1500 mg/mL from the MDC10T100 system. The particle densities decreased further with an increase to the trileucine content. Moreover, the particle densities of trileucine/trehalose systems were larger than those of neat trileucine cases at the same conditions. An increasing amount of void space is opened up as the trileucine content is increased, creating the potential to produce particles

with very low density. Elsewhere, it has been shown that at very small concentrations, trileucine does not change the morphology of trehalose-containing particles, while the particles' dispersibility already increases due to the adsorbed surface monolayer [88]. These observations show that this system is suitable for both high- and low-density particle design targets with superior aerosol performance.

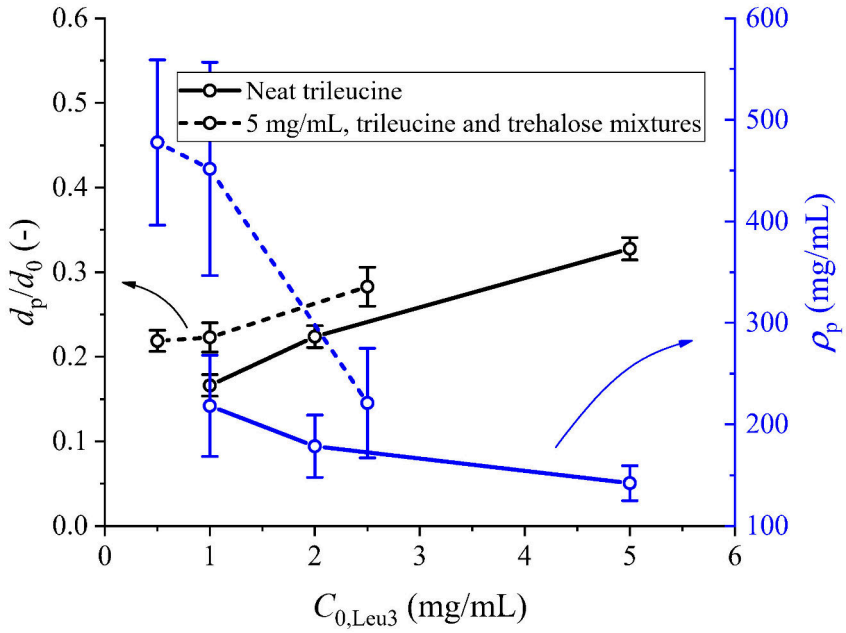

Figure 4.8: The normalized particle diameters (shown in black) and the particle densities (shown in blue) obtained from the monodisperse droplet chain instrument. The error bars represent one standard deviation. The drying temperature was 20 °C for all cases and the initial droplet diameters were approximately 40 µm.

4.3.3 Spray-Dried Powders

The spray-dried powders were also studied in order to broaden the scope of analysis to include conditions representative of actual industrial settings, in particular the spatially varying parameters inside the spray plume, such as temperature, relative humidity, and the smaller initial sizes of the polydisperse atomized droplets. It was especially of interest to determine whether the findings obtained from the larger droplets at lower drying temperatures could be generalized to practical industrial conditions.

The micrographs of the spray-dried trileucine/trehalose particles are shown in Figure 4.9. As with the monodisperse particles, increasing the trileucine content caused the particles to become larger and less dense and to develop rugose surfaces. Compared to the trehalose particles, the addition of only 2% trileucine (1 mg/mL) caused considerable morphological differences due to early liquid-liquid phase separation.

Compared to the spray-dried leucine/trehalose particles, which had a variety of different particle morphologies for different particle sizes (or different initial droplet sizes) of the same batch [122], the trileucine/trehalose particles have similar general morphologies irrespective of their sizes. This difference in behavior is further evidence for the different phase separation behaviors of leucine (nucleation and crystal growth with an energy barrier) and trileucine (spinodal decomposition near the surface) during spray drying.

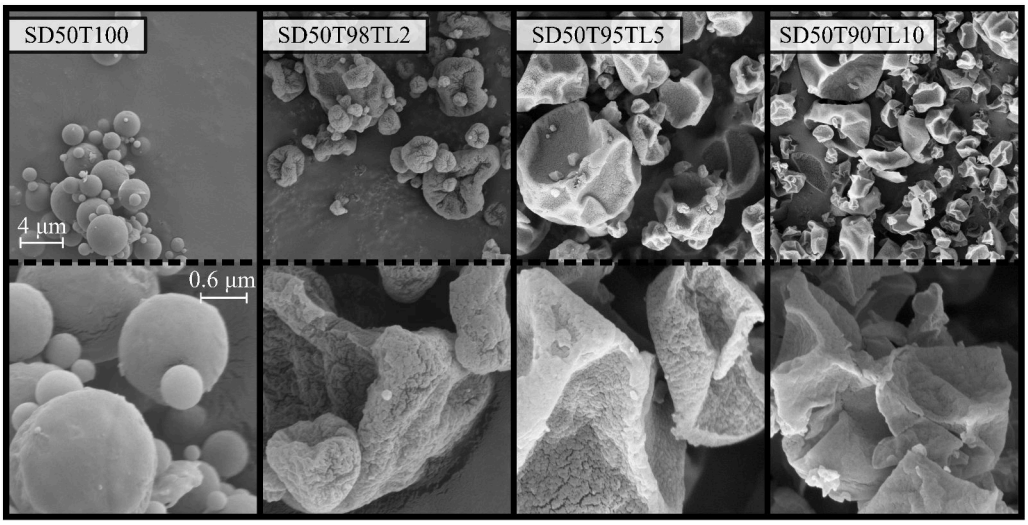

Figure 4.9: The micrographs of the spray-dried trileucine/trehalose particles at two different magnifications. The drying temperature was 75 °C for all cases. Each scale bar applies to its respective row.

Raman spectroscopy measurements (not shown) confirmed that both the trehalose and trileucine components were completely amorphous in all of the spray-dried batches [124, 125], refuting the possibility of early nucleation and crystal growth as the origins of trileucine shell formation.

The surface compositions of the spray-dried particles are shown in Fig-

ure 4.10. In these 8-bit RGB images obtained from the TOF-SIMS instrument, the blue and red channels were reserved for the signal strengths of trehalose and trileucine, respectively. The pixel-average surface compositions of the powders as a whole, small ($d < 1$ µm), medium ($1 < d < 3$ µm), and large particles ($d > 3$ µm) are shown in Figure 4.11. It is seen that the powders exhibit more trileucine on the surface at higher trileucine feed fractions. The surface coverage of trileucine increased from $\sim 70\%$ w/w to $\sim 92\%$ w/w through an increase to its feed fraction from 2% w/w to 10% w/w. It is observed that nearly complete surface enrichment of trileucine (nearly 40-fold compared to the bulk) is achieved by the addition of small quantities of this shell former. It is interesting to note that previous TOF-SIMS measurements of leucine/trehalose particles showed that the addition of different mass fractions of leucine ranging from 10 to 40% resulted in less than 3-fold surface enrichment compared to the bulk fractions [122]. Considering the probe depth of the TOF-SIMS instrument ($\sim 3-5$ nm), the extremely high surface coverage of trileucine is likely due to the presence of the saturated monolayer (the diameter of a trileucine molecule is about 0.9 nm) as well as the liquid-liquid phase separation due to spinodal decomposition with low trehalose content in the trileucine-rich phase.

As opposed to leucine/trehalose particles [122], the trileucine/trehalose particles are more similar across different particle sizes, pointing yet again to the different shell formation mechanisms of leucine and trileucine. It is observed that the particles with the smallest trileucine content (SD50T98TL2) had slightly different surface compositions for different particle sizes, with smaller particles having less trileucine on the surface than the larger particles. This behavior was not as discernible at higher trileucine fractions. The monolayer surface adsorption due to the trileucine surface activity is likely responsible for this difference in surface compositions as the thickness of the monolayer, $\sim$ 1 nm, comprises more than 20% of the probe depth of the TOF-SIMS instrument. This in turn means that a non-saturated monolayer ($\Gamma < \Gamma_{\max}$) on the smaller particles would affect the measured surface coverage slightly.

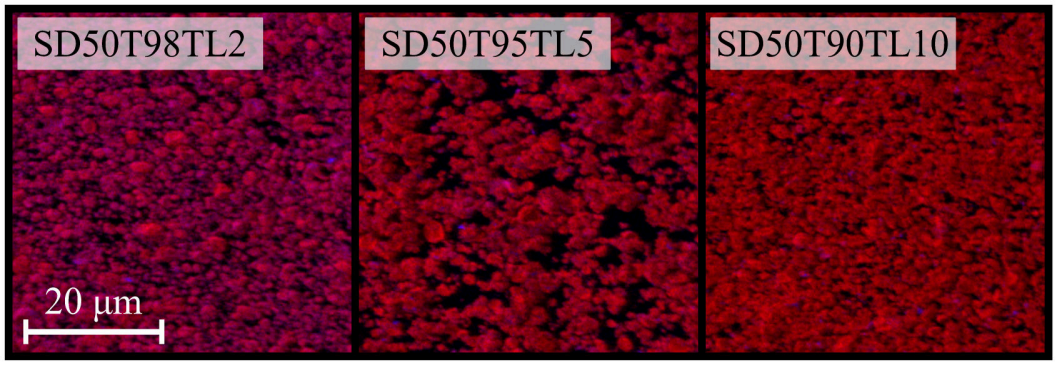

Figure 4.10: The TOF-SIMS 8-bit RGB images of the spray-dried trileucine and trehalose particles. The red and blue channels represent the trileucine and trehalose surface compositions, respectively. The drying temperature was 75 °C for all cases.

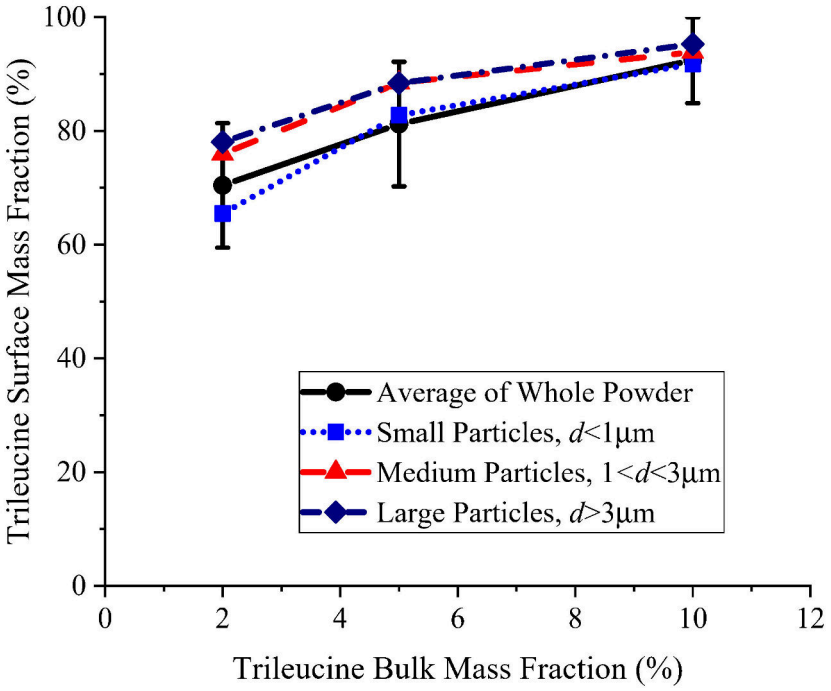

Figure 4.11: The pixel-average surface compositions of the whole powder, small, medium, and large spray-dried particles. The drying temperature was 75 °C for all cases. The error bars represent the standard deviation.

4.3.4 Implications for Formulation and Process Design via Particle Engineering for Surface-Active Materials

As discussed above, the surface adsorption of trileucine plays an important role in its higher surface enrichment in spray-dried particles. Hence, the kinetics of the monolayer formation should be studied in more depth for a successful particle design of systems containing at least one surface-active component.

The adsorption of surface-active materials on the droplet interface was previously approximated using Equation (4.4) [130], which was originally obtained for the adsorption of surfactants on the interface of a semi-infinite medium [133]. The use of this relationship does not account for the depletion of the solute molecules in small atomized droplets (due to the large surface-to-volume ratio of a small sphere), nor does it account for the effect of the receding droplet surface due to evaporation. To explain these effects, Equation (4.5) was solved in conjunction with the appropriate boundary conditions for trileucine at different initial droplet diameters, feed concentrations, and drying temperatures. The bulk concentration, subsurface concentration, and adsorbed surface excess of a sample case versus time are shown in Figure 4.12a. The initial droplet diameter was 8 µm, trileucine feed concentration was 1 mg/mL and the drying temperature was 75 °C, imitating the conditions of the SD50T98TL2 spray-dried case. Until a certain point in time, t_Γ, at which the maximum surface excess of 0.99 mg/m^2 was reached, the subsurface concentration was zero, while the bulk concentration decreased due to the surface adsorption. Upon reaching the maximum surface excess at t_Γ, the enforced boundary conditions were switched, and desorption from the interface into the subsurface commenced due to the decreasing surface area and the fact that the surface excess cannot be increased past the maximum value, Γ_{max}. Eventually, the subsurface concentration increased similarly to the ordinary particle formation predictions explained elsewhere [32, 95]. These behaviors can also be seen from the internal radial concentration distributions of the same droplet at different time points during the evaporation period shown in Figure 4.12b.

The time to reach the maximum surface excess, t_Γ, for different trileucine feed concentrations as a function of the initial droplet diameter obtained from the numerical simulations is shown in Figure 4.13 for drying temperatures of 20 °C and 75 °C. The times required to reach surface saturation obtained from Equation (4.4) (semi-infinite volume case) are also shown as the horizontal lines for each respective feed concentration; surprisingly, these are not identical for the same concentration at different temperatures. The reason is the lower aqueous viscosity at the higher wet-bulb temperature and hence the higher trileucine diffusion coefficient for the drying temperature of 75 °C compared to 20 °C.

Also shown in Figure 4.13 as grey dashed lines are the drying times, t_d, of the droplets with different diameters. The numerical results converge to those obtained from Equation (4.4) at larger initial droplet diameters, but the results deviate for smaller diameters and feed concentrations due to the shorter drying times of the small droplets. Considering only the horizontal lines obtained from Equation (4.4), any case that has an initial droplet diameter to the left of the intersection of the respective line and the t_d line would not have enough time to form a monolayer on the droplet surface. For example, the drying time of a droplet with an initial diameter of 2 µm and a trileucine concentration of 0.5 mg/mL dried at 75 °C is less than the time required to reach the maximum surface excess obtained from Equation (4.4). However, as seen from the full numerical results, the reality is different. Even though the droplet's lifetime is less than the time required for surface saturation obtained from the simple equation, there will still be a fully adsorbed monolayer near the end of the drying process due to droplet shrinkage. It is for this reason that in Figure 4.13 the numerical results are tangent to the t_d curves for smaller initial droplet diameters and for the cases with low trileucine concentrations.

It is also observed that at the lower drying temperature of 20 °C, the curves for the trileucine feed concentrations of 0.1, 0.5, and 1 mg/mL have local maxima above their respective horizontal lines. The longer times required for monolayer formation for these low-concentration cases are due to the depletion of the solute molecules in the bulk at smaller initial droplet diameters

(higher surface-to-volume ratio). At these conditions, the droplet shrinkage due to evaporation is not fast enough to maintain the bulk concentration while the solute material is being adsorbed onto the interface. At larger initial droplet diameters and smaller surface-to-volume ratios, the curves eventually converge with the horizontal lines. This behavior was not observed for the droplets evaporating at 75 °C, and the curves converged with the horizontal lines monotonically due to the fast evaporation of the droplets. Importantly, it can be concluded that for droplets typically encountered in industrial spray dryers (*i.e.* $d > 7$ µm) and typical drying gas conditions (the 75 °C plot), the time to form a saturated monolayer is very fast compared to the droplet lifetime, except in cases of very low initial trileucine concentrations.

In the presence of other excipients or actives another condition needs to be considered for particle design: for a saturated trileucine monolayer to form, the calculated t_Γ needs to be shorter than the shortest time of solidification of other components. Also, it can now be concluded that the shell formation and solidification of trileucine is a sequential process with monolayer formation being the first stage (at τ_Γ from Figure 4.13), followed by spinodal decomposition (at $\tau_{\mathrm{sp,Leu3}}$ from Equation (4.10)), and then the final period of the formation of a rigid shell on the surface of the droplet (at $\tau_{\mathrm{c,Leu3}}$ from Equation (4.11)). The critical solidification times of other components and active ingredients can now be compared to these values during formulation design. For the trileucine/trehalose platform studied in this article, the critical time of solidification for trehalose, $\tau_{\mathrm{c,Treh}}$, is assumed to be the time at which it reaches a bulk concentration of 830 mg/mL and is obtained from

$$\tau_{c,\mathrm{Treh}} = 1 - \left(\frac{C_{0,\mathrm{Treh}}}{830 \text{ mg/mL}} \right)^{2/3}, \tag{4.13}$$

in which $C_{0,\mathrm{Treh}}$ is the initial feed concentration of trehalose in mg/mL. For trehalose, the bulk concentration can be used as a threshold in particle formation, as its Péclet number is small enough to give a surface enrichment of close to 1 at these drying temperatures [122]. As an example, the time points of interest for three different trileucine/trehalose systems analogous to

the spray-dried formulations were calculated and are reported in Figure 4.14. It is observed that for all cases τ_Γ was much smaller than the solidification time of trehalose, $\tau_{c,Treh}$. But for the first system with 2% w/w trileucine, τ_Γ was relatively close in magnitude to $\tau_{c,Treh}$ for small initial droplet diameters. This difference increased for greater trileucine fractions. This fact is assumed to be one of the reasons for the relatively dissimilar surface compositions among different particle sizes of the SD50T98TL2 system as shown in Figure 4.10. In the first case with 2% w/w trileucine, $\tau_{sp,Leu3}$ was close to $\tau_{c,Treh}$ explaining possible solidification of trileucine and trehalose at similar times. In the systems with higher trileucine fractions in Figure 4.14, it is predicted that the spinodal decomposition of trileucine starts long before the solidification of trehalose.

Note that in the simplified discussion here, the liquid-liquid phase separation of the ternary system of trileucine and trehalose with water is not considered. Based on the plots shown in Figure 4.14, trileucine is expected to act as a strong dispersibility enhancer for all three systems, because a saturated monolayer could be formed on the droplet surface before other components could interfere with the surface adsorption. The presence of this monolayer is responsible for reducing the surface energy of the dried particles and in turn increasing the dispersion properties of the resulting powders. The increase of trileucine fractions from 2% w/w to 10% w/w is expected to cause a thicker trileucine shell on the surface that might not be necessary to maintain the dispersibility enhancement but that can greatly decrease the particle density if the goal of the design process is producing low-density particles.

Using a similar methodology, a formulator can design a system composed of many excipients and active ingredients. It should be noted here that multiple surface-active components in the same system are expected to interfere with each other's surface adsorption. In that case, the methodology proposed for the prediction of surface adsorption of the components in such systems would need to be modified.

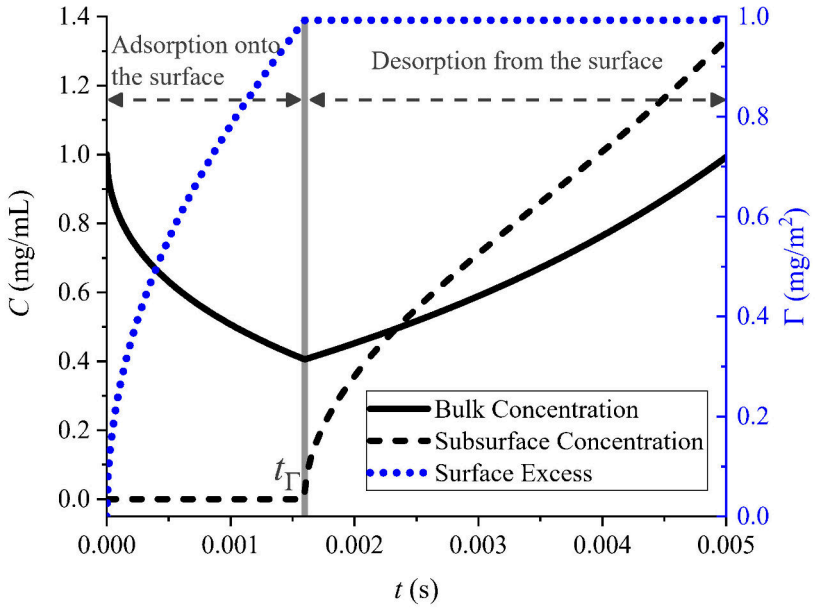

(a)

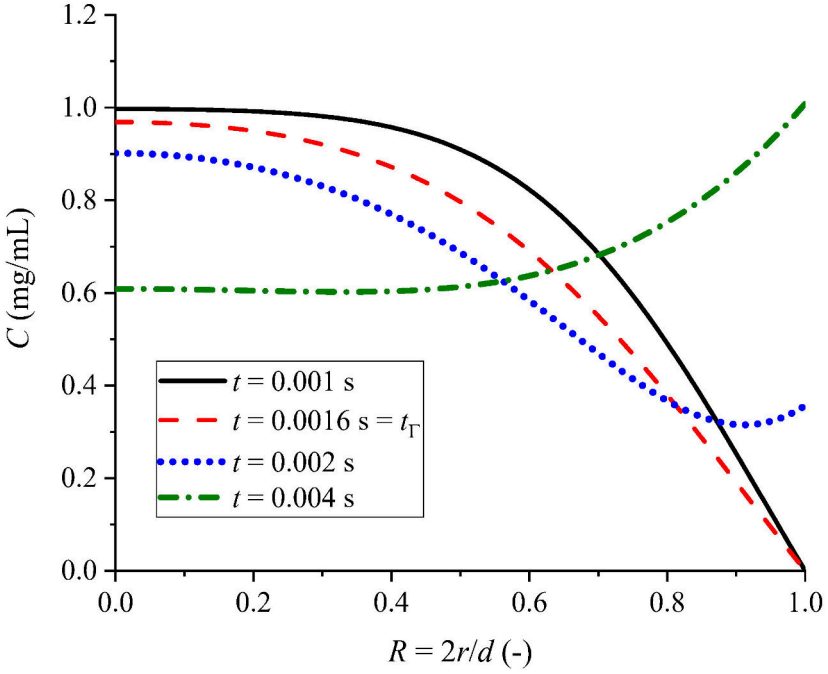

(b)

Figure 4.12: (a) The bulk and subsurface concentrations as well as the instantaneous surface excess of a water droplet containing 1 mg/mL trileucine, drying at 75 °C with an initial diameter of 8 µm. For this specific droplet, the drying time was calculated to be 0.014 s. (b) The internal concentration distribution at different times for the same droplet of (a) versus the normalized radial coordinate.

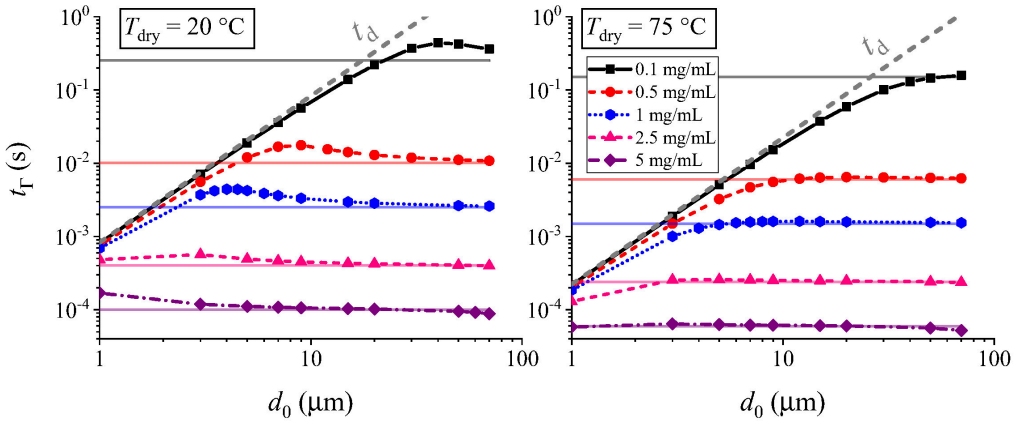

Figure 4.13: The calculated time required for trileucine monolayer formation for different trileucine feed concentrations and initial droplet diameters at two different drying temperatures. The curves were obtained from the solution of the diffusion equations inside an evaporating droplet. The horizontal asymptotic lines were obtained from Equation (4.4) and $t_d = d_0^2/\kappa$ is the droplet lifetime.

4.4 Conclusion

A methodology was proposed to implement the effect of surface activity into available particle formation models for the first time. Furthermore, the particle formation of trileucine, a surface-active molecule that does not crystallize during spray drying and has low aqueous solubility, was explained as a combination of the formation of an adsorbed monolayer on the droplet surface and liquid-liquid phase separation due to spinodal decomposition.

The formation of a fully saturated monolayer of trileucine on the droplet surface contributes to the significant improvement of aerosol properties. The highly wrinkled morphologies and low densities observed for systems containing trileucine as a dispersibility enhancer were also explained as having been caused by the early phase separation.

By following the methodology explained in this study and combining the information obtained from experimentation and theoretical discussions, a formulator can design a system with minimal experimental iterations with trileucine as a dispersibility enhancer in systems containing other excipients and active pharmaceutical ingredients.

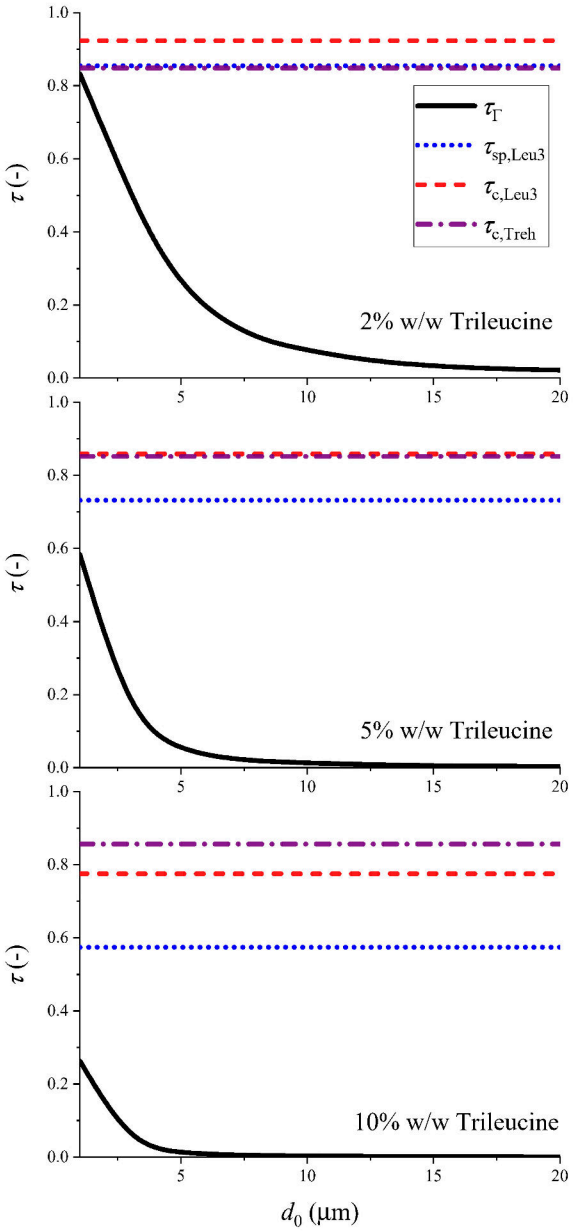

Figure 4.14: The different dimensionless timescales of three trileucine and trehalose systems with a total feed concentration of 50 mg/mL and varying fractions of trileucine. $\tau_\Gamma = t_\Gamma/t_d$ is the time required for the formation of a saturated trileucine monolayer on the surface of the droplets. $\tau_{sp,Leu3}$ is the approximate time when spinodal decomposition of trileucine is predicted to start. $t_{c,Leu3}$ is the predicted time for trileucine to make a rigid shell on the surface and $\tau_{c,Treh}$ is the approximate time at which trehalose is expected to solidify. The drying temperature was 75 °C for all cases.

Chapter 5

Conclusion

In this thesis, some of the lingering problems with particle formation models have been addressed, namely, the evaporation and internal solute diffusion of multi-solvent droplets, the particle formation of a low-soluble crystallizing shell former such as leucine, and finally, the particle formation of a strongly surface-active low-soluble shell former such as trileucine.

In Chapter 2, the drying kinetics of multi-solvent droplets containing some solutes were studied. It was shown that, depending on the solvent mixtures, azeotropic-like behavior can be observed in the evaporation of microdroplets. For these iso-compositional mixtures, the conventional particle formation models used for single-solvent systems can be employed. It was also determined that, given enough material can be dissolved in the feed, the particle formation of components that are not expected to crystallize is purely diffusion-controlled, and the particle morphology is similar at different co-solvent ratios. For molecules that do crystallize during drying, the change of solvent composition resulted in significant morphological variations in the resulting particles.

The particle formation of leucine during spray drying was studied in Chapter 3. It was determined that the surface enrichment of leucine-containing particles is mostly due to the nucleation and crystal growth of leucine molecules. Consequently, the surface morphology and solid phase of such particles were observed to be size-dependent. A theoretical supersaturation ratio at which nucleation is thought to be spontaneous was estimated for leucine. It was also confirmed that the presence of high fractions of a glass former, such as

trehalose, can hinder the nucleation and crystal growth of leucine, and hence hinder its ability to act as an efficient shell former. Based on these findings, a modified particle formation model was proposed to assist a formulator in the early stages of product development.

In Chapter 4 the phase separation of trileucine in evaporating microdroplets was studied in depth. It was concluded that the formation of a fully saturated trileucine layer on the droplet surface due to its surface activity improves the aerosol properties significantly. The wrinkled morphologies, another cause of dispersibility enhancement, were shown to be caused by early liquid-liquid phase separation in aqueous trileucine solutions. A model was also proposed to account for the surface adsorption of surface-active molecules during droplet evaporation. Such a modification improves the predictive capabilities of the particle formation models during the design of microparticles containing surfactants and shell formers.

Most of the theoretical understandings from the studies conducted in this thesis were obtained for a limited number of solvents, excipients, and active pharmaceutical ingredients. The capability of the proposed models in the prediction of physical properties of spray-dried particles encountered in a real-world situation demands further research. For example, the particle formation of a practical system comprising several crystallizing components, surface-active materials, or polymers could prove an interesting topic for future research, as could the use of the models and experimental methods employed in this thesis for the study of amorphous solid dispersions. Likewise, the use of the multi-solvent model in the simulation of simultaneous evaporation and condensation could be useful in a future study of the evaporation of pMDI propellant droplets in humid environments.

References

[1] Warren H. Finlay. *The Mechanics of Inhaled Pharmaceutical Aerosols: an Introduction*. 2nd edition. Elsevier, 2019.

[2] Stephen P. Newman. "Drug delivery to the lungs: challenges and opportunities." In: *Therapeutic Delivery* 8.8 (July 2017), pp. 647–661. ISSN: 2041-5990. DOI: 10.4155/tde-2017-0037.

[3] Ivana D'Angelo et al. "Improving the efficacy of inhaled drugs in cystic fibrosis: Challenges and emerging drug delivery strategies." In: *Advanced Drug Delivery Reviews* 75 (Aug. 2014), pp. 92–111. ISSN: 0169409X. DOI: 10.1016/j.addr.2014.05.008.

[4] N. R. Labiris and M. B. Dolovich. "Pulmonary drug delivery. Part I: Physiological factors affecting therapeutic effectiveness of aerosolized medications." In: *British Journal of Clinical Pharmacology* 56.6 (Dec. 2003), pp. 588–599. ISSN: 03065251. DOI: 10.1046/j.1365-2125.2003.01892.x.

[5] Chantal Darquenne. "Deposition Mechanisms." In: *Journal of Aerosol Medicine and Pulmonary Drug Delivery* 33.4 (Aug. 2020), pp. 181–185. ISSN: 1941-2711. DOI: 10.1089/jamp.2020.29029.cd.

[6] Ling Xu and Yi Jiang. "Mathematical Modeling of Mucociliary Clearance: A Mini-Review." In: *Cells* 8.7 (July 2019), p. 736. ISSN: 2073-4409. DOI: 10.3390/cells8070736.

[7] John S. Patton et al. "The Particle has Landed—Characterizing the Fate of Inhaled Pharmaceuticals." In: *Journal of Aerosol Medicine and Pulmonary Drug Delivery* 23.S2 (Dec. 2010), S–71–S–87. ISSN: 1941-2711. DOI: 10.1089/jamp.2010.0836.

[8] Elza Evren, Emma Ringqvist, and Tim Willinger. "Origin and ontogeny of lung macrophages: from mice to humans." In: *Immunology* 160.2 (June 2020), pp. 126–138. ISSN: 0019-2805. DOI: 10.1111/imm.13154.

[9] Charleston Ribeiro Pinto et al. "Local adverse effects associated with the use of inhaled corticosteroids in patients with moderate or severe asthma." In: *Jornal Brasileiro de Pneumologia* 39.4 (June 2013), pp. 409–417. ISSN: 1806-3713. DOI: 10.1590/S1806-37132013000400003.

[10] Ali Dabbagh et al. "Critical Parameters for Particle-Based Pulmonary Delivery of Chemotherapeutics." In: *Journal of Aerosol Medicine and Pulmonary Drug Delivery* 31.3 (June 2018), pp. 139–154. ISSN: 1941-2711. DOI: 10.1089/jamp.2017.1382.

[11] William C Hinds. *Aerosol Technology : Properties, Behavior, and Measurement of Airborne Particles*. Somerset: John Wiley & Sons, Incorporated, 1999. ISBN: 9781118591970.

[12] Bernice Mei Jin Tan, Lai Wah Chan, and Paul Wan Sia Heng. "Milling and Blending: Producing the Right Particles and Blend Characteristics for Dry Powder Inhalation." In: *Pharmaceutical Inhalation Aerosol Technology*. Ed. by Anthony J. Hickey and Sandro R.P. da Rocha. third edition. Boca Raton, Florida: CRC Press, 2019, pp. 273–289.

[13] Mehnaz Mursalat et al. "Microspheres with Diverse Material Compositions Can be Prepared by Mechanical Milling." In: *Advanced Engineering Materials* 22.3 (Mar. 2020), p. 1901204. ISSN: 1438-1656. DOI: 10.1002/adem.201901204.

[14] Reinhard Vehring. "Pharmaceutical Particle Engineering via Spray Drying." In: *Pharmaceutical Research* 25.5 (May 2008), pp. 999–1022. ISSN: 0724-8741. DOI: 10.1007/s11095-007-9475-1.

[15] Nicholas Carrigy and Reinhard Vehring. "Engineering Stable Spray-Dried Biologic Powder for Inhalation." In: *Pharmaceutical Inhalation Aerosol Technology*. Ed. by Anthony J. Hickey and Sandro R. da Rocha. third edition. Boca Raton, Florida: CRC Press, 2019, pp. 291–236.

[16] Ahmad Ziaee et al. "Spray drying of pharmaceuticals and biopharmaceuticals: Critical parameters and experimental process optimization approaches." In: *European Journal of Pharmaceutical Sciences* 127 (Jan. 2019), pp. 300–318. ISSN: 09280987. DOI: 10.1016/j.ejps.2018.10.026.

[17] Barry Long, Kevin M. Ryan, and Luis Padrela. "From batch to continuous — New opportunities for supercritical CO2 technology in pharmaceutical manufacturing." In: *European Journal of Pharmaceutical Sciences* 137 (Sept. 2019), p. 104971. ISSN: 09280987. DOI: 10.1016/j.ejps.2019.104971.

[18] Ranjith Kumar Kankala et al. "Supercritical Fluid Technology: An Emphasis on Drug Delivery and Related Biomedical Applications." In: *Advanced Healthcare Materials* 6.16 (Aug. 2017), p. 1700433. ISSN: 21922640. DOI: 10.1002/adhm.201700433.

[19] Sandro R.P. da Rocha et al. "Pressurized Metered-Dose Inhalers." In: *Pharmaceutical Inhalation Aerosol Technology*. Ed. by Anthony J. Hickey and Sandro R.P. da Rocha. third edition. Boca Raton, Florida: CRC Press, 2019, pp. 273–289.

[20] Reinhard Vehring et al. "Cosuspensions of Microcrystals and Engineered Microparticles for Uniform and Efficient Delivery of Respiratory Therapeutics from Pressurized Metered Dose Inhalers." In: *Langmuir* 28.42 (Oct. 2012), pp. 15015–15023. ISSN: 0743-7463. DOI: 10.1021/la302281n.

[21] James W Ivey, Reinhard Vehring, and Warren H Finlay. "Understanding pressurized metered dose inhaler performance." In: *Expert Opinion on Drug Delivery* 12.6 (June 2015), pp. 901–916. ISSN: 1742-5247. DOI: 10.1517/17425247.2015.984683.

[22] A. H. de Boer et al. "Dry powder inhalation: past, present and future." In: *Expert Opinion on Drug Delivery* 14.4 (Apr. 2017), pp. 499–512. ISSN: 1742-5247. DOI: 10.1080/17425247.2016.1224846.

[23] John N. Pritchard, Dirk von Hollen, and Ross H.M. Hatley. "Nebulizers." In: *Pharmaceutical Inhalation Aerosol Technology.* Ed. by Anthony J. Hickey and Sandro R.P. da Rocha. third edition. Boca Raton, Florida: CRC Press, 2019, pp. 273–289.

[24] Stefan Leiner et al. "Soft Mist Inhalers." In: *Pharmaceutical Inhalation Aerosol Technology.* Ed. by Anthony J. Hickey and Sandro R.P. da Rocha. third edition. Boca Raton, Florida: CRC Press, 2019, pp. 273–289.

[25] Alaa Hamed Salama. "Spray drying as an advantageous strategy for enhancing pharmaceuticals bioavailability." In: *Drug Delivery and Translational Research* 10.1 (Feb. 2020), pp. 1–12. ISSN: 2190-393X. DOI: 10.1007/s13346-019-00648-9.

[26] Cordin Arpagaus et al. "Nano spray drying for encapsulation of pharmaceuticals." In: *International Journal of Pharmaceutics* 546.1-2 (July 2018), pp. 194–214. ISSN: 03785173. DOI: 10.1016/j.ijpharm.2018.05.037.

[27] Reinhard Vehring. "Mechanistic Understanding of Microparticle Formation in Respiratory Applications." In: *Respiratory Drug Delivery.* 2018.

[28] David Lechuga-Ballesteros, Susan Hoe, and Benjamin W. Maynor. "Particle Engineering Technology for Inhaled Therapies." In: *Pharmaceutical Inhalation Aerosol Technology.* Ed. by Anthony J. Hickey and Sandro R.P. da Rocha. third edition. Boca Raton, Florida: CRC Press, 2019, pp. 349–361. DOI: 10.1201/9780429055201.

[29] David Lechuga-Ballesteros et al. "Trileucine Improves Aerosol Performance and Stability of Spray-Dried Powders for Inhalation." In: *Journal of Pharmaceutical Sciences* 97.1 (Jan. 2008), pp. 287–302. ISSN: 00223549. DOI: 10.1002/jps.21078.

[30] Liang Li et al. "l -Leucine as an excipient against moisture on in vitro aerosolization performances of highly hygroscopic spray-dried powders." In: *European Journal of Pharmaceutics and Biopharmaceutics* 102 (May 2016), pp. 132–141. ISSN: 09396411. DOI: 10.1016/j.ejpb.2016.02.010.

[31] A.L. Feng et al. "Mechanistic models facilitate efficient development of leucine containing microparticles for pulmonary drug delivery." In: *International Journal of Pharmaceutics* 409.1-2 (May 2011), pp. 156–163. ISSN: 03785173. DOI: 10.1016/j.ijpharm.2011.02.049.

[32] Reinhard Vehring, Willard R. Foss, and David Lechuga-Ballesteros. "Particle formation in spray drying." In: *Journal of Aerosol Science* 38.7 (2007), pp. 728–746. ISSN: 00218502. DOI: 10.1016/j.jaerosci.2007.04.005.

[33] Mohammed A. Boraey and Reinhard Vehring. "Diffusion controlled formation of microparticles." In: *Journal of Aerosol Science* 67 (Jan. 2014), pp. 131–143. ISSN: 00218502. DOI: 10.1016/j.jaerosci.2013.10.002.

[34] Mark Davis and Gavin Walker. "Recent strategies in spray drying for the enhanced bioavailability of poorly water-soluble drugs." In: *Journal of Controlled Release* 269 (Jan. 2018), pp. 110–127. ISSN: 0168-3659. DOI: 10.1016/J.JCONREL.2017.11.005.

[35] Xiangyu Ma and Robert O. Williams. "Characterization of amorphous solid dispersions: An update." In: *Journal of Drug Delivery Science and Technology* 50 (Apr. 2019), pp. 113–124. ISSN: 17732247. DOI: 10.1016/j.jddst.2019.01.017.

[36] Abhishek Singh and Guy Van den Mooter. "Spray drying formulation of amorphous solid dispersions." In: *Advanced Drug Delivery Reviews* 100 (May 2016), pp. 27–50. ISSN: 0169409X. DOI: 10.1016/j.addr.2015.12.010.

[37] Mohammed A. Boraey et al. "Improvement of the dispersibility of spray-dried budesonide powders using leucine in an ethanol–water co-solvent system." In: *Powder Technology* 236 (Feb. 2013), pp. 171–178. ISSN: 00325910. DOI: 10.1016/j.powtec.2012.02.047.

[38] Adrian Dobrowolski et al. "Preparation of submicron drug particles via spray drying from organic solvents." In: *International Journal of Pharmaceutics* 567 (Aug. 2019), p. 118501. ISSN: 03785173. DOI: 10.1016/j.ijpharm.2019.118501.

[39] Allen E. Haddrell et al. "Dynamics of aerosol size during inhalation: Hygroscopic growth of commercial nebulizer formulations." In: *International Journal of Pharmaceutics* 463.1 (Mar. 2014), pp. 50–61. ISSN: 0378-5173. DOI: 10.1016/J.IJPHARM.2013.12.048.

[40] Grazia Rovelli et al. "Accurate Measurements of Aerosol Hygroscopic Growth over a Wide Range in Relative Humidity." In: *The Journal of Physical Chemistry A* 120.25 (June 2016), pp. 4376–4388. ISSN: 1089-5639. DOI: 10.1021/acs.jpca.6b04194.

[41] Benan Cai et al. "Modeling of spray flash evaporation based on droplet analysis." In: *Applied Thermal Engineering* 130 (Feb. 2018), pp. 1044–1051. ISSN: 13594311. DOI: 10.1016/j.applthermaleng.2017.11.083.

[42] M.Q. Brewster. "Evaporation and condensation of water mist/cloud droplets with thermal radiation." In: *International Journal of Heat and Mass Transfer* 88 (Sept. 2015), pp. 695–712. ISSN: 00179310. DOI: 10.1016/j.ijheatmasstransfer.2015.03.055.

[43] Sergei S. Sazhin. "Modelling of fuel droplet heating and evaporation: Recent results and unsolved problems." In: *Fuel* 196 (May 2017), pp. 69–101. ISSN: 0016-2361. DOI: 10.1016/J.FUEL.2017.01.048.

[44] Eleftheria Chalvatzaki and Mihalis Lazaridis. "A dosimetry model of hygroscopic particle growth in the human respiratory tract." In: *Air Quality, Atmosphere & Health* 11.4 (May 2018), pp. 471–482. ISSN: 1873-9318. DOI: 10.1007/s11869-018-0555-7.

[45] Ari Kauppinen et al. "Efficient production of solid dispersions by spray drying solutions of high solid content using a 3-fluid nozzle." In: *European Journal of Pharmaceutics and Biopharmaceutics* 123 (Feb. 2018), pp. 50–58. ISSN: 0939-6411. DOI: 10.1016/J.EJPB.2017.11.009.

[46] James W. Ivey et al. "Humidity affects the morphology of particles emitted from beclomethasone dipropionate pressurized metered dose inhalers." In: *International Journal of Pharmaceutics* 520.1-2 (Mar. 2017), pp. 207–215. ISSN: 03785173. DOI: 10.1016/j.ijpharm.2017.01.062.

[47] Niels Grasmeijer, Henderik W. Frijlink, and Wouter L.J. Hinrichs. "Model to predict inhomogeneous protein–sugar distribution in powders prepared by spray drying." In: *Journal of Aerosol Science* 101 (Nov. 2016), pp. 22–33. ISSN: 00218502. DOI: 10.1016/j.jaerosci.2016.07.012.

[48] J. F. Widmann and E. J. Davis. "Evaporation of multicomponent droplets." In: *Aerosol Science and Technology* 27.2 (1997), pp. 243–254. ISSN: 15217388. DOI: 10.1080/02786829708965470.

[49] Giandomenico Lupo and Christophe Duwig. "A Numerical Study of Ethanol–Water Droplet Evaporation." In: *Journal of Engineering for Gas Turbines and Power* 140.2 (Oct. 2017), p. 021401. ISSN: 0742-4795. DOI: 10.1115/1.4037753.

[50] S. Tonini and G.E. Cossali. "A novel formulation of multi-component drop evaporation models for spray applications." In: *International Journal of Thermal Sciences* 89 (Mar. 2015), pp. 245–253. ISSN: 1290-0729. DOI: 10.1016/J.IJTHERMALSCI.2014.10.016.

[51] S. Tonini and G.E. Cossali. "A multi-component drop evaporation model based on analytical solution of Stefan–Maxwell equations." In: *International Journal of Heat and Mass Transfer* 92 (Jan. 2016), pp. 184–189. ISSN: 00179310. DOI: 10.1016/j.ijheatmasstransfer.2015.08.014.

[52] A. E. Kuchma, A. K. Shchekin, and D. S. Martyukova. "The Stefan outflow in a multicomponent vapor–gas atmosphere around a droplet and its role for cloud expansion." In: *Journal of Aerosol Science* 102 (2016), pp. 72–82. ISSN: 18791964. DOI: 10.1016/j.jaerosci.2016.08.014. arXiv: 1606.02086.

[53] N. A. Fuchs. *Evaporation and droplet growth in gaseous media*. Oxford: The Pergamon Press, 1959. ISBN: 1483225631.

[54] Tristan P. Learoyd et al. "Modified release of beclometasone dipropionate from chitosan-based spray-dried respirable powders." In: *Powder Technology* 187.3 (Nov. 2008), pp. 231–238. ISSN: 0032-5910. DOI: 10.1016/J.POWTEC.2008.02.015.

[55] Mine Ozyazici, Aysu Yurdasiper, and Mesut Arici. "Triamcinolone acetonide dry powder inhalation: A new approach for treathing asthma." In: *Journal of Pharmaceutics & Drug Delivery Research* 5.6 (2016). ISSN: 2325-9604.

[56] Faezeh Khandouzi, Zahra Daman, and Kambiz Gilani. "Optimized particle engineering of fluticasone propionate and salmeterol xinafoate by spray drying technique for dry powder inhalation." In: *Advanced Powder Technology* 28.2 (Feb. 2017), pp. 534–542. ISSN: 0921-8831. DOI: 10.1016/J.APT.2016.10.022.

[57] K. J. Knox et al. "Direct measurements of the axial displacement and evolving size of optically trapped aerosol droplets." In: *Journal of Optics A: Pure and Applied Optics* 9.8 (Aug. 2007), S180–S188. ISSN: 1464-4258. DOI: 10.1088/1464-4258/9/8/S10.

[58] James F Davies, Allen E Haddrell, and Jonathan P Reid. "Time-Resolved Measurements of the Evaporation of Volatile Components from Single Aerosol Droplets." In: *Aerosol Science and Technology* 46.6 (June 2012), pp. 666–677. ISSN: 0278-6826. DOI: 10.1080/02786826.2011.652750.

[59] Alberto Baldelli et al. "Analysis of the Particle Formation Process of Structured Microparticles." In: *Molecular Pharmaceutics* 12.8 (Aug. 2015), pp. 2562–2573. ISSN: 1543-8384. DOI: 10.1021/mp500758s.

[60] Alberto Baldelli et al. "Effect of crystallization kinetics on the properties of spray dried microparticles." In: *Aerosol Science and Technology* 50.7 (July 2016), pp. 693–704. ISSN: 0278-6826. DOI: 10.1080/02786826.2016.1177163.

[61] M. Kulmala, T. Vesala, and P.E. E. Wagner. "An analytical expression for the rate of binary condensational particle growth: Comparison with numerical results." In: *Journal of Aerosol Science* 23.SUPPL. 1 (Jan. 1992), pp. 133–136. ISSN: 00218502. DOI: 10.1016/0021-8502(92)90367-5.

[62] S. Tonini and G.E. Cossali. "An analytical model of liquid drop evaporation in gaseous environment." In: *International Journal of Thermal Sciences* 57 (July 2012), pp. 45–53. ISSN: 1290-0729. DOI: 10.1016/J.IJTHERMALSCI.2012.01.017.

[63] E. Periasamy Ravindran and James Davis. "Multicomponent evaporation of single aerosol droplets." In: *Journal of Colloid and Interface Science* 85.1 (Jan. 1982), pp. 278–288. ISSN: 00219797. DOI: 10.1016/0021-9797(82)90256-9.

[64] Fred R. Newbold and Neal R. Amundson. "A model for evaporation of a multicomponent droplet." In: *AIChE Journal* 19.1 (Jan. 1973), pp. 22–30. ISSN: 0001-1541. DOI: 10.1002/aic.690190105.

[65] B. Abramzon and W.A. Sirignano. "Droplet vaporization model for spray combustion calculations." In: *International Journal of Heat and Mass Transfer* 32.9 (Sept. 1989), pp. 1605–1618. ISSN: 00179310. DOI: 10.1016/0017-9310(89)90043-4.

[66] Rebecca J Hopkins and Jonathan P Reid. "A Comparative Study of the Mass and Heat Transfer Dynamics of Evaporating Ethanol/Water, Methanol/Water, and 1-Propanol/Water Aerosol Droplets." In: *The Journal of Physical Chemistry B* 110.7 (Feb. 2006), pp. 3239–3249. ISSN: 1520-6106. DOI: 10.1021/jp056523g.

[67] John H Seinfeld and Spyros N Pandis. *Atmospheric Chemistry and Physics : From Air Pollution to Climate Change*. New York, UNITED STATES: John Wiley & Sons, Incorporated, 2016. ISBN: 9781119221166.

[68] William A Sirignano. *Fluid dynamics and transport of droplets and sprays*. Cambridge university press, 1999. ISBN: 0521630363.

[69] Solomon Gebreyohannes, Brian J. Neely, and Khaled A.M. Gasem. "One-parameter modified nonrandom two-liquid (NRTL) activity coefficient model." In: *Fluid Phase Equilibria* 379 (Oct. 2014), pp. 196–205. ISSN: 0378-3812. DOI: 10.1016/J.FLUID.2014.07.027.

[70] Ibrahim Sadek Khattab et al. "Density, viscosity, and surface tension of water+ethanol mixtures from 293 to 323K." In: *Korean Journal of Chemical Engineering* 29.6 (June 2012), pp. 812–817. ISSN: 0256-1115. DOI: 10.1007/s11814-011-0239-6.

[71] Nancy Ekdawi-Sever et al. "Diffusion of Sucrose and α,α-Trehalose in Aqueous Solutions." In: *The Journal of Physical Chemistry A* 107.6 (Feb. 2003), pp. 936–943. ISSN: 1089-5639. DOI: 10.1021/jp020187b.

[72] Ross Taylor and Rajamani Krishna. *Multicomponent mass transfer*. Vol. 2. John Wiley & Sons, 1993. ISBN: 0471574171.

[73] Charles R Wilke. "Diffusional properties of multicomponent gases." In: *Chemical Engineering Progress* 46.2 (1950), pp. 95–104. ISSN: 0360-7275.

[74] D F Fairbanks and C R Wilke. "Diffusion Coefficients in Multicomponent Gas Mixtures." In: *Industrial & Engineering Chemistry* 42.3 (Mar. 1950), pp. 471–475. ISSN: 0019-7866. DOI: 10.1021/ie50483a022.

[75] Y P Tang and D M Himmelblau. "Effective binary diffusion coefficients in mixed solvents." In: *AIChE Journal* 11.1 (Jan. 1965), pp. 54–58. ISSN: 0001-1541. DOI: 10.1002/aic.690110114.

[76] R Byron Bird, Warren E. Stewart, and Edwin N. Lightfoot. *Transport Phenomena*. Revised 2nd. New York: John Wiley & Sons, 2006. ISBN: 978-0-470-11539-8.

[77] Joe M. Smith, Hendrick C. Van Ness, and Michael M. Abbott. *Introduction to Chemical Engineering Thermodynamics*. 7th ed. New York: McGraw-Hill, 2005. ISBN: 0-07-310445-0.

[78] L H Horsley. "Table of Azeotropes and Nonazeotropes." In: *Analytical Chemistry* 19.8 (Aug. 1947), pp. 508–600. ISSN: 0003-2700. DOI: 10.1021/ac60008a002.

[79] A. Bader, P. Keller, and C. Hasse. "The influence of non-ideal vapor–liquid equilibrium on the evaporation of ethanol/iso-octane droplets." In: *International Journal of Heat and Mass Transfer* 64 (Sept. 2013), pp. 547–558. ISSN: 00179310. DOI: 10.1016/j.ijheatmasstransfer.2013.04.056.

[80] A Jouyban and W E Acree. "In silico prediction of drug solubility in water-ethanol mixtures using Jouyban- Acree model." In: *J Pharm Pharmaceut Sci (www. cspsCanada.org)* 9.2 (2006), pp. 262–269.

[81] Dexter J. D'Sa, David Lechuga-Ballesteros, and Hak Kim Chan. "Isothermal Microcalorimetry of pressurized systems I: A rapid method to evaluate pressurized metered dose inhaler formulations." In: *Pharmaceutical Research* 31.10 (2014), pp. 2716–2723. ISSN: 1573904X. DOI: 10.1007/s11095-014-1369-4.

[82] L. Tajber et al. "Spray drying of budesonide, formoterol fumarate and their composites—I. Physicochemical characterisation." In: *International Journal of Pharmaceutics* 367.1-2 (Feb. 2009), pp. 79–85. ISSN: 03785173. DOI: 10.1016/j.ijpharm.2008.09.030.

[83] Orla Ní Ógáin et al. "Particle engineering of materials for oral inhalation by dry powder inhalers. I—Particles of sugar excipients (trehalose and raffinose) for protein delivery." In: *International Journal of Pharmaceutics* 405.1-2 (Feb. 2011), pp. 23–35. ISSN: 0378-5173. DOI: 10.1016/J.IJPHARM.2010.11.039.

[84] Jaya Mishra et al. "Influence of Solvent Composition on the Performance of Spray-Dried Co-Amorphous Formulations." In: *Pharmaceutics* 10.2 (2018), p. 47. ISSN: 1999-4923. DOI: 10.3390/pharmaceutics10020047.

[85] Anne Marie Healy et al. "Dry powders for oral inhalation free of lactose carrier particles." In: *Advanced Drug Delivery Reviews* 75 (Aug. 2014), pp. 32–52. ISSN: 0169409X. DOI: 10.1016/j.addr.2014.04.005.

[86] Anna Lechanteur and Brigitte Evrard. "Influence of Composition and Spray-Drying Process Parameters on Carrier-Free DPI Properties and Behaviors in the Lung: A review." In: *Pharmaceutics* 12.1 (Jan. 2020), p. 55. ISSN: 1999-4923. DOI: 10.3390/pharmaceutics12010055.

[87] Alberto Baldelli and Reinhard Vehring. "Analysis of cohesion forces between monodisperse microparticles with rough surfaces." In: *Colloids and Surfaces A: Physicochemical and Engineering Aspects* 506 (Oct. 2016), pp. 179–189. ISSN: 0927-7757. DOI: https://doi.org/10.1016/j.colsurfa.2016.06.009.

[88] Hui Wang, David S. Nobes, and Reinhard Vehring. "Particle Surface Roughness Improves Colloidal Stability of Pressurized Pharmaceutical Suspensions." In: *Pharmaceutical Research* 36.3 (Mar. 2019), p. 43. ISSN: 0724-8741. DOI: 10.1007/s11095-019-2572-0.

[89] Basanth Babu Eedara et al. "The influence of surface active L-leucine and 1,2-dipalmitoyl-sn-glycero-3-phosphatidylcholine (DPPC) in the improvement of aerosolization of pyrazinamide and moxifloxacin co-spray dried powders." In: *International Journal of Pharmaceutics* 542.1-2 (May 2018), pp. 72–81. ISSN: 18733476. DOI: 10.1016/j.ijpharm.2018.03.005.

[90] P.C. Seville et al. "Amino acid-modified spray-dried powders with enhanced aerosolisation properties for pulmonary drug delivery." In: *Powder Technology* 178.1 (Sept. 2007), pp. 40–50. ISSN: 00325910. DOI: 10.1016/j.powtec.2007.03.046.

[91] Jacek Gliński, Guy Chavepeyer, and Jean-Karl Platten. "Surface properties of aqueous solutions of l-leucine." In: *Biophysical Chemistry* 84.2 (Apr. 2000), pp. 99–103. ISSN: 0301-4622. DOI: 10.1016/S0301-4622(99)00150-7.

[92] Pei T. Mah et al. "The use of hydrophobic amino acids in protecting spray dried trehalose formulations against moisture-induced changes." In: *European Journal of Pharmaceutics and Biopharmaceutics* 144 (Nov. 2019), pp. 139–153. ISSN: 09396411. DOI: 10.1016/j.ejpb.2019.09.014.

[93] Marine Nuzzo et al. "Surface Composition and Morphology of Particles Dried Individually and by Spray Drying." In: *Drying Technology* 33.6 (Apr. 2015), pp. 757–767. ISSN: 0737-3937. DOI: 10.1080/07373937.2014.990566.

[94] Feifei Yang et al. "The effects of surface morphology on the aerosol performance of spray-dried particles within HFA 134a based metered dose formulations." In: *Asian Journal of Pharmaceutical Sciences* 10.6 (Dec. 2015), pp. 513–519. ISSN: 18180876. DOI: 10.1016/j.ajps.2015.07.006.

[95] Mani Ordoubadi et al. "Multi-Solvent Microdroplet Evaporation: Modeling and Measurement of Spray-Drying Kinetics with Inhalable Pharmaceutics." In: *Pharmaceutical Research* 36.7 (July 2019), p. 100. ISSN: 0724-8741. DOI: 10.1007/s11095-019-2630-7.

[96] Nicholas B. Carrigy et al. "Amorphous pullulan trehalose microparticle platform for respiratory delivery." In: *International Journal of Pharmaceutics* 563 (May 2019), pp. 156–168. ISSN: 03785173. DOI: 10.1016/j.ijpharm.2019.04.004.

[97] Guangwen He et al. "Determination of Critical Supersaturation from Microdroplet Evaporation Experiments." In: *Crystal Growth & Design* 6.5 (May 2006), pp. 1175–1180. ISSN: 1528-7483. DOI: 10.1021/cg050681f.

[98] Nan Fu, Meng Wai Woo, and Xiao Dong Chen. "Single Droplet Drying Technique to Study Drying Kinetics Measurement and Particle Functionality: A Review." In: *Drying Technology* 30.15 (Dec. 2012), pp. 1771–1785. ISSN: 0737-3937. DOI: 10.1080/07373937.2012.708002.

[99] R. de Souza Lima, M.-I. Ré, and P. Arlabosse. "Drying droplet as a template for solid formation: A review." In: *Powder Technology* 359 (Jan. 2020), pp. 161–171. ISSN: 00325910. DOI: 10.1016/j.powtec.2019.09.052.

[100] Matthias Griesing et al. "Influence of Air Humidity on the Particle Formation of Single Mannitol-Water Droplets during Drying." In: *Chemie Ingenieur Technik* 88.7 (July 2016), pp. 929–936. ISSN: 0009-286X. DOI: 10.1002/cite.201500087.

[101] Rosa Mondragon et al. "Study of the drying behavior of high load multiphase droplets in an acoustic levitator at high temperature conditions." In: *Chemical Engineering Science* 66.12 (June 2011), pp. 2734–2744. ISSN: 00092509. DOI: 10.1016/j.ces.2011.03.033.

[102] L Hennet et al. "Aerodynamic levitation and laser heating: Applications at synchrotron and neutron sources." In: *The European Physical Journal Special Topics* 196.1 (May 2011), pp. 151–165. ISSN: 1951-6355. DOI: 10.1140/epjst/e2011-01425-0.

[103] J K R Weber et al. "Aerodynamic levitator for in situ x-ray structure measurements on high temperature and molten nuclear fuel materials." In: *Review of Scientific Instruments* 87.7 (July 2016), p. 073902. ISSN: 0034-6748. DOI: 10.1063/1.4955210.

[104] G Marty and N Tsapis. "Monitoring the buckling threshold of drying colloidal droplets using water-ethanol mixtures." In: *The European Physical Journal E* 27.2 (Oct. 2008), p. 213. ISSN: 1292-8941. DOI: 10.1140/epje/i2008-10375-6.

[105] F. K. A. Gregson et al. "Studies of competing evaporation rates of multiple volatile components from a single binary-component aerosol droplet." In: *Physical Chemistry Chemical Physics* (2019). ISSN: 1463-9076. DOI: 10.1039/C9CP01158G.

[106] F. K. A. Gregson et al. "Drying and Crystallization of Evaporating Sodium Nitrate Aerosol Droplets." In: *The Journal of Physical Chemistry B* 124.28 (July 2020), pp. 6024–6036. ISSN: 1520-6106. DOI: 10.1021/acs.jpcb.0c04079.

[107] Mani Ordoubadi et al. "Interaction of evaporating multicomponent microdroplets with humid environments." In: *Respiratory Drug Delivery*. 2018.

[108] Sharad Mangal et al. "Relationship between surface concentration of l-leucine and bulk powder properties in spray dried formulations." In: *European Journal of Pharmaceutics and Biopharmaceutics* 94 (Aug. 2015), pp. 160–169. ISSN: 09396411. DOI: 10.1016/j.ejpb.2015.04.035.

[109] Allen Haddrell et al. "Identifying time-dependent changes in the morphology of an individual aerosol particle from its light scattering pattern." In: *Aerosol Science and Technology* (Sept. 2019), pp. 1–18. ISSN: 0278-6826. DOI: 10.1080/02786826.2019.1661351.

[110] MATLAB. *version 9.6.0 (R2019a)*. Natick, Massachusetts: The MathWorks Inc., 2019.

[111] Susan Hoe et al. "Use of a Fundamental Approach to Spray-Drying Formulation Design to Facilitate the Development of Multi-Component Dry Powder Aerosols for Respiratory Drug Delivery." In: *Pharmaceutical Research* 31.2 (2014), pp. 449–465. ISSN: 1573-904X. DOI: 10.1007/s11095-013-1174-5.

[112] Caroline A. Schneider, Wayne S. Rasband, and Kevin W. Eliceiri. "NIH Image to ImageJ: 25 years of image analysis." In: *Nature Methods* 9.7 (July 2012), pp. 671–675. ISSN: 1548-7091. DOI: 10.1038/nmeth.2089.

[113] Hui Wang et al. "Macro-Raman spectroscopy for bulk composition and homogeneity analysis of multi-component pharmaceutical powders." In: *Journal of Pharmaceutical and Biomedical Analysis* 141 (July 2017), pp. 180–191. ISSN: 07317085. DOI: 10.1016/j.jpba.2017.04.003.

[114] Shin Muramoto, Jeremy Brison, and David G. Castner. "Exploring the Surface Sensitivity of TOF-Secondary Ion Mass Spectrometry by Measuring the Implantation and Sampling Depths of Bi n and C 60 Ions in Organic Films." In: *Analytical Chemistry* 84.1 (Jan. 2012), pp. 365–372. ISSN: 0003-2700. DOI: 10.1021/ac202713k.

[115] Mark Nicholas et al. "Quantification of surface composition and surface structure of inhalation powders using TOF-SIMS." In: *International Journal of Pharmaceutics* 587 (Sept. 2020), p. 119666. ISSN: 03785173. DOI: 10.1016/j.ijpharm.2020.119666.

[116] M.V. Galmarini et al. "Comparison of the viscosity of trehalose and sucrose solutions at various temperatures: Effect of guar gum addition." In: *LWT - Food Science and Technology* 44.1 (Jan. 2011), pp. 186–190. ISSN: 0023-6438. DOI: 10.1016/J.LWT.2010.04.021.

[117] J.W. Mullin. "Nucleation." In: *Crystallization*. Fourth Edi. Oxford: Elsevier, 2001, pp. 181–215. ISBN: 978-0-7506-4833-2. DOI: 10.1016/B978-075064833-2/50007-3.

[118] Carl L Yaws. *Yaws' Thermophysical Properties of Chemicals and Hydrocarbons (Electronic Edition)*. 2010.

[119] Samuel H Yalkowsky, Yan He, and Parijat Jain. *Handbook of aqueous solubility data*. Second. Boca Raton, Florida: CRC press, 2019. ISBN: 9780367384173.

[120] Christoph Held, Luca F. Cameretti, and Gabriele Sadowski. "Measuring and Modeling Activity Coefficients in Aqueous Amino-Acid Solutions." In: *Industrial & Engineering Chemistry Research* 50.1 (Jan. 2011), pp. 131–141. ISSN: 0888-5885. DOI: 10.1021/ie100088c.

[121] Nazrul Islam and Matthew J. Cleary. "Developing an efficient and reliable dry powder inhaler for pulmonary drug delivery – A review for multidisciplinary researchers." In: *Medical Engineering & Physics* 34.4 (May 2012), pp. 409–427. ISSN: 13504533. DOI: 10.1016/j.medengphy.2011.12.025.

[122] Mani Ordoubadi et al. "On the particle formation of leucine in spray drying of inhalable microparticles." In: *International Journal of Pharmaceutics* 592 (Jan. 2021), p. 120102. ISSN: 03785173. DOI: 10.1016/j.ijpharm.2020.120102.

[123] Imco Sibum et al. "Dispersibility and Storage Stability Optimization of High Dose Isoniazid Dry Powder Inhalation Formulations with L-Leucine or Trileucine." In: *Pharmaceutics* 12.1 (Dec. 2019), p. 24. ISSN: 1999-4923. DOI: 10.3390/pharmaceutics12010024.

[124] Mellissa Gomez et al. "Development of a formulation platform for a spray-dried, inhalable tuberculosis vaccine candidate." In: *International Journal of Pharmaceutics* 593 (Jan. 2021), p. 120121. ISSN: 03785173. DOI: 10.1016/j.ijpharm.2020.120121.

[125] Nicholas B. Carrigy et al. "Trileucine and Pullulan Improve Anti-Campylobacter Bacteriophage Stability in Engineered Spray-Dried Microparticles." In: *Annals of Biomedical Engineering* (Dec. 2019). ISSN: 0090-6964. DOI: 10.1007/s10439-019-02435-6.

[126] Philipp Seydel, Jan Blömer, and Jürgen Bertling. "Modeling particle formation at spray drying using population balances." In: *Drying Technology* 24.2 (2006), pp. 137–146. ISSN: 07373937. DOI: 10.1080/07373930600558912.

[127] Peter G. Vekilov. "Nucleation." In: *Crystal Growth & Design* 10.12 (Dec. 2010), pp. 5007–5019. ISSN: 1528-7483. DOI: 10.1021/cg1011633.

[128] Reinhard Miller et al. "4 Surfactant Adsorption Layers at Liquid Interfaces." In: *Surfactant Science and Technology*. CRC Press, 2014, pp. 149–169.

[129] J Eastoe and J.S Dalton. "Dynamic surface tension and adsorption mechanisms of surfactants at the air–water interface." In: *Advances in Colloid and Interface Science* 85.2-3 (Mar. 2000), pp. 103–144. ISSN: 00018686. DOI: 10.1016/S0001-8686(99)00017-2.

[130] M. Jayasundera et al. "Surface modification of spray dried food and emulsion powders with surface-active proteins: A review." In: *Journal of Food Engineering* 93.3 (Aug. 2009), pp. 266–277. ISSN: 02608774. DOI: 10.1016/j.jfoodeng.2009.01.036.

[131] K. Landström, J. Alsins, and B. Bergenståhl. "Competitive protein adsorption between bovine serum albumin and β-lactoglobulin during spray-drying." In: *Food Hydrocolloids* 14.1 (Jan. 2000), pp. 75–82. ISSN: 0268-005X. DOI: 10.1016/S0268-005X(99)00047-8.

[132] Yunfei He et al. "Adsorption–desorption kinetics of surfactants at liquid surfaces." In: *Advances in Colloid and Interface Science* 222 (Aug. 2015), pp. 377–384. ISSN: 00018686. DOI: 10.1016/j.cis.2014.09.002.

[133] A. F. H. Ward and L. Tordai. "Time-Dependence of Boundary Tensions of Solutions I. The Role of Diffusion in Time-Effects." In: *The Journal of Chemical Physics* 14.7 (July 1946), pp. 453–461. ISSN: 0021-9606. DOI: 10.1063/1.1724167.

[134] Bryan R. Bzdek et al. "The surface tension of surfactant-containing, finite volume droplets." In: *Proceedings of the National Academy of Sciences* 117.15 (Apr. 2020), pp. 8335–8343. ISSN: 0027-8424. DOI: 10.1073/pnas.1915660117.

[135] J. Malila and N. L. Prisle. "A monolayer partitioning scheme for droplets of surfactant solutions." In: *Journal of Advances in Modeling Earth Systems* 10.12 (Dec. 2018), 2018MS001456. ISSN: 1942-2466. DOI: 10.1029/2018MS001456.

[136] Martin Meere, Giuseppe Pontrelli, and Sean McGinty. "Modelling phase separation in amorphous solid dispersions." In: *Acta Biomaterialia* 94 (Aug. 2019), pp. 410–424. ISSN: 17427061. DOI: 10.1016/j.actbio.2019.06.009. arXiv: 1902.05410.

[137] "Pre-nucleation clusters as solute precursors in crystallisation." In: *Chem. Soc. Rev.* 43.7 (Apr. 2014), pp. 2348–2371. ISSN: 0306-0012. DOI: 10.1039/C3CS60451A.

[138] Paul C. Hiemenz and Timothy P. Lodge. "Thermodynamics of Polymer Solutions." In: *Polymer Chemistry*. 2nd. Boca Raton: CRC Press, 2007. Chap. 7, pp. 247–288.

[139] Thomas Lindvig, Michael L Michelsen, and Georgios M Kontogeorgis. "A Flory–Huggins model based on the Hansen solubility parameters." In: *Fluid Phase Equilibria* 203.1-2 (Dec. 2002), pp. 247–260. ISSN: 03783812. DOI: 10.1016/S0378-3812(02)00184-X.

[140] Charles M. Hansen. *Hansen Solubility Parameters: A User's Handbook, Second Edition*. CRC Press, June 2007. ISBN: 9780429127526. DOI: 10.1201/9781420006834.

[141] D.W. Van Krevelen and K. Te Nijenhuis. "Chapter 7 - Cohesive Properties and Solubility." In: *Properties of Polymers - Their Correlation with Chemical Structure; Their Numerical Estimation and Prediction from Additive Group Contributions*. 4th ed. Amsterdam: Elsevier, 2009, pp. 189–227. ISBN: 9780080548197. DOI: 10.1016/B978-0-08-054819-7.00007-8.

[142] Miriam Arak Freedman. "Phase separation in organic aerosol." In: *Chemical Society Reviews* 46.24 (Dec. 2017), pp. 7694–7705. ISSN: 0306-0012. DOI: 10.1039/C6CS00783J.